Imperial College London

Adaptive Structures for the Control of Cellular Separation

Michael Garland

Department of Aeronautics

Imperial College London

Submitted in partial fulfilment of the requirements for the degree of Doctor of Philosophy in Aeronautics and the Diploma of Imperial College London

August 2016

Declaration

I herewith declare that all work presented within this thesis is my own, or has been referenced accordingly.

Michael G. C. Garland

The copyright of this thesis rests with the author and is made available under a Creative Commons Attribution Non-Commercial No Derivatives licence. Researchers are free to copy, distribute or transmit the thesis on the condition that they attribute it, that they do not use it for commercial purposes and that they do not alter, transform or build upon it. For any reuse or redistribution, researchers must make clear to others the licence terms of this work.

Abstract

This work describes the research undertaken on the development of adaptive structures to reduce turbulent boundary layer separation from a wing. Separation control is a safety critical function that is currently filled by the application of static vortex generators to the wings on most modern aircraft. These devices generate vorticity which produces a downstream mixing effect, energising the boundary layer and postponing separation. The mixing of the boundary layer also increases the drag of the aircraft, reducing efficiency. As static devices, the mixing effect is also permanent, regardless of the current likelihood of separation.

Adaptive structures allow the development of beneficial geometry from the bodys surface without the use of breaks or mechanisms in the structure surface. This allows geometry modification without sources of parasitic drag or turbulent transition. The first subject of this work is the development of an adaptive surface to provide the desired momentum transfer through the boundary layer when required, and which can be retracted when not needed, reducing drag and increasing efficiency.

Adaptive structures inhabit a complex design space due to the coupling between bending and in-plane stretching of the surface. In previous morphing studies, design optimisation has frequently been used to identify the ideal design parameters. Initially, the design methodology is developed on a test case transferring momentum within a zero-pressure gradient boundary layer. The resulting geometry is then tested experimentally and the structural and fluidic response is found to compare well to simulations.

Once the design approach is validated, it must be applied to an efficient location on an aerofoil. The second area of research is therefore the complex, three-dimensional, separation from a 2D aerofoil. This is investigated experimentally with both mean and time-dependent data. The naturally occurring, three-dimensional and spanwise periodic topology of the separated flow,

termed a ‘stall cell’, is investigated to determine a suitable location for the application of targeted control at a critical point. Fourier analysis and Proper Orthogonal Decomposition are applied to the time-dependent data gathered to extract coherent, periodic, fluctuations in the separated flow field. The variation of the relative strengths of these features, distinct in frequency, is isolated to regions within the stall cell.

Knowledge of the flow field gained during this work is applied to stall cell reduction and a single vortex generator is applied to the wing upstream of an identified critical point within the flow field. The separated area is seen to reduce significantly with this actuation. The design methodology developed previously is applied to the initially curved surface of an aerofoil. The final structure is manufactured and tested experimentally and found to be effective in reducing the separation extent. The control is found to be less effective than the static vortex generators. However, unlike the static device, the adaptive version is fully elastic, in both deployment and reaction, and thus shows none of the detrimental effects associated with traditional devices.

Acknowledgements

Firstly, I would like to express my sincere gratitude to my supervisors, Prof. Jonathan Morrison and Dr. Matthew Santer, for the opportunity to conduct this research at Imperial College. Their guidance has helped steer what, at times, has been a bit of a crazy ride. I would also like to thank the Department of Aeronautics which provided the funding for this project, without which none of the last four years would have been possible.

I owe much of my sanity, as well as the contents of this thesis, to my friends and collogues within the department. My fellow residents of E454: James Bird, Richard Bosworth, Robert Siddall, and James Threadgill – thank you for providing the many thought-provoking discussions, assistance, reassurance, and humour that has been characteristic of this journey. Also, of particular note are the staff of the workshop: Roland Hutchins – for his assistance with even the strangest of requests; Mark Grant – for his understanding when $\pm 5\mu$m really wasn't close enough, and Ian James – for his assistance in all things experimental and without whom I would probably still be hunting for equipment.

Finally I would like to thank my wonderful wife, Plum, who has provided tireless and continuous support over the course of this work, during which she has learnt more about fluid mechanics than she ever wished to.

Contents

List of Figures **11**

List of Tables **15**

Nomenclature **17**

1 Introduction **21**

2 Literature Review **25**

2.1 Separating Boundary Layers 26

2.1.1 Critical Point Theory 30

2.1.2 Effect of Separation on Aerofoils 33

2.1.3 Separation from a Three-Dimensional Wing 36

2.1.4 Separation Control 42

2.2 Compliant structures 48

2.2.1 Morphing Aircraft 48

2.2.2 Morphing Skins 58

2.3 Objectives 60

3 Numerical Methods **63**

3.1 Optimisation 64

3.1.1 Optimisation Algorithm 65

3.1.2 Linearisation of Constraints 66

3.2 Finite Element Analysis 67

3.3 Computational Fluid Dynamics 68

3.3.1 Solver Details and Boundary Conditions 70

3.4 Penalty Function 71

4 Experimental Methods **73**
4.1 Wind Tunnel Control . . . 73
4.2 Surface Pressure Measurements . . . 74
4.3 Oil Flow Visualisation . . . 75
4.4 Particle Image Velocimetry . . . 75
4.4.1 Hardware Setup . . . 75
4.4.2 Processing . . . 77
4.5 Adaptive Device Manufacturing . . . 78
4.6 Data Analysis . . . 79
4.6.1 Non-dimensional Parameters . . . 79
4.6.2 Power Spectral Density . . . 80
4.6.3 Proper Orthogonal Decomposition . . . 81

5 Adaptive Boundary Layer Control **83**
5.1 Geometric Objective Function . . . 84
5.1.1 Shell Simulation Setup . . . 86
5.1.2 Geometric Optimisation . . . 87
5.1.3 Influence on a Simulated Boundary Layer . . . 89
5.2 Aerodynamic Objective . . . 91
5.3 Influence of Gaussian Curvature on Morphing Structures . . . 97
5.4 Lattice Structure . . . 98
5.4.1 Unit Cell Topology . . . 101
5.4.2 Beam Element Simulation . . . 101
5.4.3 Lattice Optimisation . . . 103
5.4.4 Experimental Validation . . . 106
5.5 Implementation . . . 108
5.6 Discussion . . . 111
5.7 Summary . . . 113

6 Cellular Separation **115**
6.1 Experimental Setup . . . 115
6.1.1 Dynamic Pressure Fluctuations . . . 116
6.1.2 Wind Tunnel Model . . . 119
6.1.3 Boundary Layer Conditioning . . . 119
6.2 Selection of Experimental Conditions . . . 120
6.2.1 Skin Friction . . . 121

6.2.2 Velocity Field . . . 123
6.3 Mean Velocity Field . . . 123
6.4 Mean Surface Pressure . . . 129
6.5 Frequency Distribution of Surface Pressure Fluctuations . . . 131
6.6 Modal Decomposition of Velocity Fluctuations . . . 133
6.7 Discussion . . . 141
6.7.1 Mean Flow . . . 141
6.7.2 Unsteady Flow . . . 142

7 Point Actuation **147**
7.1 Introduction . . . 147
7.2 Actuator Placement . . . 147
7.3 Adaptive Device Design . . . 150
7.4 Actuation with an Adaptive Actuator . . . 154
7.5 Summary . . . 157

8 Conclusions **159**
8.1 The Design, Optimisation and Manufacture of an Adaptive Boundary-Layer Control Device . . . 159
8.2 Investigation of Cellular Separation from an Aerofoil . . . 161
8.3 Point Control of a Stall Cell . . . 162
8.4 Further Work . . . 163

References **165**

List of Figures

2.1 Boundary layer velocity profiles: (b) Leading edge, (c) and (d) development under zero pressure gradient; (e) and (f) development and separation under adverse pressure gradient with separating streamline (- - -). Reproduced from Schlichting and Gersten (2000) 27

2.2 An aerofoil as a source and sink of vorticity with separation point (•) and separating streamline (- - -), adapted from Lighthill (1963). 29

2.3 Skin friction topologies around a critical point ($\boldsymbol{\tau}_w = 0$) in the $[p, q]$ plane (Délery, 2001). 31

2.4 Skin friction topologies around simple geometries. Nodal points are highlighted in blue. 33

2.5 Streamlines around a 2D NASA GA(W)-1 aerofoil during separation. Separation point marked with (•) 34

2.6 Aerofoil performance for the NASA GA-W(1) profile at $Re = 3.5 \times 10^5$ as calculated using X-Foil (Drela, 1989) 35

2.7 Appearance of stall cells at a range of: (a) aspect ratios (Winkelmann and Barlow, 1980), and (b) incidence angles (Boiko et al., 1996). 37

2.8 Flow models for Stall Cells 39

2.9 Pressure fluctuations on a NACA 0015 aerofoil model at $Re = 3.2 \times 10^5$ and $\alpha = 17°$ presented by Yon and Katz (1998). 40

2.10 Identification of: separation line (SL), trailing edge line (TEL), and stall cell (SC) vortices from RANS data (Manolesos and Voutsinas, 2014) . . 41

2.11 SPIV of a stall cell (Manolesos and Voutsinas, 2014) 41

2.12 Examples of vortex generators: (a) Counter-rotating and co-rotating vanes; (b) Wedge-type; (c) Dimple (Ligrani et al., 2001); and (d) Engine nacelle chine (circled)(Kerker, 1973) 43

2.13 Streamwise velocity distribution recorded downstream of Vane-Type VG inclined at 16° to the flow (Yao et al., 2002) 44
2.14 Reduction of a three dimensional stall cell using a 2D array of vane-type VG (Manolesos and Voutsinas, 2015) 47
2.15 Examples of compliant mechanisms incorporating: (a) concentrated compliance, and (b) distributed compliance 49
2.16 (a) Varieties of morphing technology (Barbarino et al., 2011) and (b) potential applications (Joshi et al., 2004) 50
2.17 Variable span wing section produced by Blondeau and Pines (2004) . . . 52
2.18 Lockheed Z-Wing Demonstrator (Bye and McClure, 2007) 54
2.19 Profile morphing achieved through structural compliance 55
2.20 2D morphing transonic shock control bump by Rhodes (2012) 56
2.21 Three dimensional geometry produced by Rhodes (2012) showing 40% of target deformation – streamwise cross-section shown 57
2.22 Corrugation to produce 'ultra-anisotropic' skins to increase profile morphing capability 59

3.1 Flowchart of structural design optimisation process 64
3.2 Nonlinear constraint example 67
3.3 Typical spectrum of turbulent velocity fluctuations in the frequency domain (data from Pope (2009)) 70

4.1 Frequency response of μDAQ compared to an Endevco high-frequency pressure probe 74
4.2 PIV Timing Trace from a Digital Oscilloscope 77

5.1 Comparison of morphed and target surfaces (Rhodes, 2012) 84
5.2 (a) Target geometry and (b) optimisation domain 85
5.3 Grid convergence results, variation of peak stress with cell count 87
5.4 Geometric convergence and peak von Mises stress 88
5.5 Optimal geometry for minimising RMS positional error using an actuated uniform plate 89
5.6 Plate CFD Mesh 90
5.7 Boundary-layer profiles downstream of deformed geometry 91
5.8 Convergence plots of the objective function for (a) each subiteration call; (b) CFD grid; and (c) optimisation iterations 93

5.9 Deformed geometry resulting from the converged optimisation function using a shell section 95
5.10 Mean boundary layer profiles for the 'clean' condition (×), the optimised deformation (○), and a fixed static vortex generator (▽). 96
5.11 Gaussian curvature distributions on three wing segments: (a) unmodified geometry; (b) the same section following a camber variation (zero Gaussian curvature); and (c) the original section with a local, out-of-plane, geometry change (non-zero Gaussian curvature) 99
5.12 Example of a bending-dominated lattice under in-plane normal loading. 100
5.13 (a) the unit-cell parameters which define the lattice, and (b) 2D lattice simulation with hex-chiral geometry. 102
5.14 Variation of peak stress with beam element count 102
5.15 Plot of optimisation function convergence with Shape factor (○) and corresponding peak von Mises stress (×) 104
5.16 Deformed geometry resulting from the converged optimisation function. The deformation achieved with a simple shell in the previous section is included for comparison. 105
5.17 Scheme for Plate Experiment in 18-inch Tunnel 107
5.18 Mean boundary layer profiles for the 'clean' condition (×), a discrete forwards wedge vortex generator (▽) and with the optimised deformation (○). Experimental and computational results for all cases are shown as solid (—) and dotted (· · ·) lines respectively. 107
5.19 Typical node of the manufactured lattice viewed under an optical microscope 108
5.20 Measurement and comparison of manufactured lattice displacement to finite element predictions. 110

6.1 Experimental setup of the GA(W)-1 model in the Donald Campbell wind tunnel 117
6.2 Freestream Characteristics of 5×4 Wind Tunnel at $U = 24.5$ ms^{-1} . . . 118
6.3 Effect of Ballotini on Lift Coefficient 120
6.4 Surface oil flow visualisation of the wall shear stress distribution for a NASA GA(W)-1 aerofoil at $Re \approx 3.5 \times 10^5$. Critical points are overlayed and distinguished between Saddles – S, and Foci – F. 122

6.5 Mean velocity (a, c, e, g) and turbulence intensity (b, d, f, h) for a series of spanwise planes parallel to the trailing edge of a NASA GA(W)-1 aerofoil at $Re = 3.5 \times 10^5$ and $\alpha = 15°$. 126
6.6 Mean spanwise velocity w (a, c, e, g) and turbulence intensity (b, d, f, h) for a series of streamwise, wall normal, planes NASA GA(W)-1 aerofoil at $Re = 3.5 \times 10^5$ and $\alpha = 15°$ 128
6.7 Mean surface pressure across a stall cell on a GA(W)-1 aerofoil at $\alpha = 15°$ and $Re = 3.5 \times 10^5$. Flow from top to bottom of each figure. 130
6.8 Surface pressure spectra from four positions across a stall cell at $Re = 3.5 \times 10^5$ and $\alpha = 15°$. 131
6.9 Surface pressure spectra from a high frequency transducer located near the cell boundary 132
6.10 POD Modes for streamwise × wall normal plane at $z_s/c = 0$ 136
6.11 POD Modes for streamwise × wall normal plane at $z_s/c = 0.49$ 138
6.12 POD Modes of the wall-parallel plane at $y_{TE} = 20$ mm 140
6.13 Comparison of frequency distribution of pressure fluctuations from within separating regions across a range of flows. 144

7.1 Convection of information along streamlines within a stall cell. The bifurcating saddle point is marked with (•). 148
7.2 Flow field before and after application of a discrete VG to the wing . . . 149
7.3 Polar mesh grid topology. Only one in four grid guidelines shown for clarity. 151
7.4 Convergence of the aerofoil boundary layer shape factor and peak stress with optimisation iterations 152
7.5 Wing section actuator 153
7.6 Flow field before and after actuation of the optimised Adaptive VG . . . 155

List of Tables

5.1 Optimisation design variables $\mathbf{x}$ and their constraints $\mathbf{x_{LB}}$ and $\mathbf{x_{UB}}$ 86
5.2 Optimal design parameters for minimising RMS positional error using an actuated uniform plate 88
5.3 Optimal design parameters for minimising H using an actuated uniform plate 94
5.4 Comparison of boundary layer shape factors 94
5.5 Lattice design parameters and their constraints 103
5.6 Lattice design parameters and their optimal values 104
5.7 Comparison of boundary layer shape factors 108

7.1 Lattice design parameters and their constraints for decreasing the boundary layer shape factor over an aerofoil section 152

Nomenclature

Greek Symbols

α	Incidence Angle
δ	Boundary Layer Thickness
δ^*	Boundary Layer Displacement Thickness
ϵ	Strain
θ	Boundary Layer Momentum Thickness
κ	Gaussian Curvature
ν	Kinematic Viscosity (Chapter 6)
ν	Poisson's Ratio (Chapter 5)
ρ	Density
σ	Stress
τ_w	Surface Shear Stress
Φ	Modes of Proper Orthogonal Decomposition
χ	Euler Characteristic
ω	Vorticity

Roman Symbols

c	Aerofoil Chord Length
E	Young's Modulus of Elasticity
C_D	Drag Coefficient

C_L	Lift Coefficient
C_P	Coefficient of Pressure
f	Frequency
H	Boundary Layer Shape Factor
h	Height
L, l	Length
M	Bending Moment
p	Static Pressure
S	Objective Function
St	Strouhal Number
t	Time
Tu	Turbulence Intensity
u, v, w	Components of Velocity (streamwise, wall-normal, spanwise)
U_e	Velocity at the Boundary Layer Edge
U_∞	Freestream Velocity
x, y, z	Directions (streamwise, wall-normal, spanwise)
x	Design Variables

Abbreviations

AR	Aspect Ratio
FE	Finite Element
LES	Large Eddy Simulation
RANS	Reynolds Averaged Navier-Stokes
SLV	Separation Line Vortex
sPIV	Stereo Particle Image Velocimetry
TELV	Trailing Edge Line Vortex

VG Vortex Generator

Chapter 1

Introduction

The use of approximately rigid structures has dominated the mechanical design of aircraft for many years. This is a robust method, used throughout the design world, in which an ideal aerodynamic form is developed and a series of internal supports maintains the shape, within a tolerance, under load. By ensuring that the geometry remains unchanged throughout the anticipated flight envelope, the performance of the aircraft is more easily predicted.

The aircraft must operate over a wide range of flight conditions. For a commercial passenger aircraft, the majority of the operating life will be spent in the high-speed, low-drag, cruise condition. However, for take-off and landing, a low-speed, high-lift, wing is required. In order for the same, rigid, structure to achieve these two opposing operating requirements, mechanisms are frequently used to deploy additional components from the wing in order to alter both the chord length and camber. Other, more localised modifications, are also made to aircraft wings for both performance and safety applications. One example of this is the application of vortex generators to the surface of the wing to prevent boundary layer separation.

The separation of the fluid boundary layer typically provides the upper limitation on the achievable lift from an aerofoil. This occurs when the near wall flow is decelerated by the adverse pressure gradient which is present on the upper surface of the wing. When the fluid streamlines leave the wing surface, a volume of recirculating fluid is formed which significantly alters the effective inviscid profile. This, coupled with the increased levels of losses associated with the recirculating region, causes a rapid increase in drag. For high Reynolds number flows the separation is also unsteady, adding fluctuating wing loading

to the other detrimental effects. Vortex generators produce a mixing effect in their wake which transfers momentum through the boundary layer and so postpones separation.

When VG are applied to an aerofoil they are typically located in a uniformly-spaced spanwise array upstream of the region of concern. However, studies have shown that, for a wing with large aspect ratio $AR > 3$, the separation pattern consists of an array of spanwise periodic 'stall cells'. Although unstable, these cells have a quasi-steady topology which contains critical points in the flow field. A large degree of uncertainty remains around the formation, distribution and behaviour of stall cells on an aerofoil, however limited work has been conducted developing flow control based on the existence of a 3D rather than 2D separation pattern. As static devices, the mixing effect of a vortex generator is present across the flight envelope and so produces increased drag during cruise. A method to control the deployment of these systems only when and where required would remove this source of inefficiency from the airframe.

Adaptive structures – those which use the structural compliance of the system to achieve motion without mechanisms – have long been proposed as a technique suitable for deployment in aerospace. Prototype aircraft using adaptive structures, frequently termed morphing aircraft, use careful topological positioning of the structure to allow the system to deform under actuation between geometries with different performance characteristics. Achieving this without the mechanisms or additional components required typically reduces the component count, and so weight, of the design. Additionally, the skin can be continuous without the drag promoting steps or gaps necessary to deploy additional parts from the structure.

This thesis investigates the design and positioning of an adaptive separation control device for elastic deployment from a high lift aerofoil. To achieve this, the problem must be considered from both a structural and aerodynamic perspective. Initially, in Chapter 2, a review of the literature on turbulent separation, and its control, from a moderate aspect ratio wing is conducted. Uncertainty in the current understanding of the 3D structure of separation is highlighted and expanded upon. The opportunity to improve the efficiency of separation control based on the local flow topology can then be identified.

The numerical and experimental methods used throughout this work are described in Chapters 3 and 4. A design methodology for an adaptive boundary layer control device, based on a multi-disciplinary design optimisation, is developed and validated on a simple

test case in Chapter 5. Chapter 6 investigates the structure and topology of three-dimensional turbulent separation. Characteristic features are identified in the frequency spectra of the surface pressure. In Chapter 7, a critical point within the flow field is highlighted for the application of control. Actuation is provided at this point by a static vortex generator and the downstream effect from this device is shown to have a large effect on the spanwise form of the stall cell. The static device is replaced by an adaptive version which is also shown to be effective in the control of spanwise separation extent. Finally, in Chapter 8, a summary of the conclusions drawn in the previous chapters is provided and suggestions are made for ongoing research.

Chapter 2

Literature Review

Aircraft wing design is driven by a large number of factors, the foremost of which is the aerodynamic efficiency of the design under cruise conditions where the aircraft may be operating at a relatively low incidence angle $\alpha \approx 1 - 5^{\circ}$ with a corresponding lift coefficient $C_L \approx 0.4 - 0.6$ (Filippone, 2000). These are not, however, the conditions where the wing is operating at its peak lift coefficient. This is instead associated with so-called high-lift configurations, such as those used for take-off and landing. At these conditions, the aircraft is operating at reduced speed yet must maintain the lift required to keep the aircraft in flight. It is achieved by increasing the incidence of the aircraft, and therefore that of the wing, relative to the free-stream flow. The resulting increase in lift coefficient C_L is accompanied by an increase in drag coefficient C_D on the wing. The maximum aerodynamic efficiency C_L/C_D achievable is limited by the eventual increase in drag caused by the departure of fluid streamlines from the surface of the aerofoil as the boundary layer separates and the aircraft begins to stall.

Due to the significant limitations posed by separation on peak aircraft performance, a large body of research has been conducted either to alter the effective geometry of the wing allowing a greater incidence angle; or to delay flow separation by applying control devices which re-energise the boundary layer. Each of these methods has an impact on the aircraft performance during all phases of the flight envelope, either through a significant weight increase or by inducing additional parasitic drag.

One technique to reduce the impact such mechanisms have on a system, which has grown in support in recent years, is that of using adaptive structures. These techniques are designed to use the structural compliance, which exists to a greater or lesser degree

in any engineering system, to produce a useful geometry change when exposed to an actuation load. The conceptual advantage of such a system is that, by removing the additional components required to produce a mechanical assembly, weight can be reduced. In addition, by removing gaps in the aircraft surface, laminar flow may be maintained and so parasitic drag can be reduced (Duncan et al., 2013). The potential advantages of these designs have prompted significant interest from a variety of sources and they may provide a key tool for future aircraft design.

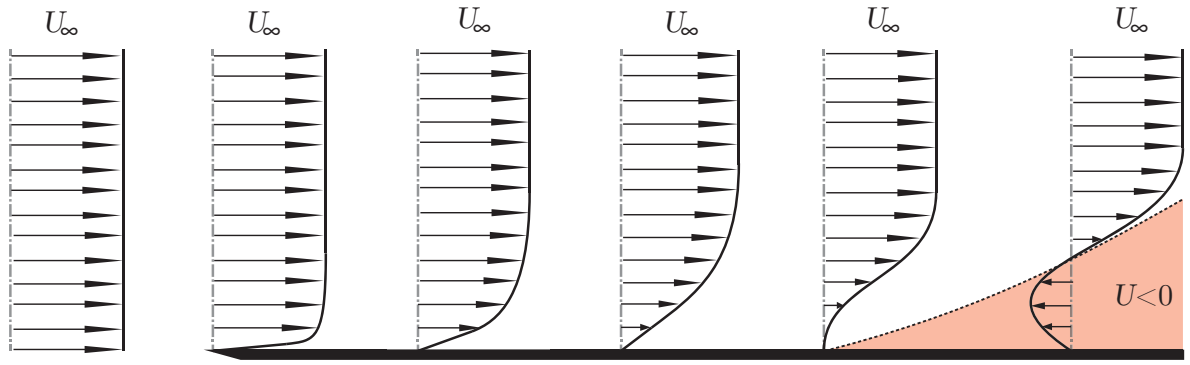
This review will begin with an overview of the mechanism behind boundary layer separation and existing methods of its prevention in Sec. 2.1. A discrepancy between assumptions made during the specification of these methods and the existing literature on the topology of separation in three dimensions will be highlighted and a potential source for improvement is proposed. A summary of compliant structures follows in Sec. 2.2, with an emphasis on the current state-of-the-art of morphing aerodynamic components. The key structural limitations in the development of this field are identified and investigated before the aims of this thesis are presented in Sec. 2.3.

2.1 Separating Boundary Layers

In order to understand the effects that a potential flow control device will have on a separating flow, it is first necessary to discuss the mechanism behind separation, the interaction between pressure gradient and viscosity. In inviscid flows the radial acceleration around a body, or streamline curvature, results in a streamwise variation in pressure. When considering viscous flows at high Reynolds number, and with a zero or favourable pressure gradient, the bulk motion is similar to that of the inviscid case while the effect of viscosity is limited to a thin layer immediately adjacent to the fluid boundary (Prandtl, 1927).

Within the boundary layer, viscosity causes a continuous transition of the fluid velocity between the inviscid flow and, immediately adjacent to the wall, that of the fluid boundary due to the *no-slip* condition (Figs 2.1(b) – (e)). The velocity gradient caused by this deficit modifies the effective 'inviscid' boundary and so alters the pressure gradient over the surface. The magnitude of this geometric modification is termed the *displacement thickness* δ^* and is given by

$$\delta^* = \int_0^\delta \left(1 - \frac{u(y)}{U_e}\right) dy \tag{2.1}$$



(a) (b) $\frac{\partial p}{\partial x} > 0$ (c) $\frac{\partial p}{\partial x} = 0$ (d) $\frac{\partial p}{\partial x} = 0$ (e) $\frac{\partial p}{\partial x} > 0$ (f) $\frac{\partial p}{\partial x} > 0$

Figure 2.1: Boundary layer velocity profiles: (b) Leading edge, (c) and (d) development under zero pressure gradient; (e) and (f) development and separation under adverse pressure gradient with separating streamline (- - -). Reproduced from Schlichting and Gersten (2000)

in which δ is the boundary layer thickness, u is the streamwise fluid velocity, y is the wall normal distance from the surface, and U_e is the velocity at the edge of the boundary layer.

In the presence of a positive (*adverse*) pressure gradient $\left(\frac{dp}{dx} > 0\right)$ the effective modification of the boundary increases and this may drastically alter the flow field around the body. The effect of pressure gradient on velocity in an inviscid, incompressible, flow can be seen from Bernoulli's equation along a streamline s

$$\frac{|\mathbf{u}(\mathbf{s})|^2}{2} + \frac{p(s)}{\rho} = \text{constant} \tag{2.2}$$

where p is the pressure and ρ is the fluid density. Differentiating Eq. 2.2 with respect to s gives

$$\frac{\partial |\mathbf{u}(s)|}{\partial s} + \frac{1}{\rho |\mathbf{u}(s)|} \frac{\partial p(s)}{\partial s} = 0 \tag{2.3}$$

It can be seen from Eq. 2.3 that an adverse pressure gradient $\left(\frac{\partial p}{\partial s} > 0\right)$ acts to retard the flow and that the rate of deceleration is inversely proportional to the velocity magnitude of the fluid. The adverse pressure gradient therefore has the greatest effect on the near-wall flow where velocity magnitude is small. This reduces the near-wall momentum, which increases the velocity deficit and hence thickens the boundary layer. In order to

quantify the impact of the velocity deficit on the fluid momentum, an alternative measure of boundary layer thickness is used. The momentum thickness θ is defined as

$$\theta = \int_0^\delta \frac{u(y)}{U_e}\left(1 - \frac{u(y)}{U_e}\right) dy \tag{2.4}$$

and gives the distance the boundary of an invisicd fluid would need to move in order to give the same total momentum as is present with the boundary layer. The non-dimensional ratio between the two measures of boundary layer thickness, δ^* and θ is termed the shape factor H, given by

$$H = \frac{\delta^*}{\theta} \tag{2.5}$$

and which describes the distribution of momentum through the boundary layer. A low shape factor indicates a large near-wall velocity gradient and is typical of a turbulent boundary layer. A large shape factor indicates a low near-wall gradient with little momentum near to the boundary. For a laminar boundary layer described by the analytical Hartree profile, with $\beta = -0.199$, a shape factor $H = 4.029$ corresponds to the velocity profile at separation (Schlichting and Gersten, 2000).

If an adverse pressure gradient is of sufficient magnitude, or acts over a large enough length, the retardation of the streamwise velocity near the wall will be sufficient to cause a stagnation, and then reversal, of a region of fluid within the boundary layer. When this happens the fluid streamlines, otherwise following the profile of the body, depart the surface and the boundary layer *separates* as shown in Figs. 2.1(e) and (f).

While the inviscid Eq. 2.3 demonstrates the influence of a pressure gradient on varying velocities, the velocity gradient within the boundary layer is present due to the fluid viscosity acting on the velocity difference between the freestream flow and the no-slip condition on the surface. Viscosity cannot therefore be neglected and so must also be considered. In his comprehensive review of boundary layer theory Lighthill (1963) proposes that a surface in a viscous flow behaves as a distributed source, or sink, of vorticity to the fluid (Fig. 2.2). The vorticity generated is then distributed away from the wall through viscous diffusion and downstream through convection with the fluid. It is therefore apparent that the velocity profile of the boundary layer is dependent on both the fluid properties and the vorticity generation at the wall.

The strength of the vorticity flux to the fluid can be determined through application of the continuity equation

$$\nabla \mathbf{u} = \mathbf{0} \tag{2.6}$$

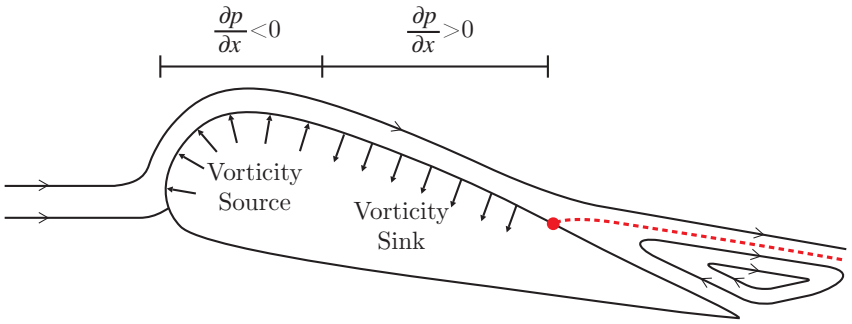


Figure 2.2: An aerofoil as a source and sink of vorticity with separation point (•) and separating streamline (- - -), adapted from Lighthill (1963).

and the incompressible Navier-Stokes equation

$$\frac{\partial \mathbf{u}}{\partial t} + \mathbf{u} \cdot \nabla \mathbf{u} = \phi - \frac{1}{\rho} \nabla p + \nu \nabla^2 \mathbf{u} \tag{2.7}$$

in which t is time, ϕ is the sum of body forces, and ν is the fluid kinematic viscosity. Considering the components of fluid velocity, u, v,and w in the streamwise x, wall normal y, and spanwise z directions respectively, at the wall $y = 0$ and applying the relevant boundary conditions, $(u, v, w)|_{y=0}$, $\left.\frac{\partial (u, v, w)}{\partial (x, z)}\right|_{y=0}$, $\frac{\partial \mathbf{u}}{\partial t}$, and $\phi = 0$ then Eq. 2.7 becomes

$$\nu \left(\frac{\partial^2 u}{\partial y^2} \hat{\mathbf{i}} + \frac{\partial^2 w}{\partial y^2} \hat{\mathbf{k}} \right) = \frac{1}{\rho} \left(\frac{\partial p}{\partial x} \hat{\mathbf{i}} + \frac{\partial p}{\partial z} \hat{\mathbf{k}} \right) \tag{2.8}$$

Considering the wall as a source of vorticity, the transmission of vorticity from the wall to the fluid can be expressed as

$$-\frac{\partial \omega}{\partial y} = -\frac{\partial}{\partial y} \left[\left(\frac{\partial w}{\partial y} - \frac{\partial v}{\partial z} \right), \left(\frac{\partial u}{\partial z} - \frac{\partial w}{\partial x} \right), \left(\frac{\partial v}{\partial x} - \frac{\partial u}{\partial y} \right) \right] \tag{2.9}$$

and when evaluated at the wall this simplifies to

$$-\left.\frac{\partial \omega}{\partial y}\right|_{y=0} = \left[-\left(\frac{\partial^2 w}{\partial y^2} \right), 0, \left(\frac{\partial^2 u}{\partial y^2} \right) \right] \tag{2.10}$$

The x and z components of Eq. 2.8 can therefore be re-written respectively as

$$\nu \frac{\partial \omega_z}{\partial y} = \frac{1}{\rho} \left(\frac{\partial p}{\partial x} \right) \tag{2.11a}$$

$$-\nu \frac{\partial \omega_x}{\partial y} = \frac{1}{\rho} \left(\frac{\partial p}{\partial z} \right). \tag{2.11b}$$

It can be seen from Eqns. 2.11 that the transmission of vorticity to the fluid is perpendicular to both the fluid boundary and the pressure gradient. The diffusion of vorticity within the fluid was formalised by Morton (1984) as a linear transfer of momentum over a velocity gradient with a coefficient of diffusion equal to the fluid viscosity.

In the case where the vorticity flux out of the fluid due to pressure gradient is greater than the diffusion towards the wall, it is possible for the vorticity at the wall, and so skin friction τ_w to vanish:

$$\omega_x|_{y=0} = \left.\frac{\partial u}{\partial y}\right|_{y=0} = \frac{\tau_{w_x}}{\mu} = 0 \tag{2.12a}$$

$$\omega_z|_{y=0} = \left.\frac{\partial w}{\partial y}\right|_{y=0} = \frac{\tau_{w_z}}{\mu} = 0 \tag{2.12b}$$

The locations of these *critical points*, where $\boldsymbol{\tau}_w \equiv 0$, and the topology of the skin friction lines around them can provide a detailed understanding of the near-wall flow.

2.1.1 Critical Point Theory

A critical point can be classified based on the trajectories of skin friction lines in its vicinity (Lighthill, 1963; Tobak and Peake, 1982). These trajectories can be described using the Jacobian of the skin friction vector evaluated at the critical point, which is given by

$$J = \begin{bmatrix} \dfrac{\partial \tau_{w_x}}{\partial x} & \dfrac{\partial \tau_{w_z}}{\partial x} \\ \dfrac{\partial \tau_{w_x}}{\partial z} & \dfrac{\partial \tau_{w_z}}{\partial z} \end{bmatrix}. \tag{2.13}$$

The sign and complex character of the eigenvalues $\lambda_{1,2}$ of J, which are given by

$$\lambda_{1,2} = \frac{-p \pm \sqrt{p^2 - 4q}}{2}, \tag{2.14}$$

where $p = -\left(\mathrm{tr}(J)\right)$ and $q = \det(J)$, determines the behaviour of the critical point and its influence on the surrounding skin friction pattern.

The sign of q determines the classification of the critical point. This can either be a saddle point ($q < 0$), where only two skin friction lines pass through the critical point and the remainder follow a hyperbolic path past the point, or $q > 0$, where all skin friction lines have a common target or source. The parabola $q = p^2/4$ further subdivides this second category into nodes, which approach the critical point on a common tangent, and foci

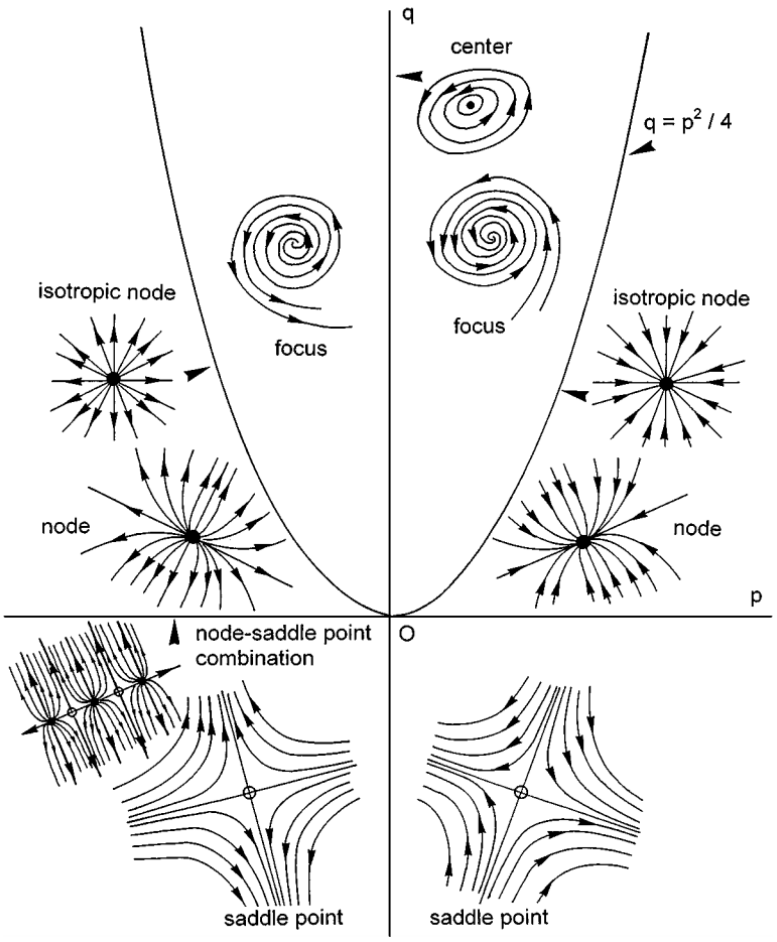


Figure 2.3: Skin friction topologies around a critical point ($\boldsymbol{\tau}_w = 0$) in the $[p, q]$ plane (Délery, 2001).

which spiral around the point. All of these varieties may be either a point of separation ($p > 0$) or attachment ($p < 0$) whereby the topology of the flow adjacent to the critical point remains the same but the direction reverses. The distribution of these points in $[p, q]$ space is shown in Fig. 2.3.

Legendre (1956) describes how the skin friction lines (or wall-bounded streamlines) on a body are part of a continuous vector field. It therefore follows that the trajectory through any non-singular point on the surface is unique and thus that these lines only converge at a finite number of singular points. Based on the categorisation and distribution of critical points, the qualitative topology of skin friction lines on the surface of a body can be determined (Lighthill, 1963). On a three dimensional body, lines of attachment or separation exist but where $\tau_w \neq 0$. These link nodes and saddle points and are termed *dividing streamlines* as they separate flows with opposite direction.

A number of topological rules have been presented regarding the quantity of nodes (Σ_N) and saddles (Σ_S) which appear on an arbitrary surface. The most significant of these is Poincaré-Hopf theorem which states that, for a conservative vector field

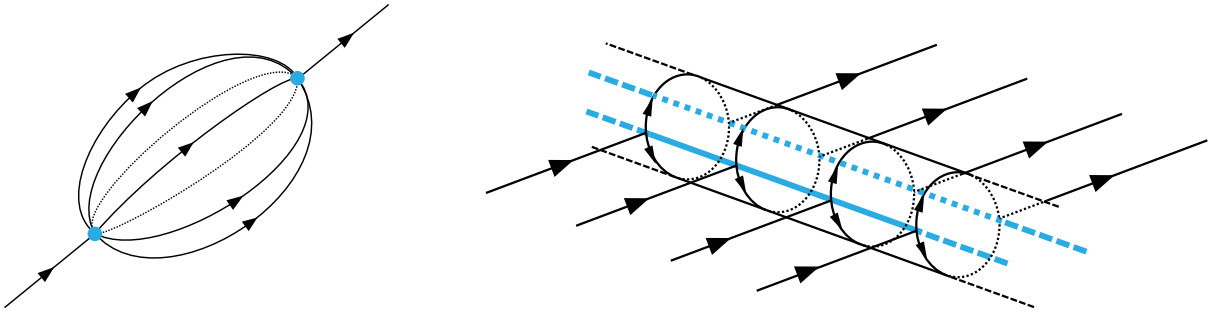
$$\Sigma_N - \Sigma_S = \chi \tag{2.15}$$

where χ is the Euler characteristic of the surface given by

$$\chi = \Sigma_{\mathrm{F}} + \Sigma_{\mathrm{V}} - \Sigma_{\mathrm{E}} \tag{2.16}$$

and Σ_{F}, Σ_{V}, and Σ_{E} are the sum of faces, vertices and edges of a shape respectively.

For the trivial case of an isolated simple three-dimensional body such as that in Fig. 2.4(a), with $\chi = 2$, it can be seen that, without separation, there would exist one node of attachment and one node of separation at the upstream and downstream stagnation points and with no saddle points. For the case of bodies which are not isolated, such as those with an intersection with a planar end-plate or wall, these same features may appear at the intersection and form half nodes and half saddles (N' and S'). One exception of interest to this work concerns the rare cases of axisymmetric or prismatic bodies with leading or trailing edges perpendicular to both the free stream flow and the skin friction lines. In these cases the node of attachment or separation becomes a critical line of attachment or separation, as shown in Fig. 2.4(b), where $\tau_w \equiv 0$ at all locations on the line (Lighthill, 1963). For the topological rules above, this line is a single node. If the body were inclined away from the perpendicular the critical line would coalesce to a point



(a) 3D bullet

(b) 2D cylinder of infinite length with axis perpundicular to the flow.

Figure 2.4: Skin friction topologies around simple geometries. Nodal points are highlighted in blue.

with $\tau_w \equiv 0$ with the remainder of the line acting as a line of attachment or separation where $\tau_w \neq 0$.

In their paper regarding the reconstruction of skin friction line topology from a critical point distribution, Liu and Woodiga (2010) argue that, since the residual index of critical points on a surface is equal to the Euler characteristic, the definition of the domain is very significant. As described above, an isolated 3D body can be topologically equated to a sphere with $\chi = 2$; however few experimental models within a wind tunnel are truly isolated. The model will usually be supported from the tunnel walls or instrumentation via struts, linking the surfaces, and the tunnel itself may be toroidal ($\chi = 0$) or open-loop (χ is an unknown). For this work however, where the focus is on the variation of the topology of skin friction lines on a surface undergoing no severe topological change (such as a small alteration of geometry or variation in inclination to the flow) it follows that χ will remain constant. From Eq. 2.15 any additional critical points that are produced as a result of these changes must therefore be equally divided between nodes and saddles.

2.1.2 Effect of Separation on Aerofoils

Aerofoils at low incidence, and other 'streamlined' bodies, operate at low levels of drag as the streamlines over the two sides of the profile converge at the trailing edge. This occurs as, after a change in velocity or incidence, the viscous forces in the system act to oppose the sharp velocity gradients which would otherwise be present in the vicinity of the trailing edge. The radial acceleration of the fluid due to the additional circulation over the surface produces a streamwise pressure gradient. On the suction surface this

is typically favourable near to the leading edge and adverse over the remainder of the aerofoil surface.

As the incidence increases, the circulation strength also increases, resulting in stronger pressure gradients over the aerofoil. The stronger adverse pressure gradient thickens the boundary layer as described previously, resulting in a greater wake velocity defect, and thus increasing drag. As the incidence is increased further, a specific condition is reached where the strength of the adverse pressure gradient is sufficient to cause fluid within the boundary layer to reverse and the flow to separate. For two-dimensional thick aerofoils operating at moderate and high Reynolds numbers, the stereotypical transition from fully-attached flow to global separation is that of a spanwise line of separation starting at the trailing edge and moving forward with increasing incidence until the separated region consists of the total chord as shown in Fig. 2.5 (McCullough and Gault, 1951).

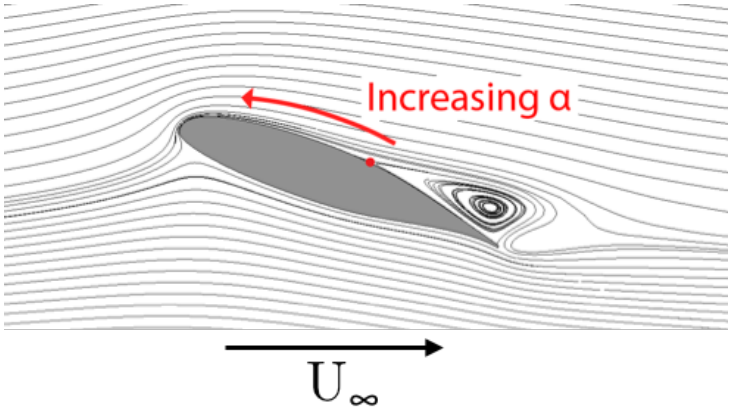
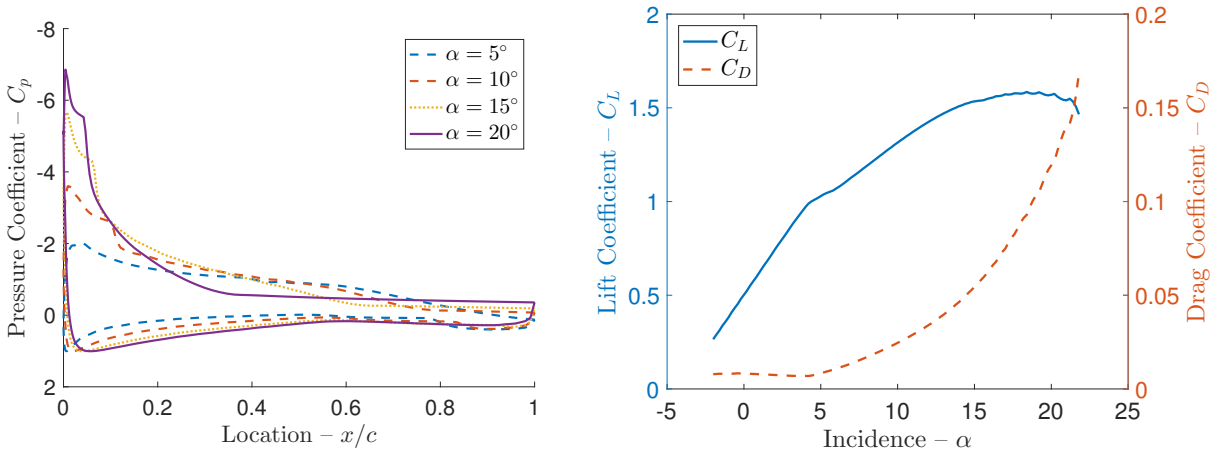


Figure 2.5: Streamlines around a 2D NASA GA(W)-1 aerofoil during separation. Separation point marked with (•)

The recirculating region found downstream of the separation line stretches into the wake and is bounded by upper and lower shear layers. The additional vortical activity maintains coherence into the far wake leading to much larger region of flow generating viscous losses. It is therefore evident that the velocity deficit in the wake is many times thicker than is found in the wake of an attached flow indicating a substantial increase in drag.

When the flow separates and the streamlines no longer follow the aerofoil profile for the entire chord, the circulation added to the inviscid flow decreases throughout the separated region. The radial acceleration of the inviscid flow in that region decreases and the surface pressure increases towards ambient. In Fig. 2.6(a) this effect can be seen at $\alpha = 15°$ at



(a) C_P distribution

(b) C_L and C_D

Figure 2.6: Aerofoil performance for the NASA GA-W(1) profile at $Re = 3.5 \times 10^5$ as calculated using X-Foil (Drela, 1989)

$x/c > 0.6$. The overall effect of separation on resultant forces can be seen in the lift and drag profiles for this wing shown in Fig. 2.6(b).

Once the flow begins to separate from an aerofoil, the vorticity produced in the shear layer rolls-up into discrete spanwise vortex cores which can be unstable. As the vortices gain strength, they are shed downstream and either form a von Kármán vortex street, similar to that produced by a cylinder, or are simply convected with the free stream (Mulleners et al., 2008). For a bluff body, of diameter D, the characteristic frequency f of a von Kármán street corresponds to a Strouhal number $St \approx 0.2$ (Roshko, 1954) where

$$St = \frac{fD}{U_\infty} \tag{2.17}$$

For high angles of attack, aerofoils have been demonstrated to behave in a similar manner to bluff bodies, with $St \approx 0.2$, when the projected height of the aerofoil is used as the characteristic diameter $D = c\sin(\alpha)$ (Huang and Lin, 1995). The shedding of vorticity from the near wake produces a variation in pressure distribution on the aerofoil which leads to a significant fluctuation in the loading of the aerofoil structure (Flynn et al., 2001).

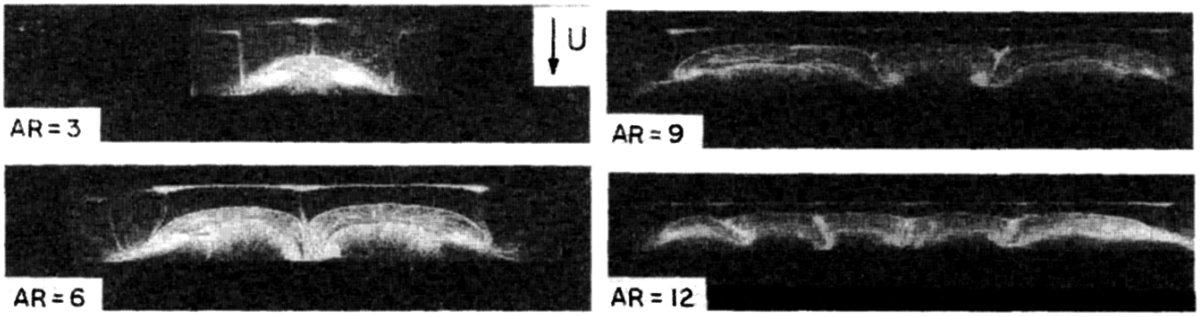
2.1.3 Separation from a Three-Dimensional Wing

Given the previously-described similarity between the behaviour of the flow behind a bluff-body and a two-dimensional aerofoil, it is logical to expect similar behaviour, away from local wing-tip effects, when moving to a three-dimensional body with constant section but with finite span.

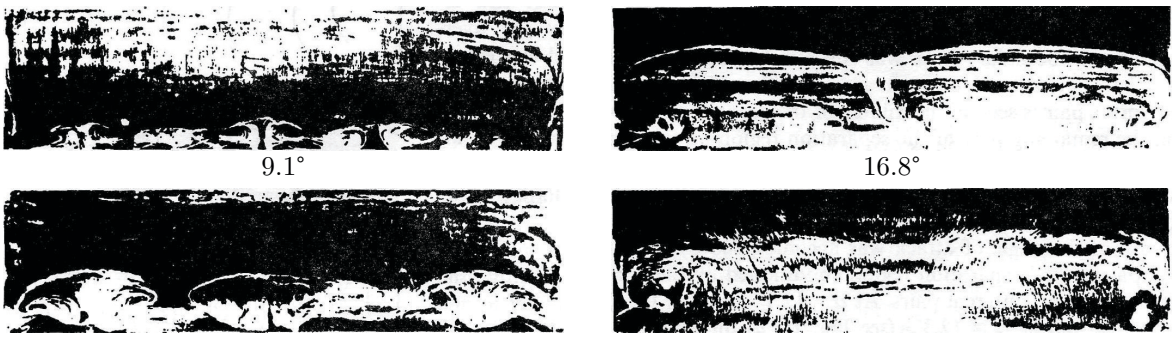
The first report of flow patterns other than those presented above was by Jones (1934) who reported significant low frequency ($St \ll 0.2$) fluctuations in loading from a partially stalled aerofoil. The phenomenon was then reported in passing in subsequent work, however little investigation was conducted until Zaman et al. (1989) presented his review. In this work Zaman et al. (1989) investigated a three-dimensional separated flow field which was recorded in a series of smoke patterns. In these he observed a low frequency 'flapping' of the separated region as well as the anticipated periodic shedding of vorticity into the wake. While trying to isolate the cause of the low frequency phenomenon he discounted many of the presumed sources of this oscillation: blower instability, structural resonance, or a standing acoustic wave. This work also identified that the disturbance was not apparent in flows exhibiting leading edge separation and only present for a small range of α in flows which separated from the trailing edge however a cause for the disturbance was not identified.

During the investigation into the flow of a pitching aerofoil around stall conditions Moss and Murdin (1971) observed that, even in a stable airflow, it was not possible to obtain a steady 2D separation pattern. Further investigation identified local regions of detached flow, the bounds of which were observed to be formed of counter-rotating vortices, which induced upwash within the separated region and downwash on the exterior, thus forming a self stabilising stall cell. It was also discovered during these tests that the development of a stall cell on an aerofoil could be postponed through the addition of vane-type vortex generators upstream of the separated region.

Following this study, Gregory et al. (1971) investigated the flow over a stable aerofoil and reported that, with changing α or Aspect Ratio (AR), the three-dimensional separation pattern varied and was independent of corner effects from the model endplates. This report is also the first to note the existence, under some conditions, of multiple cells on the model surface. Winkelmann and Barlow (1980) extended the data to cover a much larger range of aspect ratios and found that the size of stall cell was independent of aspect ratio. Instead it was observed that with increasing AR the number of stall cells present



(a)



(b)

Figure 2.7: Appearance of stall cells at a range of: (a) aspect ratios (Winkelmann and Barlow, 1980), and (b) incidence angles (Boiko et al., 1996).

under the same flow increased in integer increments. For example, in Fig. 2.7(a) the number of stall cells evident from oil flow visualisation can be seen to increase from one at $AR = 3$ to five visible cells at $AR = 12$.

Additionally it was noted that as incidence was increased the cells merge until, at a sufficient angle, only one cell remains which spans the entire wing planform. The dependence of cell size and distribution on incidence angle was demonstrated experimentally (Fig. 2.7(b)) in a review by Boiko et al. (1996). Both authors mention a state which exists within the incidence range between two stable cell patterns where the cells 'jostle' each other and the global topology switches between integer states. The cause of this behaviour is unknown. However it is clear that it would form the source of further unsteadiness within the flow field and thus wing loading.

Winkelmann and Barlow (1980) also presented a preliminary model of the flow (Fig. 2.8(a)) within a stall cell based on the work above and independent experiments. In this model,

the characteristic 'mushroom' topology is produced by a vortex core which links the two counter-rotating nodes on the aerofoil surface. A separate trailing edge vortex is included below the main loop vortex and the existence of a rear stagnation is predicted although no experimental data were provided on its existence.

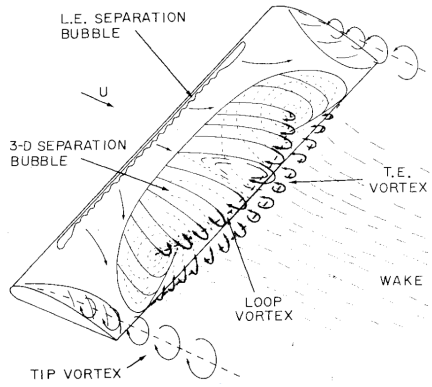
The mechanism for the development of stall cells from a separating wake is still unproven. However Weihs and Katz (1983) proposed that, when the flow over an aerofoil separates, a pair of counter-rotating spanwise vortex cores are produced. Due to fluctuations in the mean flow a symmetric Crow-type instability (Crow, 1970) forms between the two cores which then interact to form vortex rings as shown in Fig. 2.8(b). Crow (1970)'s stability analysis predicted a dominant wavelength of $8.6b$, where b is the spacing between the vortex pairs. Weihs and Katz (1983) use this value, coupled with the mean chord ratio of separated flow K, to estimate the number of stall cells n on an aerofoil to be

$$n = \frac{AR}{17.2K\tan(\alpha)}. \tag{2.18}$$

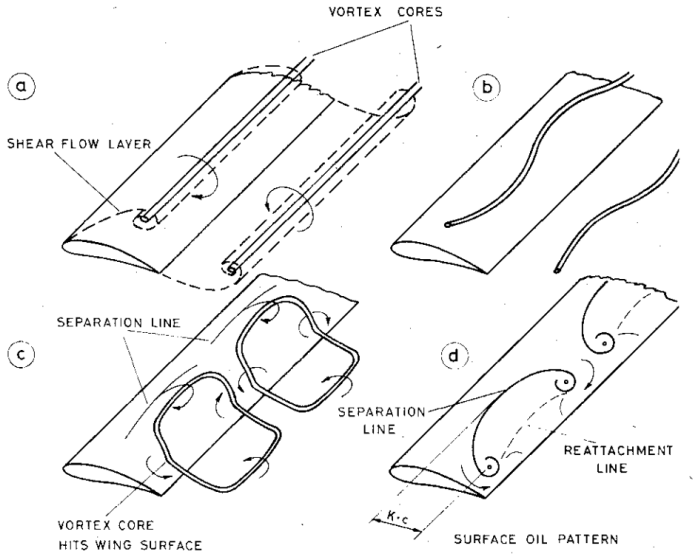
This was shown to be in good agreement with the experimental results of Winkelmann and Barlow (1980), however it requires a level of prior knowledge of the flow. Due to the formulation of this estimate, from an instability analysis on an infinite pair of vortices, no account is made for the limitation of an integer cell count which is observed on finite wings.

The effect of downwash between stall cells predicted by Moss and Murdin (1971) was observed during experiments by Yon and Katz (1998). In this work, surface pressure from the attached flow between stall cells was recorded and compared to the potential flow solution of the same aerofoil at lower angles of attack. In this experiment, at $Re = 6.2 \times 10^5$ and $\alpha = 17°$, the recorded pressure within the stall cell demonstrated the flat distribution typical of fully separated flow while the pressure distribution between cells compared well with the pressures from a potential flow solution at $\alpha = 10°$. The observed downwash is proposed as the stabilising mechanism for the size and periodic distribution along a wing.

Based on the pressure data obtained in this experiment, Yon and Katz (1998) conclude that the flow pattern within a stall cell did not match that of the Winkelmann and Barlow model. Instead a model is proposed where the vortices, formed by the foci bounding each stall cell, trail downstream. This paper is also the first time a potential link is made between the low frequency ($St \ll 0.2$) loading at a finite range of incidence around stall, summarised by Zaman et al. (1989), and cellular separation which occurs in a similar small range.



(a) Stall-cell flow model presented by Winkelmann and Barlow (1980)



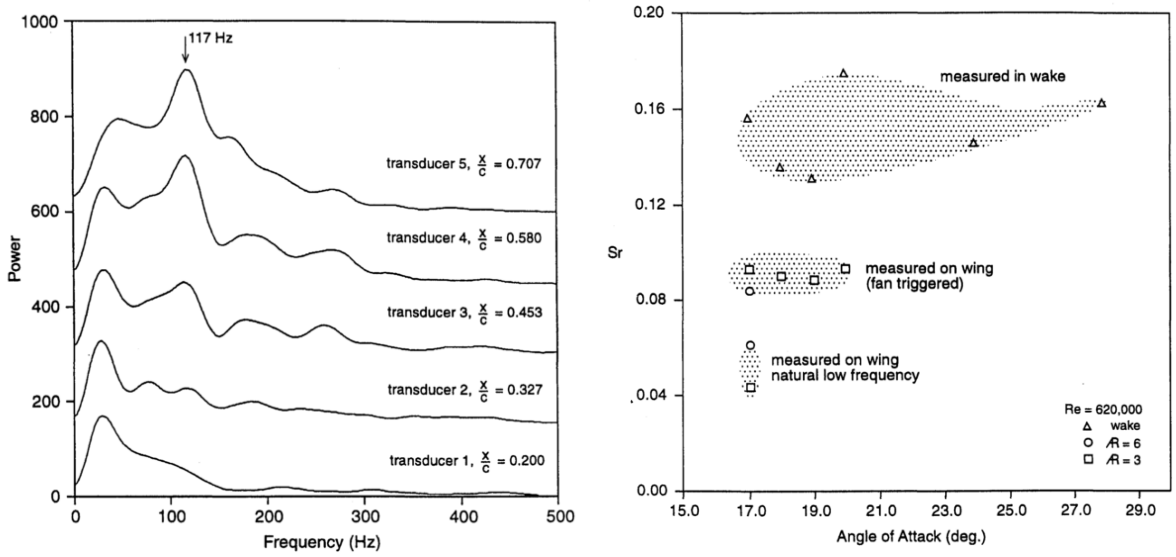
(b) Stall-cell development model presented by Weihs and Katz (1983)

Figure 2.8: Flow models for Stall Cells

The Power Spectral Density (PSD) spectra, shown in Fig. 2.9, of the pressure measurements made by Yon and Katz (1998) demonstrate a peak near $St \approx 0.16$ which is attributed to the typical von Kármán shedding. A second peak is observed at $St \approx 0.05$, slightly higher than that measured by Zaman et al. (1989), in the 'shallow stall' regime where stall cells are observed and is described as a 'natural low frequency'. The same peak is not present in 'deep stall' when no stall cells were visible.

During their investigations, significant time periods (> 0.3 s) were noted where neither of the peaks at $St \approx 0.16$ or 0.05 are observed in the surface pressure data. The authors therefore conclude that, while the low frequency fluctuations are present in the same range as stall cells, the two phenomena are independent. The low frequency fluctuations are instead attributed to a flapping of the separated region in the wake. This conclusion is supported by pressure measurements in the far wake where, in both stall regimes, only fluctuations related to the von Kármán shedding are observed.

Broeren and Bragg (2001) add to this work with a review of the stalling characteristics of a range of aerofoils. Although no PSD estimates are provided, the authors identify a low frequency disturbance associated with aerofoils which exhibit a 2D laminar separation bubble which is not present on models which produce stall cells. While this work does



(a) PSD taken at five chordwise positions. Successive spectra are vertically offset by 150 units for clarity.

(b)

Figure 2.9: Pressure fluctuations on a NACA 0015 aerofoil model at $Re = 3.2 \times 10^5$ and $\alpha = 17°$ presented by Yon and Katz (1998).

not directly contribute to the understanding of stall cells, it does highlight the uncertainty surrounding this phenomenon.

Recently, Manolesos and Voutsinas (2014) conducted an investigation into the structure of stall cells using a combination of RANS simulations (Fig. 2.10) and stereo PIV (Fig. 2.11). To facilitate the experimental study of the separated flow topology, Manolesos and Voutsinas applied a local perturbation at the spanwise centreline downstream of the leading edge which forced the separation pattern to that of a single stall cell. A good correlation between these two sets of results is reported by the authors.

From the computational data obtained, a series of vortex cores within the stall cell were identified (Fig. 2.10) which contradict the flow models presented by both Winkelmann and Barlow (1980) and Yon and Katz (1998). In these predictions the vorticity due to separation is localised within the bounds of stall cell forming two counter-rotating loops. In this work, however, a pair of trailing vortices are identified which the authors conclude to be those which form the bounding vortices of the structure.

Separation on an aerofoil provides an upper limit to an aerofoil's achievable performance in terms of both reduced lift and increased drag. For a turbulent aerofoil, the reduction

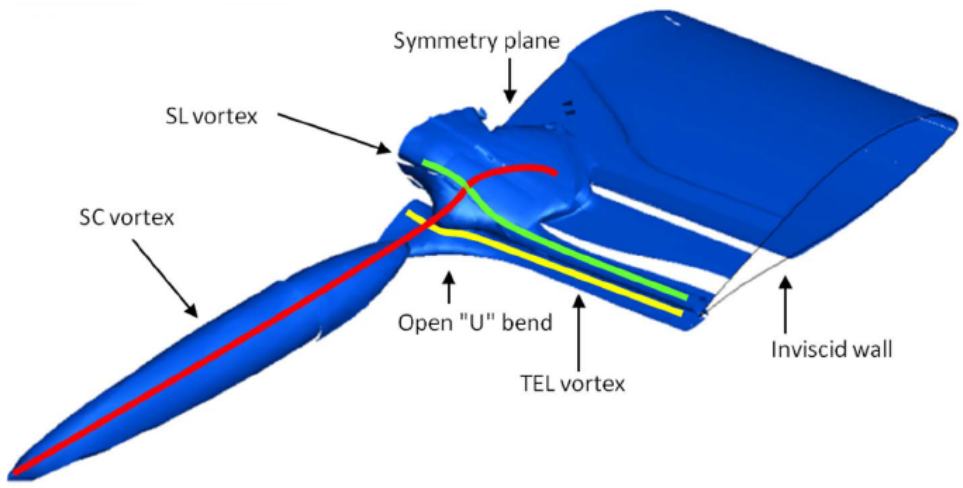


Figure 2.10: Identification of: separation line (SL), trailing edge line (TEL), and stall cell (SC) vortices from RANS data (Manolesos and Voutsinas, 2014)

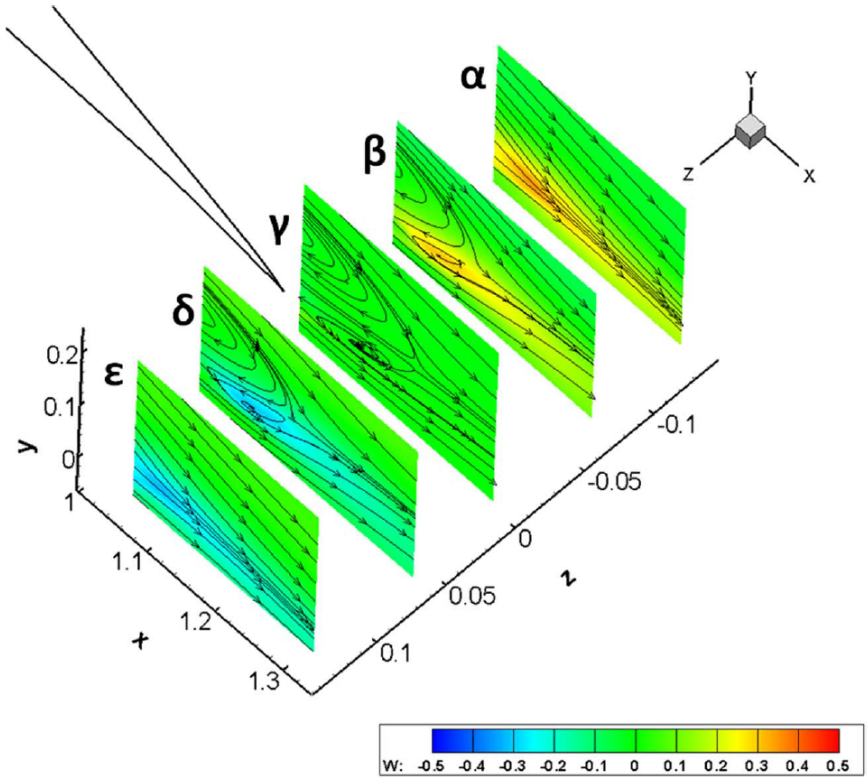


Figure 2.11: SPIV of a stall cell (Manolesos and Voutsinas, 2014)

in lift in the post-separation region of the C_L/α curve is modest, as shown in Fig. 2.6(b), however the shedding of vorticity causes the loading to fluctuate. Oscillatory structural loading is highly undesirable and introduces detrimental effects for both component fatigue design and vehicle control. The drag increase in the same region is many times larger than the reduction in lift and frequently the most significant performance limitation. Controlling separation is therefore of significant interest to a number of industries and so a sizeable body of research has been undertaken which will be reviewed in the following section.

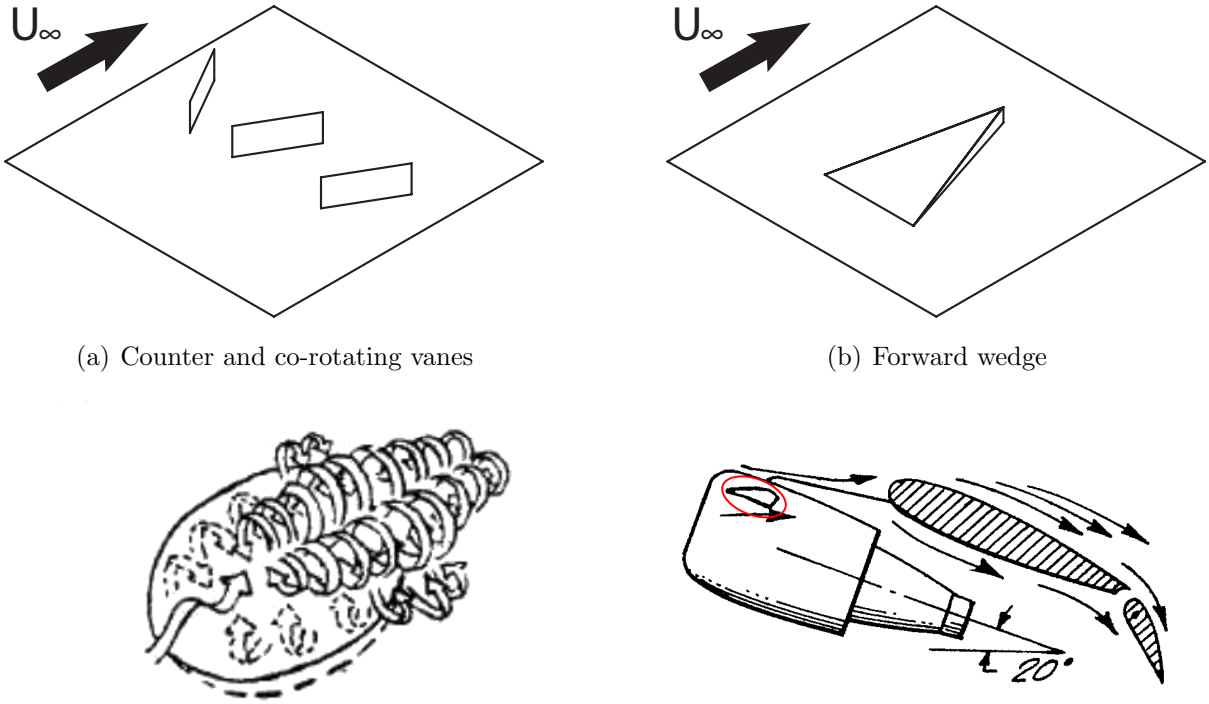
2.1.4 Separation Control

Many technologies that exist for the control or prevention of separation are demonstrated in the literature. Before these are discussed it is important to note that, as shown above, separation is fundamentally caused by insufficient momentum in the near-wall flow to overcome an adverse pressure gradient. Independent of the exact method used, all separation control devices must necessarily re-energise the flow adjacent to the wall. In the following discussion the control methods will be separated into those passive systems where the control device requires no ongoing energy input to function; or active systems with a more-or-less continuous energy requirement.

Passive Flow Control Devices

The most common separation prevention device is the passive Vortex Generator (VG). They are conceptually relatively simple and a large body of research has been conducted in the field to date (for a comprehensive review on the subject see Lin (2002)). Introduced by Taylor and Hoadley (1948), these devices, typically of height ($0 \leq h/\delta \leq 2$), are positioned upstream of the anticipated separation region and are designed to produce streamwise vorticity near the wall. Figures 2.12(a)-(d) show a selection of the many designs which have been developed for use in this role to date.

While there are many differences between each specific case, they can be summarised as a spanwise variation in the fluid boundary, which produces spanwise pressure gradients so introducing streamwise vorticity to the flow as discussed in (Sec. 2.1). The effect of this is to mix fluid from a distance away from the boundary into the near-wall region (Logdberg, 2006). The additional momentum in the boundary layer can overcome a more significant



(a) Counter and co-rotating vanes

(b) Forward wedge

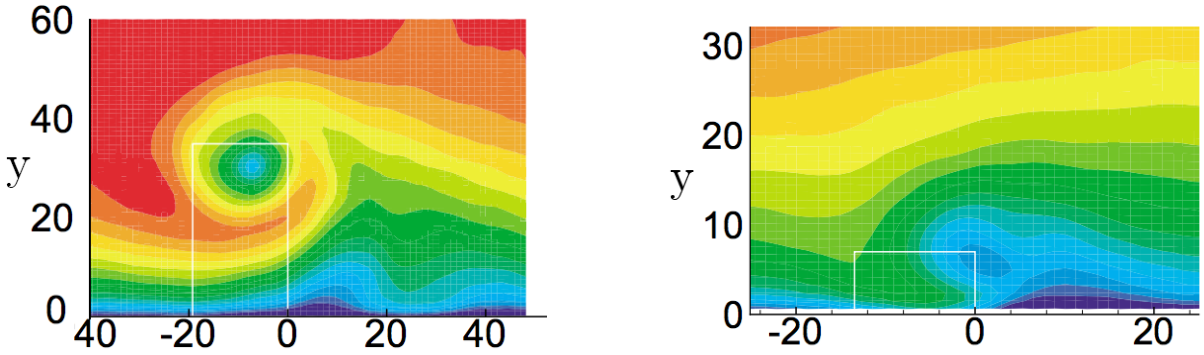
(c) Dimple

(d) Nacelle Chine

Figure 2.12: Examples of vortex generators: (a) Counter-rotating and co-rotating vanes; (b) Wedge-type; (c) Dimple (Ligrani et al., 2001); and (d) Engine nacelle chine (circled)(Kerker, 1973)

adverse pressure gradient than the baseline flow, thus delaying separation. These devices are typically positioned upstream of regions prone to separation and spaced periodically with spacing normalised by a device height of $4 \leq \Delta z/h \leq 13$ (Lin, 2002).

While delaying separation from a wing can be a safety-critical function, as passive devices, vortex generators must be present at all times during flight regardless of the level of requirement. Therefore during cruise, when the risk of separation is low, a vortex generator continues to introduce streamwise vorticity to the flow, thickening the boundary layer and increasing parasitic drag. In some cases it is possible to minimise the effect of a vortex generator during normal operation and produce vorticity only at specific point in the flight envelope. The control of flow over an aircraft jet turbine nacelle is one example of this design (Fig. 2.12(d)). When operating in a high lift configuration, the flow over the wing in the region around the nacelle is adversely affected by the nacelle itself. To overcome this, a strake (or chine) is positioned on the nacelle oriented in the nominal



(a) Conventional VG

(b) Sub Boundary-Layer VG

Figure 2.13: Streamwise velocity distribution recorded downstream of Vane-Type VG inclined at 16° to the flow (Yao et al., 2002)

streamwise direction. When the aircraft incidence alters to a high lift configuration, the vortex generator is now at an angle to the free-stream and so induces streamwise vorticity, delaying separation (Kerker, 1973).

Kuethe (1972) investigated the use of small ($h/\delta \leq 0.65$) so-called Sub Boundary-Layer Vortex Generators (SBVG) as a method of reducing the acoustic impact of an unsteady aircraft wake. It has since been found that SBVG produce a higher level of performance, as measured by the ratio of induced circulation and drag, than larger components as the effect is confined within the boundary layer and the coherent vortex decays faster from the smaller variants. This decreases boundary layer thickening, corresponding to a lower parasitic drag relative to the larger variants (Lin, 2002). This was confirmed experimentally by Yao et al. (2002) in a comparative experiment between conventional and low-profile VG on a flat plate with zero pressure gradient (Fig. 2.13).

Active Separation Control

Unlike the devices outlined above, active flow control systems require additional power and then inject that energy into the boundary layer to reduce the momentum deficit near the wall. The most direct form of this type of control is that provided by the Blown Jet (North, 1976). Here, fluid is drawn from elsewhere on the body and pumped, at high velocity, directly into the boundary layer where it mixes with the existing fluid, increasing the overall momentum in the flow. The opposite fluid path has also been used for separation control: boundary layer suction (Poppleton, 1951). In this case the low velocity fluid near the wall is removed with suction and expelled elsewhere. The

remaining high speed flow from the freestream is drawn towards the wall and forms a new boundary layer. Both of these methods require both a large amount of energy during operation and a mass flux through the surface, and the associated fluid paths, which must be considered during the design.

An alternative to these early active systems was the proposal of oscillatory blowing (Seifert et al., 1993) to re-energise the boundary layer. From this work the Zero Net Mass Flux (ZNMF) or synthetic jet actuator was developed. These devices operate in an oscillatory fashion by drawing air from the boundary layer through a slit or hole in the wall into a diaphragm and then expelling it rapidly. The expelled air forms a coherent jet, the effect of which is observed a large distance from the wall (Glezer and Amitay, 2002). The resulting flow patterns encourage mixing in the boundary layer and separation control is achieved. These devices have been demonstrated widely and require little additional infrastructure to implement, making them very attractive for commercial applications. The current research focus is on reducing the weight impact of these devices to a point at which they may be seriously considered for deployment. The necessity of a break in the skin through which the jet can act is, however, a limitation of their use in many future applications. A strong emphasis is being placed on maximising the area of a wing with a laminar boundary layer during flight as a drag reduction mechanism for future aircraft. To maintain a laminar flow on a surface, exuberances must be minimised as steps and gaps as small as $h \approx 20$ μm have been shown to promote transition (Duncan et al., 2013).

Plasma-based actuation systems have also been proposed for motivation of the boundary layer. These actuators are attractive as they have no moving parts and require no break in the aircraft skin, relying instead on an oscillating electric field to produce a low temperature plasma within the boundary layer. The rapid expansion of the fluid, and resulting shock waves, promote the required momentum transfer through the boundary layer (Roupassov et al., 2009). The adoption of this technology is limited by the high voltages required within the system, $V = \mathcal{O}(10)$ kV, and the low efficiency due to the power required to create the plasma.

The use of passive dimples has long been known to reduce the extent of separation, and so drag, on a body. In their work on the drag reduction of a cylinder, Udovidchik and Morrison (2006) and Dearing et al. (2007) demonstrated the use of active dimples, a spanwise array of electro-active polymer actuators which periodically vary from a smooth surface to a hemispherical depression with depth $d = \mathcal{O}(\delta)$, for delay of separation at

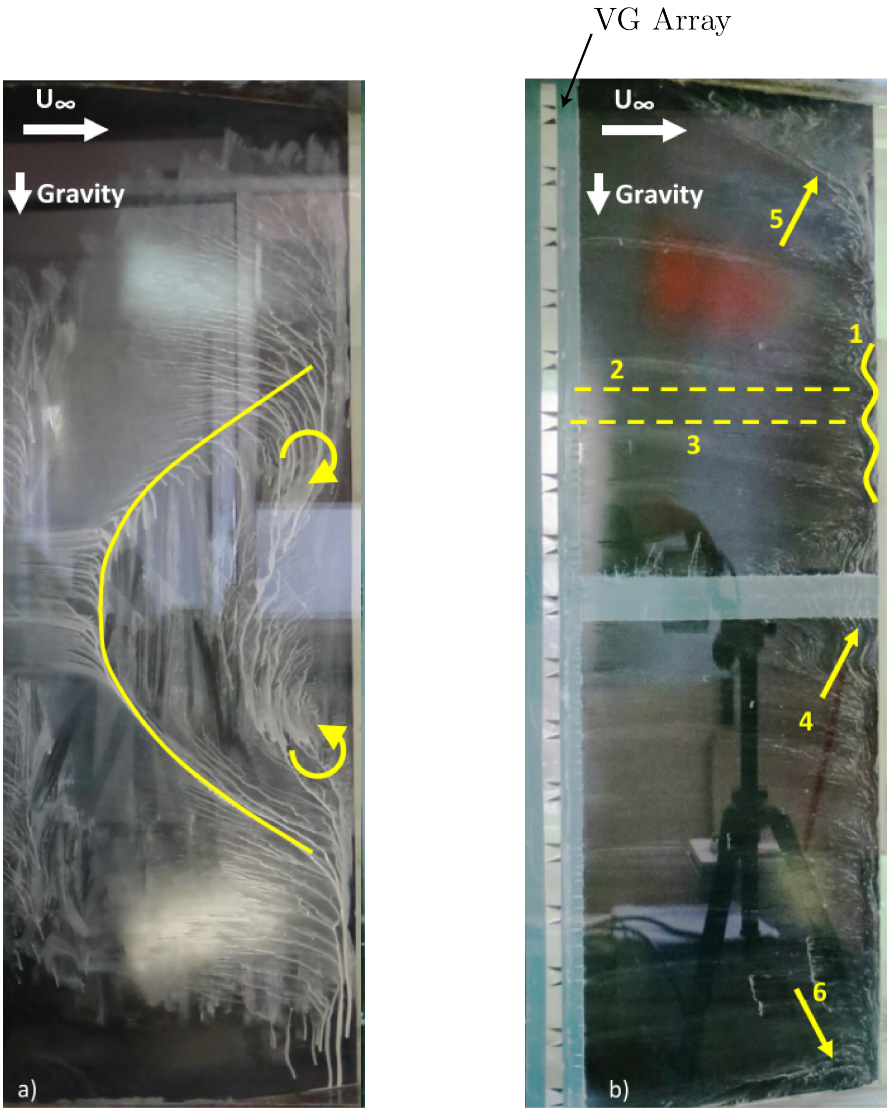
$Re = 2.2 \times 10^5$. When forced at $St = 0.26$, near to the natural shedding frequency, the separated region retreated by $\approx 10°$ demonstrating the potential of dimples for spanwise vorticity generation on an experimental surface, and so separation control.

Control of Three-Dimensional Separation

Throughout the literature on the separation control reviewed above, the authors assume that the flow separation is purely two-dimensional with a bluff-body like wake.The proposed approach towards actuator placement then follows a similar 2D methodology with a prescribed spanwise array with constant spacing recommended. Following their earlier work on stall cells, described above, Manolesos and Voutsinas (2015) have investigated the specific reduction of a stall cell using passive devices.

A spanwise array of vane-type vortex generators was applied to the model at $x/c = 0.3$ with height $h = \mathcal{O}(\delta)$ and spanwise period $D = 11.7h$. Oil flow visualisation and mean pressure measurements revealed that this control reduced the upstream separation extent from $x/c \approx 0.5$ to $x/c > 0.95$ at $\alpha = 10°$. Subsequent analysis of the time series of pressure measurements identified a bifurcation of flow states at $\alpha = 16°$ which was not seen at lower incidences. The predominant flow remained attached until $x/c \approx 0.55$; however for distinct intervals the flow reverted to that of the uncontrolled state, separating at $x/c \approx 0.3$. The authors do not draw any specific conclusions from these results nor is any characteristic frequency of occurrence identified. While this work directly acknowledges the presence of 3D separation on the model, the control method remained independent of the known topology of the skin friction lines.

Given the highly three-dimensional structure of turbulent separation it is proposed that the most efficient methods of its control would also vary in the spanwise direction. It also follows that, given the periodicity of stall cells reported, such a 3D actuation pattern would also be spanwise periodic. This will be investigated further in Chapter 7. However, as reviewed above, while the flow topology is periodic, the size of the cell and so the spanwise length scale varies with the flow conditions. In order to maximise the efficiency of the actuation it is therefore necessary for each actuator to revert from the controlled to uncontrolled state when not required. This can be achieved with any of the active methods described above; however, these all contain drawbacks and so an alternative actuation method is desirable.



(a) Baseline Flow (b) With VG

Figure 2.14: Reduction of a three dimensional stall cell using a 2D array of vane-type VG (Manolesos and Voutsinas, 2015)

2.2 Compliant structures

In all but the most trivial of systems, the relative movement of at least one component with respect to others is required. In traditional mechanical design each component is considered nominally rigid (Uicker et al., 2010), and so in order to achieve the necessary movement, the assembly is split at a point. Additional components are then added to provide a degree of freedom to the design. This mechanism allows the desired rigid-body motion in the structure without introducing material strain and so without breeching the rigid body assumption.

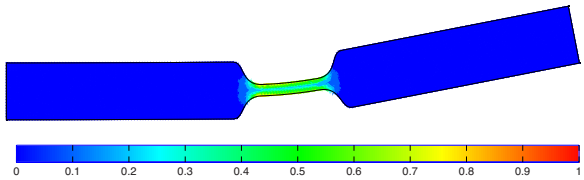
This design methodology is both mature and robust. Examples of its use can be found in nearly all complex systems. Two significant drawbacks associated with the use of mechanisms are derived from the need for additional components: the increased failure rates derived from the larger number of components and so decreased reliability of the system; and the increased size and weight of the design which must transfer the structural loading through additional discrete components. In many applications these are of limited consequence. However they are of particular importance in the aerospace industry due to the opposing requirements of safety and efficiency (Kota et al., 2003).

In recent years the drive for miniaturisation of products has caused a steady growth in the research into the use of compliant structures to replace mechanisms. Such structures use the compliance of the constituent material and the topology of the component to achieve the target deformation under actuation. The structural compliance may either be concentrated, through a local thinning of the material (Fig. 2.15(a)), or distributed through the entire structure (Fig. 2.15(b)).

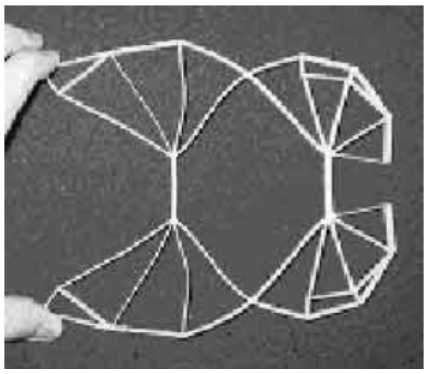
The use of adaptive structures allows the simplification and lightening of an assembly at the expense of an increased part complexity. In aerospace applications the use of adaptive structures to alter the geometry of the aircraft is given the term *morphing* and this specific application will now be reviewed.

2.2.1 Morphing Aircraft

When considering the design of an aircraft wing the performance, as measured by a role specific metric, across a number of scenarios within the flight envelope will be considered. The final design is therefore the result of a multi-objective optimisation problem with a



(a) A 'Living Hinge' with localised structural compliance due to selective weakening of the structure (Weisbord and Paros, 1965).

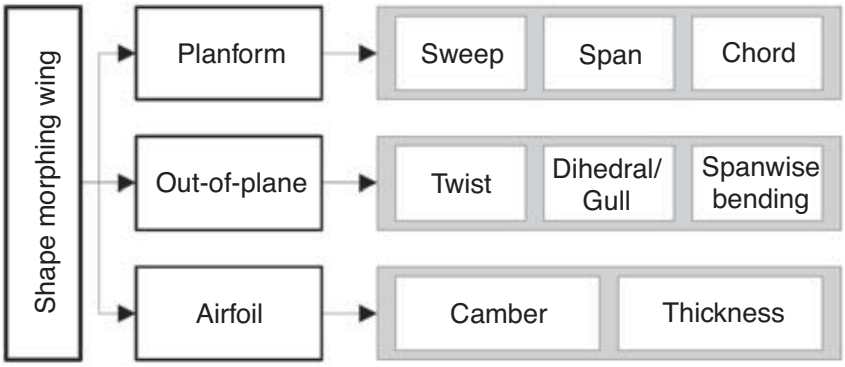


(b) Monolithic gripper demonstrating distributed compliance (Kota et al., 2003)

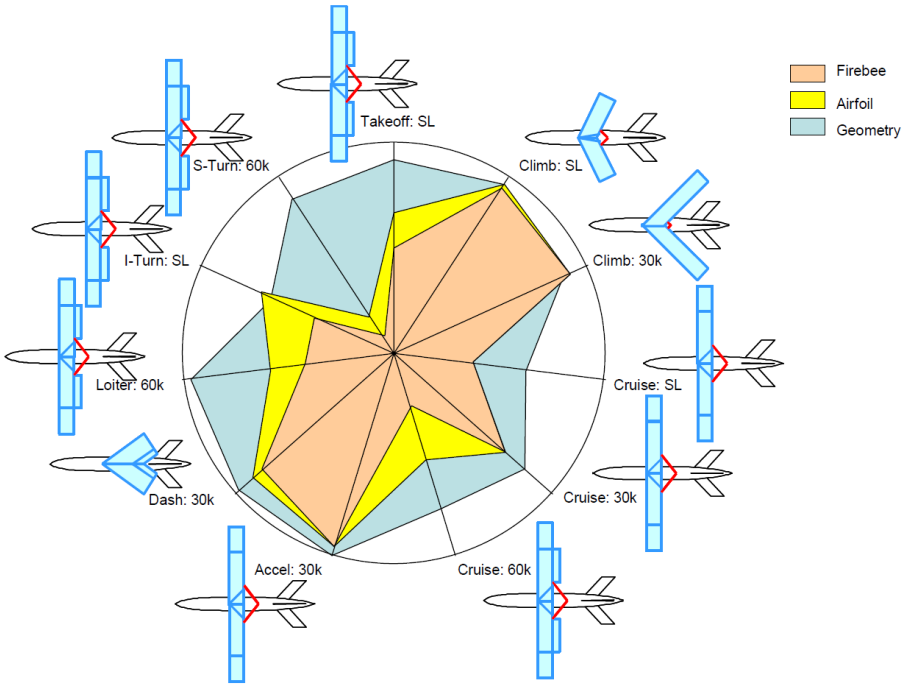
Figure 2.15: Examples of compliant mechanisms incorporating: (a) concentrated compliance, and (b) distributed compliance

high number of variables including: wing span, sweep, twist and profile. The optimal solution, found at the Pareto point, in the objective space represents the design parameters which provide the ideal compromise between all objectives subject to the design constraints.

The quasi-rigid body approach to design of the wing allows the profile, determined from the flow, and structure, based on loading, to be considered independently, however it also forces a compromise on the final airframe geometry. Since the optimal geometry will vary with conditions, the requirement to fix to a single, broadly acceptable, geometry prevents the achievement of an aerodynamic optimum at any individual point in the envelope. Mechanical components to mitigate the extent of this compromise in geometry are frequently included in the design such as: systems to deploy additional lifting surfaces and vary the wing camber; or fixed components to modify the flow and improve off-design performance. While these additions increase the overall efficiency of the aircraft, the additional penalties such as an increase in weight or drag, or physical design constraints, limit their effectiveness. While these systems may be considered types of adaptive structure, a distinction is drawn between the change between discrete states as provided by traditional mechanical systems and the continuous variation offered by an adaptive structure. The use of adaptive structures in an aircraft enables the broadening of the achievable design space which is accompanied, in commercial applications, by significant efficiency gains.



(a)



(b)

Figure 2.16: (a) Varieties of morphing technology (Barbarino et al., 2011) and (b) potential applications (Joshi et al., 2004)

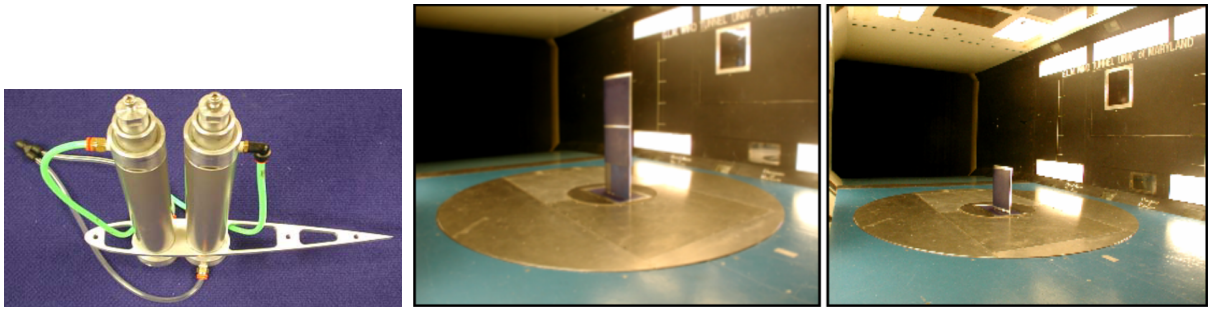
A large body of research has been conducted on the application of morphing components in aircraft since the use of wing warping on the first powered heavier-than-air craft, the Wright Flyer (Culick and Jex, 1985). Depending on the mission profile of a given aircraft the variation of any of the design parameters, which are fixed in a traditional approach, may result in an improvement in the relevant performance metric. As such, the research into morphing aircraft covers many different aspects of wing design and can be broadly split, as shown in Fig. 2.16(a), into three categories: planform, out-of-plane, and profile change. In their development of the morphing aircraft *Firebee*, Joshi et al. (2004) grade the effectiveness of either geometric (planform or out-of-plane) or airfoil (profile) change in adapting between different aircraft configurations, this is presented graphically in Fig. 2.16(b).

The focus of this work is on the enabling technologies proposed for use in morphing applications, many of which are common between the different categories. As such a brief overview of each category and its application will be provided before the common limitations to morphing performance are highlighted. A number of solutions have been proposed to overcome these challenges and these are investigated below. For a detailed review of individual morphing proposals, experiments, and results the reader is directed to those produced by Barbarino et al. (2011) and Gomez and Garcia (2011).

Planform Morphing

Planform alteration is principally concerned with a vehicle which is required to achieve both a high endurance loiter phase, requiring a highly efficient low-speed configuration, and a high-speed dash capability with high manoeuvrability, requiring low drag and high wing loading. This can be achieved by varying the span or chord of the wing, altering both wing loading and induced drag (McCormick, 1995).

A variable span model was first implemented by Blondeau and Pines (2004) with the replacement of the wing spars with pneumatic pistons connected to a sliding outboard section of wing (Fig. 2.17). The sliding wing in this instance was found to significantly under perform in the extended position and this was concluded to be due to both the reduced rigidity of the wing spars and skin, and the joints in the aerodynamic surface needed for the sliding mechanism. Henry (2005) used the same wing model to demonstrate the use of variable span wings to provide roll control which removes the associated increase in weight and parasitic drag, thus further increasing the efficiency of the morphing aircraft.



(a) Planform Actuators (b) Planform Testing

Figure 2.17: Variable span wing section produced by Blondeau and Pines (2004)

Several authors have since attempted to correct the performance under-delivery by improving on either the structure or skin of the concept. Joo (2006) investigated the positioning of actuators within a scissor mechanism to provide a similar elongation but with distributed actuation throughout a scalable array of unit cells. Depending on the impact of compressibility in the high speed configuration variable sweep, such as that used on the Grumman F14-A and Panavia Tornado production aircraft, may be included in the variation of span to further reduce drag. The NextGen batwing (Bowman et al., 2007) used a similar distribution of actuators within a 4-bar mechanism to that developed by Joo (2006). Instead of pure span morphing, the linkages were arranged to provide a combination of span and sweep change. During flight tests the UAV was able to change sweep angle by 20° and span by 30% mid-flight.

Out-of-Plane Morphing

Adjustable twist wings, or warping wings, were originally used in early aircraft to provide roll control by varying the local incidence angle and producing a net moment on the vehicle. As aircraft developed, and wing loading increased, the wing structure required did not allow sufficient rotation to provide control authority and ailerons replaced warping as the primary method of roll control.

The renewed interest in varying wing twist has been largely driven by the proliferation of low speed micro air vehicles (Gomez and Garcia, 2011). For such very light aircraft, operating at low Reynolds numbers where thin aerofoils are suitable, the increased complexity of distinct control surfaces at the extremity of the wing span is structurally expensive. Conversely, the thin aerofoil profile only requires a small moment to create a significant

deflection and this can be produced in the aircraft fuselage and transmitted to the wing tips through a lightweight torque rod (Garcia et al., 2003).

Wing twist control has also been used to amplify the roll authority of control surfaces on very high speed aircraft. At large dynamic pressures, the control provided by ailerons alone is insufficient to provide the rate of turn required by modern military aircraft. Instead, work by Miller (1988) showed that, by reducing wing stiffness near the ailerons, the aeroelastic effects increased roll authority for high speed manoeuvres. Following this, Griffin and Hopkins (1997) and Chen et al. (2000) have presented designs for variable stiffness spars whose torsional rigidity can be altered on demand, passively twisting the wing and increasing control efficiency.

Although categorised separately by Barbarino et al. (2011), gull wings and the variation of wing dihedral can both be considered a form of spanwise bending which is localised at either a location along the span or at the wing root respectively. These designs are largely bio-inspired and so mimic the variation in wing topology exhibited by birds during flight. Altering the dihedral allows a similar alteration to the effective wing planform as the morphs discussed above but without a large change in wing surface area. However, due to the technical challenges posed, relatively few experimental models have been produced.

The Lockheed Martin Z-Wing aircraft concept (Bye and McClure, 2007) used folding wings to provide span morphing capability. The system was originally actuated with shape memory alloy based actuators however, after poor performance in cyclic tests, these were replaced with mechanical drives. A carbon-elastomer composite 'sock' similar to traditional carbon fibre panels was used to provide a seamless skin (Fig. 2.18). To manufacture the skin, the resin normally used with carbon was replaced with a silicone compound providing a surface which allowed flexibility without elongation.

Profile Morphing

The variation of an aerofoil profile during flight has received the most research of any morphing category due to its wide-ranging applications (Barbarino et al., 2011). The changing requirements of take-off, climb, cruise or loiter, descent, and landing are common to all aircraft and require significantly different performance characteristics due to changing speed, fluid properties and wing loading. Altering the aerofoil profile allows the optimal performance, to a role specific metric, at each stage of flight based on the local flow conditions. This is commonly achieved on traditional aircraft through the



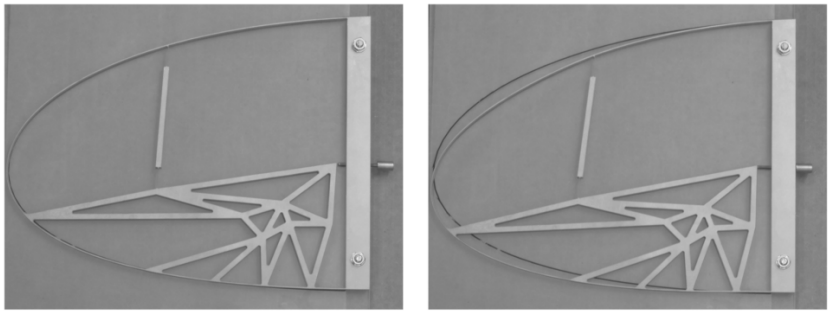
Figure 2.18: Lockheed Z-Wing Demonstrator (Bye and McClure, 2007)

deployment of slats and flaps from a wing section to change from cruising to a high-lift configuration. The use of compliant structures in this role aims to achieve the same effect on aircraft performance without the parasitic drag penalty which accompanies any gaps, steps or voids in an aerodynamic surface.

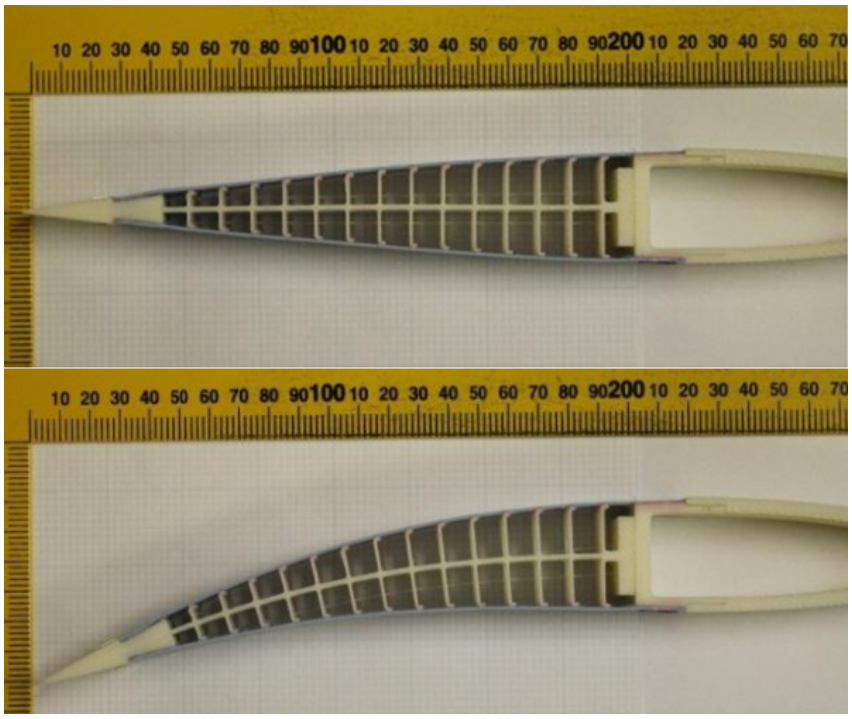
The design methodology and demonstrator for a 5° camber change in the leading edge section of an aerofoil was presented by Santer and Pellegrino (2009) (Fig. 2.19(a)). A load-path-based topology optimisation was applied to an initially seeded internal lattice structure to produce an optimised support structure which can produce a defined, elastic, camber morph in an aluminium cross section. The topology optimisation allows the actuation from a single internal point to be distributed through the load path with lowest mass for the intended morph.

Figure 2.19(b) shows a bio-inspired concept for a morphing trailing edge called *fishBAC* (Woods and Friswell, 2012). The actuation is provided by two antagonistic 'tendons' situated either side of the central spine. An impermeable pre-tensioned elastomer skin provides a clean fluid boundary without restricting the displacement of the profile. The presented deflection can be reproduced symmetrically and represents a camber change from 0 to 13.3% of the chord length.

In addition to reproducing the systems currently in service on traditional wings, the con-

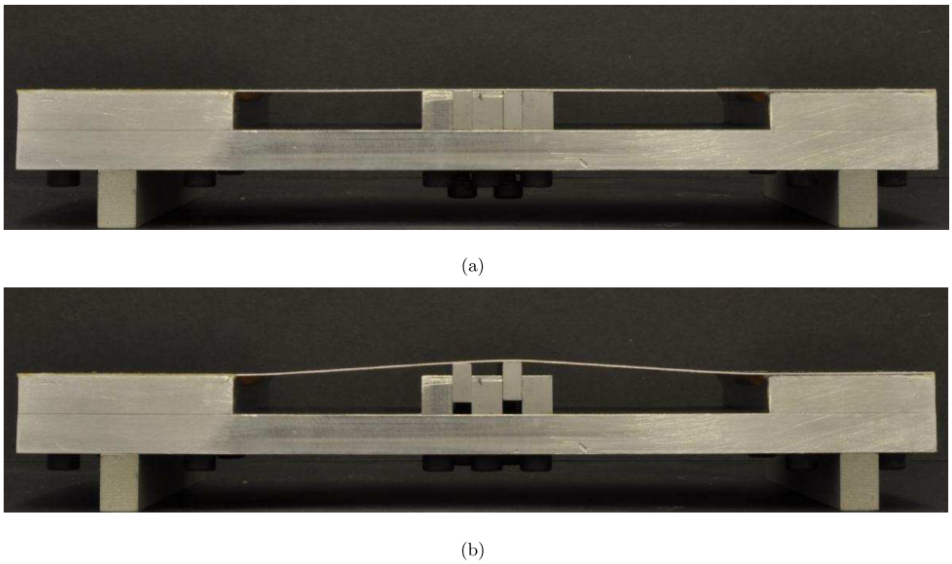


(a) Leading edge morph (Santer and Pellegrino, 2009)



(b) Trailing Edge Morph (Woods and Friswell, 2012)

Figure 2.19: Profile morphing achieved through structural compliance



(a)

(b)

Figure 2.20: 2D morphing transonic shock control bump by Rhodes (2012)

sideration of adaptive structures in a design can allow performance enhancement which traditional systems are unable to offer. Bernhammer et al. (2013) proposed using the continuous variation of wing camber, available only to an adaptive structure, to alleviate gust loading on the airframe. The subsequent reduction in structural requirements resulted in a decrease in wing weight, providing a further efficiency benefit.

Rhodes (2012) presented an adaptive wing profile for reducing the wave drag of a transonic aerofoil operating at off design speeds. The development of 2D shock control bumps onto a wing profile alters the shock structure, reducing the total pressure loss in the system. Using two actuation points a demonstrator was produced (Fig. 2.20) which closely matched the FE predictions. In the same work Rhodes attempted the production of a 3D (finite in the spanwise direction) shock control bump but found that the overall deflection was severely limited by the production of in-plane strains.

A common argument against the use of morphing wing profiles is the additional weight required for the adaptive structure which must be over-engineered in order to accept the bending loads required for actuation as well as the anticipated structural loads. However, the combination of potential benefits at many operating points means profile morphing remains a particularly attractive option for future aircraft. While a large variety of morphing structures have been proposed, all require a skin which is a balance between flexibility, to allow the morph to be elastic, and stiffness, to transfer the aerodynamic loads to the wing structure.

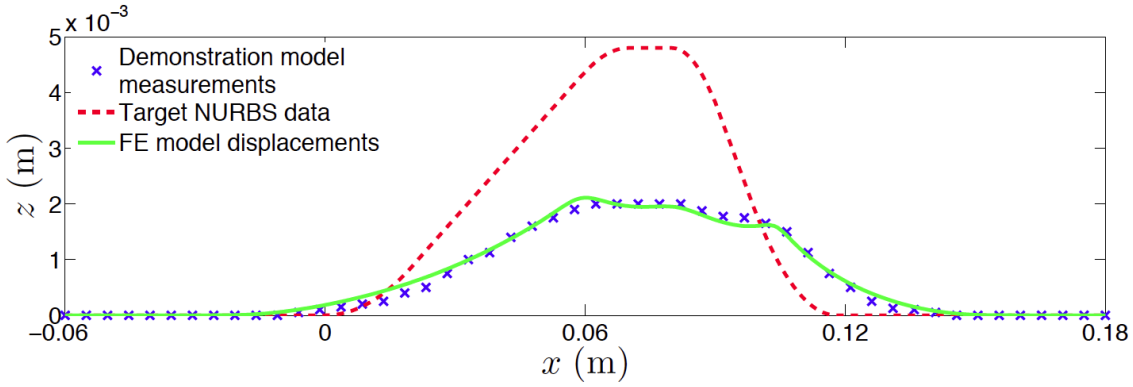


Figure 2.21: Three dimensional geometry produced by Rhodes (2012) showing 40% of target deformation – streamwise cross-section shown

Local Profile Morphing

Examples of three-dimensional morphing are rare, with two notable exceptions. Arrieta et al. (2013) developed an adaptive winglet concept which used a bistable material to provide two distinct states of actuation. The surface could either act as a thin wingtip span extension or sit perpendicular to the wing and therefore behave as a winglet to reduce circulation losses. The actuation of the device between each state was enacted by exposing the surface to vibrations from an actuator. As the two stable geometries have different natural frequencies, oscillating the surface with the frequency of the unwanted state will cause a rapid growth in oscillations until the strain energy potential required to switch states is reached and the structure snaps to the other stable state. The oscillations then have little effect on the desired state but provide a rapid correction if unwanted actuation occurs. This method requires the device to maintain surface area between states and is able to produce significant changes in geometry because the device is unrestrained on three sides.

A demonstration model of a three-dimensional shock control bump based on experimentally-derived geometry was produced by Rhodes (2012). In this work, Rhodes produced a finite element model and experimental demonstration from a 0.4 mm thick aluminium skin. The FE model closely matched the final morph but was only able to achieve 40% of the peak displacement levels in the target geometry (Fig. 2.21). This represents the current state of the art and underlines the challenges faced in this field.

2.2.2 Morphing Skins

In order to replace traditional mechanisms with an adaptive structure, it is necessary to ensure that the prescribed geometry change must be repeatable. It therefore must be achieved within the material's elastic limits. Much of the research above focuses on the internal morphing structure, however a suitable skin must also be considered.

When designing a profile change, the skin can be considered as a simple beam exposed to an external bending moment (Rhodes, 2012). Using Euler-Bernoulli beam theory, for small changes in curvature, it is assumed that the mid-plane of the beam of length l and thickness $t \ll l$ can be deformed to a deflection field w and that plane sections (normal to the mid-plane) remain plane after deflection (Love, 1888). For small deflections, without a change in length of the neutral axis, these assumptions allow the internal stresses for a change in curvature κ to be calculated. For a linear-elastic deflection of an isotropic beam, the stress a distance y from the neutral axis can be calculated with

$$\sigma_{_B} = \frac{My}{I} = -yE\frac{d^2w}{dx^2} = -yE\kappa \tag{2.19}$$

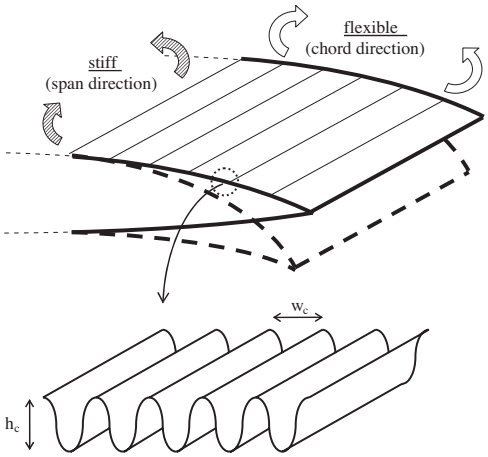
in which M is the bending moment, y is the perpendicular distance from the neutral axis, I is the second moment of area of the section, E is the material Young's modulus, and w is deflection perpendicular to the neutral axis.

For larger displacements, or deflection under fixed boundary conditions, it is necessary to include the effect of elongation of the beam length L in the solution. For a profile of constant section, the membrane stress $\sigma_{_M}$ caused by the in-plane strain ϵ_M occurs uniformly through the structure and can be found according to

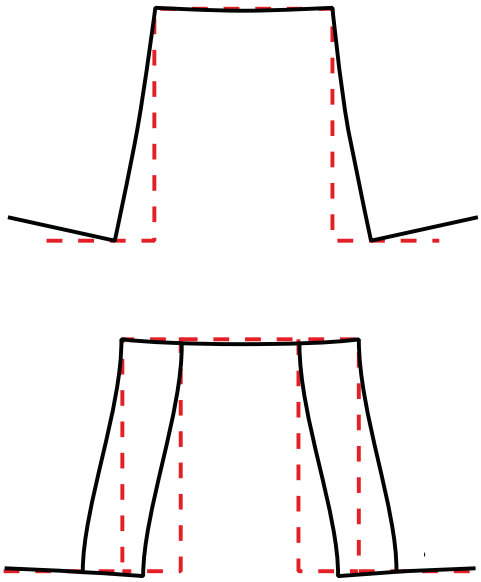
$$\sigma_{_M} = \epsilon_{_M} E = \frac{L_1 - L_0}{L_0} E \tag{2.20}$$

If the deformation is linear, the two components of stress can be considered independently and then combined thorough superposition. In the plane bending case, it is clear that the stress distribution through the cross section of the beam varies over the cross section of the surface. The maximum shear stresses occur on the outer surfaces and shear stress is equal to zero along the neutral axis at the mid-section of the surface. Conversely, membrane stress results from tension in the material and so acts uniformly across the section. The maximum total stress within the beam is therefore found at the plate surface where $y = t/2$ and is given by

$$\sigma_{max} = \sigma_{_M} + \sigma_{_{B_{max}}} = E\left(\frac{L_1 - L_0}{L_0} + \left|\frac{t}{2}\kappa\right|\right) \tag{2.21}$$



(a) Corrugated trailing edge section as proposed by Yokozeki et al. (2006)



(b) Improvement in out-of-plane deformation as a result of the double corrugation method (Previtali et al., 2015)

Figure 2.22: Corrugation to produce 'ultra-anisotropic' skins to increase profile morphing capability

The yield strain of a typical aerospace aluminium grade 7075-T6 is $\approx 0.6\%$. It is clear that a significant alteration in profile geometry cannot therefore be achieved through the elastic elongation of the material alone. However, as $t \ll l$, moderate local curvature changes can be achieved while the solution remains elastic. The effect of this local curvature change on material position is then integrated around the section resulting in a large, repeatable, deformation which may be used to modify the flow.

In order to achieve still higher levels of deformation, dedicated anisotropic materials have been proposed in which the bending and membrane stiffnesses vary with material orientation. Yokozeki et al. (2006) proposed the use of corrugated materials in flexible wings as a method of achieving a decreased actuation force while maintaining a high spanwise bending stiffness. In their experiments, Yokozeki et al. also achieved an increase in yield strain from 1% to 45% in the direction perpendicular to the corrugation although this value can be adjusted with the design of the structure. One highlighted limitation of this method, lack of control of the deformed shape under actuation, was addressed by the addition of a second corrugation by Previtali et al. (2015). In this double corrugation layout the bending moments which exist at each corner of the single corrugation are

transformed by the enclosed sections into shear and axial forces which do not cause the structure to deform out-of-plane. This allows a locally plane surface to be maintained which can then be skinned using a technique such as that proposed by Thill et al. (2010). In this work, a small section of skin is bonded to each corrugation to form a sliding layer which can accommodate the local change in surface length due to morphing but with a greatly reduced impact on the fluid boundary.

Bubert et al. (2010) proposed a carbon-filled elastomer skin attached to a supporting lattice with zero Poisson's ratio, developed by Olympio and Gandhi (2007), to provide a stiffened skin which could double its spanwise length without joints or a significant reduction of chord. Similar work by Chen et al. (2015) has been conducted using a different lattice topology which allows both the extension of the wing surface in span as well as a change in sweep angle.

While a significant quantity of proposals for whole wing or two-dimensional morphing have been proposed by previous authors, limited work has been conducted on the production of a local, isolated, deformation. From the previous comparable example, in-plane membrane strain is described as the limiting factor in reproducing the required geometry. Work to extend the range of achievable two-dimensional morphs has identified that the use of certain lattice structures, in place of uniform sections, for the skin of the structure can increase in-plane yield strain. Such an approach, tailored to the requirements of a local geometry change may provide a solution to the problems faced previously.

2.3 Objectives

Having reviewed the relevant literature on turbulent separation, and its control, it is evident that existing static devices are not optimal due to their negative impact when not required. A method of providing actuation only when, and where, necessary is therefore highly desirable. The principle aim of this study is therefore to develop an adaptive structure to reduce the extent of turbulent separation from a partially separated, three dimensional, wing. In order to achieve this the key objectives are to:

- Investigate the limitation of out-of-plane surface displacement in locally three-dimensional morphing geometries.
- Develop an aero-elastic optimisation process to identify the optimal, elastically feasible, morphing structure for re-energising a boundary layer.

- Investigate the internal pressure and velocity fields of the periodic separation pattern known as stall cells in order to identify the locations where actuation would be most effective.
- Combine the aero-elastic optimisation process with the understanding of the separation topology to provide control of a stall cell on a separating aerofoil using an adaptive structure.

Chapter 3

Numerical Methods

The design of an aerodynamic surface is a complex field with many design parameters; the varying of any one of which can have a significant impact on the final performance (Torenbeek, 1979). The use of one of these surfaces to fulfil an additional role, as a morphing structure, further increases the complexity. Using only experimental methods, it is not feasible to fully explore the design space and so a series of numerical analyses were conducted during this work. In order to identify the most efficient parameter values for a given objective, the process of numerical optimisation illustrated in Fig. 3.1 is employed. This chapter describes this framework and the methods used within it.

Initially, an optimisation algorithm selects a series of design parameters based on the results of previous iterations and the design constraints. The selection and behaviour of this algorithm are described in Sec. 3.1. In this work, the design variables describe a deforming surface, and the resulting deformation is calculated using the finite element analysis described in Sec. 3.2. The nodal positions following deformation are then passed to an objective function to reduce their performance to a scalar quantity. The objective functions are problem specific and so will not be specifically discussed in this chapter, instead are described alongside their applications in Chapters 5 and 7. For some applications, the influence of the deformed surface on the initial fluid flow is evaluated using computational fluid dynamics as described in Sec. 3.3. Once the objective is evaluated, any constraints which are nonlinear with respect to the design variables, and so complex to apply in advance, are included with a penalty function as described in Sec. 3.4.

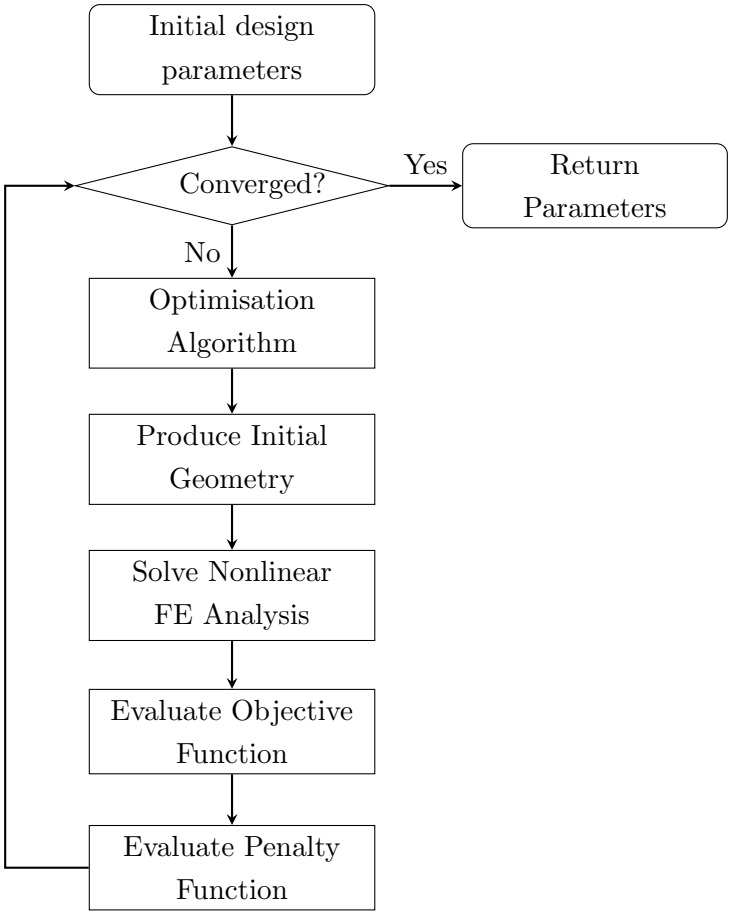


Figure 3.1: Flowchart of structural design optimisation process

3.1 Optimisation

There are two main branches of optimisation techniques which are widely used: classical, or gradient based, and heuristic methods. The first group starts with an identified location in the design space and then finds the local gradient of the objective function. A step is taken along the path of steepest descent, or ascent for a maximisation problem, and the new local gradient is computed. These steps are repeated until the local gradient is zero, indicating no further improvement can be made. Gradient-based methods allow a rapid convergence to the local minima, however they require a continuous function over which to operate. It is also assumed that the desired solution can be approached from the starting location and therefore that the starting 'guess' is suitable.

Unlike classical optimisation, heuristic methods rely on the evaluation of a large number of independent or loosely-related combinations of design variables. From these results

it is possible to identify either the optimal set of parameters directly or to find suitable regions of the design space in which to focus the search. These techniques provide a search of the design parameters without a need for any pre-existing knowledge of the objective space. The risk of either non-convergence or incorrectly identifying a local rather than global optimum are small. As a result of the comprehensive nature of these methods, the number of function calls increases geometrically with design parameters. Due to the relative expense of the objective functions which are used in this work, a large number of function calls is not computationally feasible and so a gradient based method has been selected for the current work.

3.1.1 Optimisation Algorithm

Initial design parameters $\mathbf{x}$ are selected to form the starting geometry from which the design is optimised. These variables contain sufficient information about the geometry and actuation to produce a unique topology and therefore resulting in a deformation field. This is used to calculate the objective function $S(\mathbf{x})$ to be optimised subject to a set of linear design constraints

$$\begin{aligned} &\min\left(S_H(\mathbf{x})\right) \\ \text{s.t.} \quad &\mathbf{x}_{_{LB}} \leq \mathbf{x} \leq \mathbf{x}_{_{UB}} \end{aligned} \tag{3.1}$$

The algorithm for conducting constrained optimisation problems which is used in this work has been implemented as the function *fmincon* in the MATLAB Optimisation toolbox Mathworks Inc. (2015). From an initial set of parameters $\mathbf{x_0}$, a sequential quadratic programming SQP method is used to carry out a search of the local space using the hill-climbing BFGS method (Nemec and Zingg, 2002). While the optimisation process is critical for the selection of a suitable parameter set, the algorithm itself is not the focus of this work and so the utility of a robust, commercial, solution has been employed. This function is used 'as-is', a full mathematical description will not be given and only a brief description of the process follows.

Constraints on the design parameters may be passed to *fmincon* either as: linear combinations of design variables forming equality or inequality conditions; or as nonlinear functions containing any other required operations. Any linear constraints which limit

the design parameter space are incorporated into an auxiliary Lagrangian function

$$L(x, \lambda) = S(\mathbf{x}) + \sum_i \lambda_{g,i} g_i(x) \tag{3.2}$$

where the function $g(x)$ contains the constraint functions and λ_g is the associated Lagrangian coefficient vector. The local gradient of L is calculated using finite differencing techniques and then a quasi-Newton approach is used to approximate the local Hessian matrix H_k

$$H_k(x) = \nabla_x^2 L(x, \lambda) = \nabla_x^2 f(x) + \sum_i \lambda_{g,i} \nabla_x^2 g_i(x) \tag{3.3}$$

at each major iteration k. This is then used to evaluate a step direction d_k

$$H_k d_k = -\nabla L(\mathbf{x}) \tag{3.4}$$

where $H_0 = 1$ for the first iteration. A line search is used to evaluate a step length α_k which either maximises the estimated improvement or, if this would breach a constraint, is the maximum allowable movement in the correct direction.

The objective is then evaluated at the new position and this process is repeated until the Jacobian of the objective $S(\mathbf{x})$ with respect to the design parameters, the first order optimality condition, is zero

$$\left|\nabla L(\mathbf{x})\right|_\infty = 0 \tag{3.5}$$

indicating a local critical point has been identified.

3.1.2 Linearisation of Constraints

The SQP method in *fmincon* imposes a strict feasibility requirement on the selection of design parameters with respect to the bounds supplied in the form of linear constraints or equalities for both. This requirement is applied for both main iterations and finite difference steps. This is especially important for this problem as, using non-analytical objectives, the objective may be undefined for parameter values beyond the bounds.

Nonlinear constraints are however handled using a different method and, as a result, are not strictly adhered to. To maintain robustness in the process these parameters must be linearised. For example, in Fig. 3.2, if selecting the actuation point x_a on the line with variable endpoints x_1 and x_2, the trivial inequality constraints $\mathbf{c}$ on x_a are given by

$$c_1(x_1) \leq x_A \leq c_2(x_2) \tag{3.6}$$

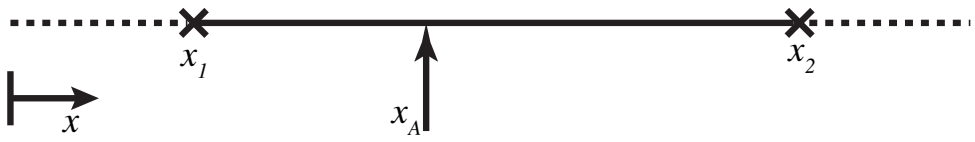


Figure 3.2: Nonlinear constraint example

and are clearly nonlinear, hence not strictly maintained within the algorithm. To circumvent this, x_a is redefined using an independent parameter s

$$x_A = x_1 + s(x_2 - x_1) \tag{3.7}$$

where: $0 \leq s \leq 1$

3.2 Finite Element Analysis

Once the design parameters have been generated by the optimisation algorithm, the displacement field following actuation is determined. The commercial finite element package Abaqus (Dassault Systemes, 2013) is used to conduct a finite element (FE) analysis of the actuated surface. Due to the impact of membrane stresses on the production of morphing geometries, all calculations account for the geometrically nonlinear effects of material extension which result from out-of-plane shape change.

The solution is obtained using an incremental implicit solver which linearises the nonlinear equations of motion at each step using the Newton-Raphson method. The step size is altered automatically to reduce the computational efficiency and the result is judged to be converged when the residuals for all variables are below 1×10^{-4}. Depending on the type of structure being considered, either shell or beam elements are used throughout the course of this work, both methods are described in the relevant sections. Depending on the objective function used, the nodal positions of the deformed geometry may be sufficient to conduct the optimisation. For more complex objectives, details of the resulting flow field are required and this data is obtained using Computational Fluid Dynamics (CFD) and the details of theses simulations now follow.

3.3 Computational Fluid Dynamics

In order to quantify the aerodynamic effect of the surfaces calculated using the methods detailed in the previous section, Computational Fluid Dynamics (CFD) simulations are incorporated into the objective function in Chapters 5 and 7. A brief overview of the methods employed will be given before the simulation techniques used in this work are described.

Regardless of the precise method used for solving the flow field computationally, the governing Navier-Stokes equations for incompressible flow remain the same. The Reynolds decomposition of a fluid velocity field proposes that, for any flow, the value of u can be defined as

$$u = \bar{u} + u' \tag{3.8}$$

where $\bar{u}$ and u' are the mean and fluctuating components respectively. It is the method of calculating the presence, distribution and effects of these fluctuating components, and hence u, which separate the most common computational methods.

RANS solutions attempt to find a solution for the mean velocity field and so use Eq. 3.8 to separate the components of the Naiver-Stokes equations into steady and unsteady terms

$$\bar{u_j}\frac{\partial \bar{u_i}}{\partial x_j} = \bar{\phi_i} + \frac{\partial}{\partial x_j}\left[-\frac{\bar{p}}{\rho}\delta_{ij} + \nu\left(\frac{\partial \bar{u_i}}{\partial x_j} + \frac{\partial \bar{u_j}}{\partial x_i}\right) - \overline{u_i' u_j'}\right] \tag{3.9}$$

where δ_{ij} is the Dirac delta function and all other variables are as previously defined. It can therefore be seen that all terms are functions of mean value with the exception of the Reynolds Stress tensor $-\overline{u_i' u_j'}$.

The contribution to the momentum equations of this term are incalculable from the steady values alone and so it is instead modelled using a numerical turbulence model. A variety of models are available with varying complexity. However a thorough review of the techniques used is beyond the scope of this work. Typically, models use an additional set of parameters which contain information about the turbulence levels within the flow and from which the influence of fluctuating velocities can be estimated.

These models are developed for a wide variety of flow conditions and, by their nature, attempt to reproduce a complex system with a simpler system. Detail is therefore lost at the expense of computational efficiency. For many cases, this is an acceptable trade off. However, for a system operating within a boundary layer, where nonlinear viscous terms dominate, such models are dependent on modelling assumptions.

The separation of a turbulent boundary layer from a curved surface is a difficult numerical problem to solve and RANS simulations, are not able to accurately capture the post-separation dynamics. An extension to this method adds time-marching to the solution, allowing a level of unsteady dynamics to be captured, and is termed unsteady RANS (URANS). The evaluation of turbulent fluctuations, fundamental to the behaviour of many non-trivial flows, still rely on RANS closure models and thus do not significantly gain in accuracy.

One alternative is to attempt to calculate the exact numerics of the system, including all small fluctuations. Such Direct Numerical Simulation (DNS) studies exist for small scale flows, such as that through a channel, however the computational grid size and time step implications mean that these simulations are not yet feasible for larger, application based studies. To produce a model with a greater accuracy than RANS but without the computational cost of DNS, it is possible to improve the accuracy of the modelled turbulence by exploiting the differing behaviour between large and small scale eddies. Such simulations only partially resolve the turbulent motion and the remainder is modelled using a simpler turbulence model. These simulations are termed Large Eddy Simulations (LES) and the rational for this approach will now be discussed.

Large scale eddies, formed as a result of the pressure and velocity gradients surrounding any immersed body, are highly dependent on the flow patterns around and across the wetted surface. They therefore have a length scale of the order of the characteristic length of the body ℓ_0. The energy of these large features is transferred to smaller scales which in turn feed yet smaller scales. This process only ends when a scale ν is reached at which the energy of the fluctuation is entirely dissipated by viscosity. At these smallest scales the fluctuations are statistically isotropic (Kolmogorov, 1941).

If the energy content of a typical turbulent velocity measurement is considered in terms of spatial frequency, then a profile similar to Fig. 3.3 is observed (Pope, 2009). From this it can be seen that the energy content of the flow is dominated by the large, anisotropic, scales. LES therefore aim to resolve these features fully and to only model the smaller, isotropic, structures which are easier to predict and so for which the modelling is more accurate. The Navier Stokes equations are therefore spatially filtered to separate the scales which can be resolved and a sub-grid model is used to provide the required closure from the unresolved components. In this work, the filter size Δ_{LES} is determined based on the mesh density

$$\Delta_{LES} = \sqrt{\Delta_x^2 + \Delta_y^2 + \Delta_z^2} \tag{3.10}$$

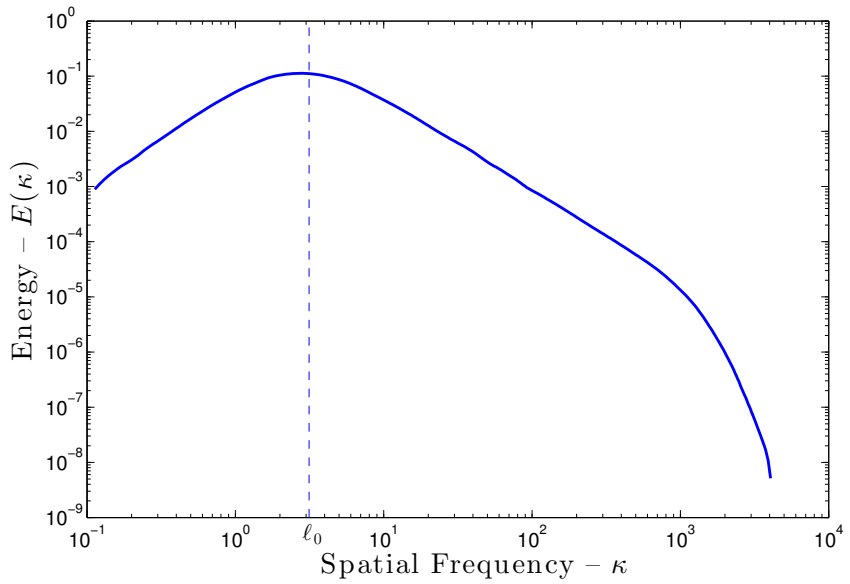


Figure 3.3: Typical spectrum of turbulent velocity fluctuations in the frequency domain (data from Pope (2009))

where Δ_x, Δ_y, and Δ_z are the grid spacing in each direction.

LES are unsteady and thus, if a mean value is sought, must be iterated in time until the mean flow field converges to the solution. In order to accelerate this process for use in optimisation, a RANS solution was solved for each case and used to initialise the flow field and start the LES. The turbulence model developed by Spalart and Allmaras (1992) and its LES sub-grid variant was used to provide closure for the momentum equations.

3.3.1 Solver Details and Boundary Conditions

The simulations used in this work are conducted using the open-source CFD toolbox OpenFOAM (*OpenFOAM*, 2013). The RANS SIMPLE finite-volume algorithm implementation, simpleFOAM, is used for the initialisation stage of each simulation. This is run for 1000 iterations, to form an initial estimate of the flow field before time-marching commences. Following this, the solution type is changed to LES and continued. The transient solution is solved using the general purpose pimpleFOAM transient algorithm. The time-step is variable to maintain a CFL = 1 at each step. This approach minimises the total solution time while maintaining accuracy of the flow field calculations.

The inlet boundary has a fixed uniform velocity into the domain. The inlet and initial

eddy viscosity ratios are set following the recommendations of Spalart and Rumsey (2007), where $\nu_t \approx \nu \times Re \times 2 \times 10^{-7}$ and the closure parameter $\widetilde{\nu} = 3\nu$. The upper and side walls of the model are prescribed with Neumann boundary conditions and the downstream boundary is a reference pressure outlet. Further details on the specifics of each simulation are given in the relevant chapters once the problem is fully defined.

3.4 Penalty Function

It has been noted that any adaptive geometry which is to be operated for more than one cycle must operate only in the elastic region of the stress-strain curve. As with actuation location, the peak stress in the structure cannot be defined by a linear combination of the design variables and so must be included in the optimisation through another method. In this work, such constraints, which are only evaluated following the finite element calculation, have been achieved using a dynamic penalty function as described by Smith et al. (1997).

A penalty function $S_p(\mathbf{x})$ acts to increase the returned objective function value when the defined constraint has been breached. A static penalty function, such as that used by Rhodes (2012), adds an arbitrary constant to the true objective

$$S_p(\mathbf{x}) = S(\mathbf{x}) + \sum \delta_i c_i \tag{3.11}$$

where c is the penalty constant and $\delta = 1$ if a constraint is breached and 0 otherwise. The function therefore returns a value higher than the local region if outside the design constraints.

During the finite differencing step, the local gradient is therefore driven away from the illegal point and the optimisation continues. While this is effective in penalising infeasible points, a constant arbitrary value produces both a discontinuity in the objective space and a plateau of infeasible values. If the optimisation were to step into a location which is penalised in this way, there is then no gradient towards an acceptable location in the design space for the algorithm to use.

A dynamic penalty function replaces the constant value c_i with a function of the constraint

which has been breached. In the case of a yield stress constraint this is implemented as

$$S_p(\mathbf{x}) = S(\mathbf{x}) + \delta c \tag{3.12}$$

$$c = a\left(\frac{\sigma_{max}}{\sigma_{yield}} - 1\right)$$

$$\text{where:} \quad \delta \begin{cases} 0 & \sigma_{max} \leq \sigma_{yield} \\ 1 & \sigma_{max} > \sigma_{yield} \end{cases}$$

where a is a weighting constant. The inclusion of the breached constraint in the formulation of the penalty provides a gradient towards the optimal, legal, parameter set which may be followed by the algorithm. The parameter a allows the penalty magnitude to be scaled to an appropriate value for the current objective.

Once the modified objective function is evaluated, it is returned to the optimisation algorithm. A new point in the design space is selected and the process repeats. This continues until a local minimum is found and hence the set of optimal design parameters is identified. As with all computational simulations, a series of modelling assumptions are made that may influence the result. To quantify the true effect on the flow field, the initial and modified flow fields are also investigated experimentally. Details of the experimental process and equipment used follow in the next chapter.

Chapter 4

Experimental Methods

The data presented in this thesis were gathered using facilities in the Department of Aeronautics at Imperial College. Two different wind tunnels were used for experiments at different scales during this work. Equipment and techniques common to both experiments are described here while specific details of each experiment is given in the relevant chapters.

The control methodology for maintaining constant flow conditions within the wind tunnel is given initially in Sec. 4.1. In order to investigate the flow field, pressure and three-component velocity fields are obtained using pressure transducers and stereo particle image velocimetry. The details of the equipment and techniques used for each are given in Sections 4.2 and 4.4 respectively. Finally, in Section 4.6, details of the data reduction and analysis techniques used are described.

4.1 Wind Tunnel Control

The wind tunnel speed is closed-loop controlled using a PID controller operating within the National Instruments LabView 2013 system environment (National Instruments, 2013). The total and static tunnel pressures are monitored using a Furness FCO 310 micro-manometer and connected to the controller by RS232. The dynamic pressure, tunnel temperature and atmospheric pressure are recorded at 2.5 Hz throughout the experiment.

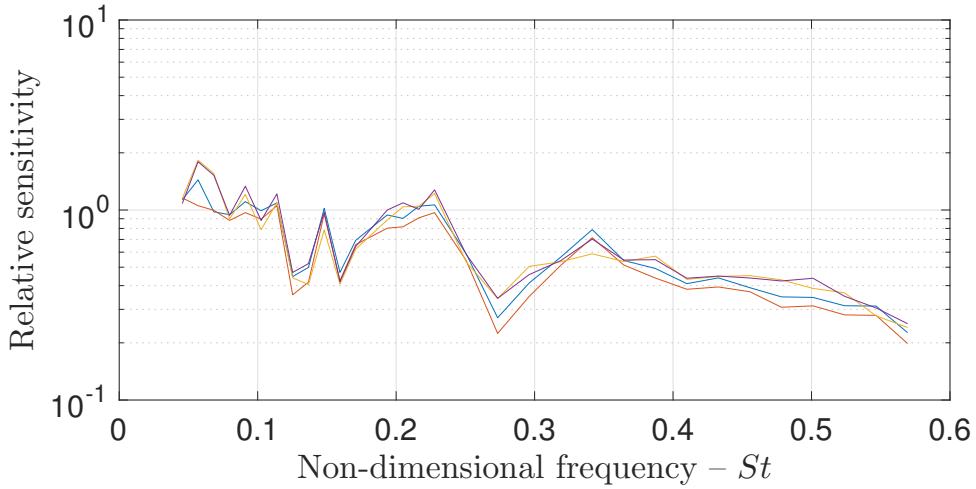


Figure 4.1: Frequency response of μDAQ compared to an Endevco high-frequency pressure probe

.

The controller was operated to maintain a constant Re. The current temperature and density are used with Sutherland's law to calculate kinematic viscosity ν. In both cases, data are only recorded once the recorded tunnel velocity is within 0.1% of the demanded value.

4.2 Surface Pressure Measurements

Surface pressure measurements are made using a number of Chell μDAQs. These transducers have a range of ±1 kPa and thermal compensation is applied internally. Each of the two transducers used have a maximum sampling rate of 20 kS/s multiplexed between channels. For the 32 channel transducers used in this work the maximum sampling rate is therefore 625 S/s/channel. This decreases to a maximum of ≈ 550 Hz when triggered externally. All pressures were therefore sampled at 500 Hz to avoid data loss.

The surface tappings are connected to the transducer by 0.97 m lengths of 0.5 mm diameter plastic tubing which runs through the model. The differential pressure for all tappings are connected to the static port on the tunnel Pitot-static probe. The total pressure is also connected to a measurement tapping for non-dimensionalisation.

The response of the μDAQ tappings to dynamic forcing is compared to that from an Endevco 8507C-1 piezoresistive pressure transducer located within the tapping array. A

speaker, driven with a generated sine signal, located 1 m from the aerofoil was used to excite all tappings at a range of frequencies and the response was compared to the Endevco probe. The relative sensitivity of the μDAQ compared to the signal from the Endevco for four tappings, used later in this work, are shown in Fig. 4.1. The pressure response is seen to be comparable between ports although varies across frequencies.

4.3 Oil Flow Visualisation

In order to gain a qualitative understanding of the pattern of near-wall streamlines, oil flow visualisation is used in Sec. 6.2.1. A mixture of paraffin, talc and hydraulic oil is applied to the experimental surface before staring the wind-tunnel. The wall shear stress acting on the model transports the mixture along the skin friction lines.

As the paraffin evaporates the talc is deposited on the surface. The hydraulic oil increases both the viscosity of the mixture and the working life, thus providing a qualitative description of the mean flow. In these experiments, the mixture is applied using an airbrush to achieve a thin uniform coating.

4.4 Particle Image Velocimetry

Stereo Particle Image Velocimetry sPIV is used to record the three component 3C flow field in this thesis. In the majority of vector fields presented in this work there is a significant through plane component. As any light sheet has a finite thickness, two component 2C PIV, which uses one camera, may incorrectly interpret this through plane movement as an in-plane translation and thus produce erroneous results. The use of sPIV, using two cameras offset from each other, allows the calculation of the third component of velocity, thus simultaneously providing more information about the velocity field and removing this source of error.

4.4.1 Hardware Setup

The wind tunnel is seeded with polyethylene glycol (PEG) mixed at a ratio of 1:4 with water. This mixture is atomised in a TSI 9307-6 seeder to form droplets with mean

diameter $d \approx 1$ μm (Tropea et al., 2007). The seed droplets are added to the closed-loop wind tunnel flow downstream of the working section. In order to obtain a suitable seeding density the tunnel is flooded with seeding before each run.

Illumination is provided by a dual cavity Litron LDY-304 pulsed YaG laser with wavelength 532 nm. Each cavity produces a 30 mW pulse at a repetition rate of up to 1 kHz. The beam path is manipulated using an array of coated mirrors before being formed into a light sheet using a cylindrical lens with focal length -74.4 mm.

The light sheet is directed at a 3D calibration target positioned in a known location and angle within the experiment. Alignment of the light sheet is confirmed by the illumination of four points offset to the target plane. Two targets of different sizes are used in this work, to account for different fields of view, and each has a positional tolerance of ± 20 μm. The light sheet is focused to the point immediately prior to the camera field of view to ensure a finite sheet thickness $t \approx 1$ mm across the recorded area.

The illuminated field is captured using two Phantom high speed cameras mounted on Scheimpflug mounts. Nikon 135 mm objective lenses are used. Two camera models are used in this work:

- For small fields of view 1 MPix Miro M310 are used with a maximum full resolution 12 bit frame rate of 3620 Hz.
- For large fields of view 4 MPix Phantom v641 are used with a maximum full resolution 12 bit frame rate of 1450 Hz.

The detail of the camera arrangement and location relative to the light sheet and field of view is experiment dependent and so are described in the relevant sections (5.4.4 and 6.1). The laser and cameras are synchronised using clock and trigger pulses produced by a LaVision HSC high speed timing box. The selection of the time period between frames is a balance between maintaining accurate correlation and obtaining a large enough displacement to reduce error in the velocity calculation. As a large through-plane component exists in most data, a time period of 7.5 μs was selected through experimentation as a suitable compromise.

The timing of these signals was confirmed using a digital oscilloscope and a typical trace of signals is shown in Fig. 4.2. The laser illumination was recorded using a Thor DET10A/M sensor positioned in an area of reflection from the tunnel wall. For a demand time period of 7.5 μs, the mean achieved value was 7.405 μs with a standard deviation of 549.9 ps

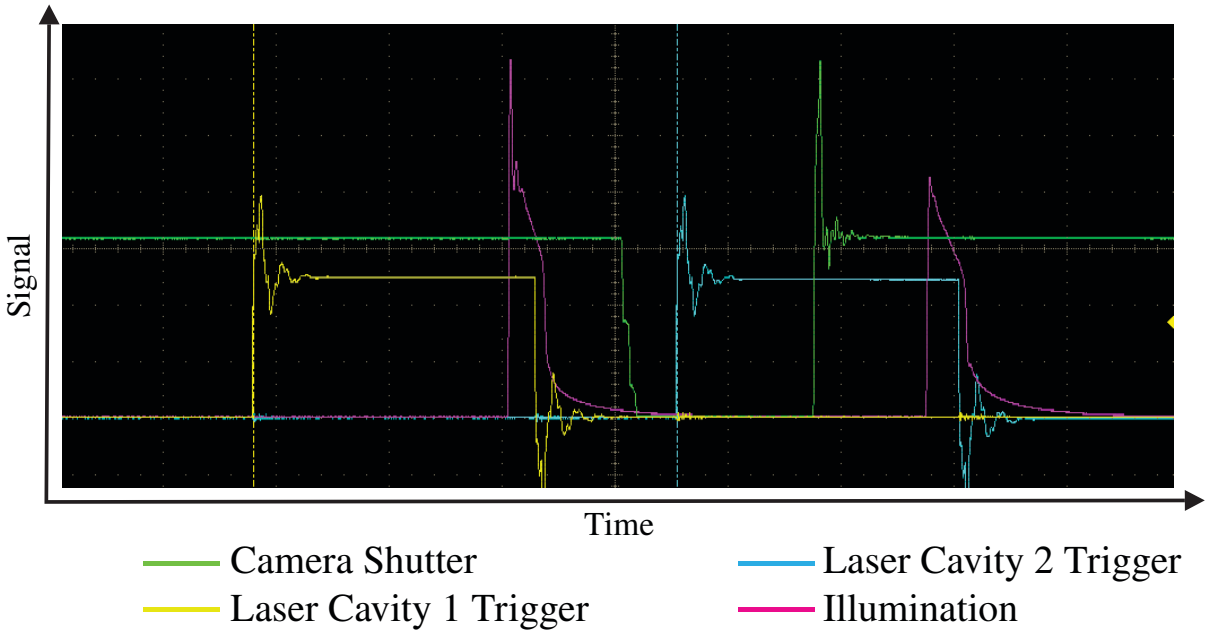


Figure 4.2: PIV Timing Trace from a Digital Oscilloscope

based on 1000 recorded samples. This calibration is subsequently applied to all velocity data presented during processing. Recording of a frame series is triggered by a signal from the Labview tunnel controller which ensures the operating conditions have been reached before data is recorded and then are sampled during the sequence.

4.4.2 Processing

The vector field reconstruction was performed using LaVision's DaVis 8.3.0 software (LaVision GmbH, 2015). For each dataset, the following procedure was followed:

1. Background subtraction – the minimum intensity from each pixel over the recorded set is found and subtracted from each frame. This is calculated independently for each camera.

2. Dewarping – all frames are transformed to 'real-world' coordinates using the calibration

3. 2D2C Correlation – Cross correlation is performed on each pair of frames from each camera to produce two separate two-component 2C vector fields.

4. 2D3C Correlation – The 2D3C vector fields are reconstructed from the two 2D2C fields.

5. Vector removal and replacement– Vectors are removed from the 2D3C field if the ratio of the correlation magnitude between the two most significant peaks $P_1/P_2 < 1.5$. The removed vectors are replaced using a 3×3 vector smoothing filter

Items 3 – 5 are repeated four times to iteratively improve the vector field. The first step uses a larger interrogation window to form an initial coarse field and the remaining steps use a smaller window to refine the solution. In all steps the field is calculated with a 75% overlap of a square, equally weighted, windows.

4.5 Adaptive Device Manufacturing

The VG developed or evaluated within this thesis are manufactured and measured using facilities at Imperial College London. Static devices are produced using a Connex 350 3D printer from a material compound of Vero and Tango proprietary materials. The printer resolution is $600 \times 600 \times 1600$ dpi in the x, y and z-axes respectively with a typical accuracy of < 85 μm.

The adaptive devices are manufactured from Stainless steel shim with thickness tolerance ± 4 μm. The structure is initially cut from the base material using an Oxford Lasers compact Micromachining system with beam width ≈ 6 μm. The material is restrained on a machined aluminium support using four rare earth magnets on the machine bed. This holds the material securely without warping or damaging the structure following cutting.

Each segment of the structure is cut in two steps, once with the beam path offset by half of the beam width to remove the inner material. A final path is cut to ablate the remaining material back to the desired structure. The cutting beam is manipulated using the integrated Galvo system with a traversing speed of 150 mm/s and repeated for 100 passes. Machine code detailing this process for each structure is produced using a MATLAB script from the design parameters. The cut structures are inspected for dimensional accuracy using a calibrated AxioVision measurement system and Zeiss Imager.M2M microscope.

To provide an impermeable skin to the cut structure it is cast in a 0.5 mm thick elastomer skin. The material used to provide this membrane is EcoFlex Silicone 00:50 rubber. This

material has a Young's modulus of $Y \approx 29.5$ kPa (Hollenstein, 2005) and a yield strain $\epsilon_{yield} > 1000\%$ and thus will not significantly alter the behaviour of the structure.

The upper surface of the translucent rubber skin is dusted with titanium dioxide to aid reflectivity before being measured with a Faro laser measurement arm. The arm is calibrated immediately before use and the standard deviation of the measurement error of a known surface was 2.5 μm. The model is clamped to the datum surface and a baseline measurement is taken. The surface is then measured at the actuated position and again once the surface was retracted to check for hysteresis in the lattice following actuation.

4.6 Data Analysis

Once data is acquired, either experimentally or numerically, additional analysis is conducted on it for comparison between cases or with previous studies. The principle techniques used in this work are: the use of non-dimensional parameters; transformation between the time and frequency domains; and the decomposition of vector fields into constituent modes for analysis. These techniques are described briefly below.

4.6.1 Non-dimensional Parameters

Reynolds Number

When investigating flows in which viscosity is significant, such as the separating flow over an aerofoil at high incidence, it is necessary to maintain similarity between experimental sessions. The Reynolds number Re is the ratio between inertial and viscous forces in the flow over a body and is given by

$$Re = \frac{U_\infty L}{\nu} \tag{4.1}$$

where U_∞ is the free-stream velocity, L is the characteristic length of the body, and ν is the fluid kinematic viscosity.

Pressure Coefficient

The surface pressures presented in this work are expressed as the difference between surface p and free-stream p_∞ pressures. This value is then normalised by the dynamic

pressure of the free-stream flow and is given by

$$C_p = \frac{p - p_\infty}{\frac{1}{2}\rho U_\infty^2} \tag{4.2}$$

where ρ is the measured fluid density. As C_p is independent of the free-stream fluid properties, results may be compared to other experiments with similar Reynolds number.

Strouhal Number

When studying fluctuating fluid flows around a body, a frequency f may be reduced to the non-dimensional Strouhal number

$$St = \frac{fD}{U_\infty} \tag{4.3}$$

where D is the characteristic body diameter. For the case of the flow over a cylinder, the canonical von Karmàn vortex street occurs at $St \approx 0.2$. When considering the flow over an aerofoil, the characteristic diameter can be found using

$$D = c \sin \alpha \tag{4.4}$$

where c is the aerofoil chord and α is the angle between the chord line and the free-stream flow (Roshko, 1954).

4.6.2 Power Spectral Density

In order to identify potential sources of oscillations in the measured flow quantities, it is useful to examine how the fluctuating energy is distributed in the frequency domain. In this work, the power spectrum analysis of a sampled data set is conducted using Welch's modified periodogram method (Welch, 1967). This method, when applied to long data sets, reduces the variance of the resulting power spectral analysis at the expense of a minimum resolved frequency.

The data series is split into a number of equal segments with 50% overlap. For each segment, a Hamming stencil is applied to the data and a periodogram is found using the finite Fourier transform. The mean of these windowed periodograms provides the averaged, modified, periodogram.

In this work, for ease of interpretation, these are presented as pre-multiplied spectra where the periodogram values are multiplied by the corresponding frequency and plotted on a graph with a log scale abscissa. The energy contained within spectral peaks can therefore be compared across the frequency range and peaks with equal area containing equal energy.

4.6.3 Proper Orthogonal Decomposition

The turbulent fluid flows which are recorded in this work represent instantaneous snapshots of a high order system, the dynamics of which are complex. Proper orthogonal decomposition (POD) has been shown to be useful in producing low-order approximations to the system dynamics (Berkooz et al., 1993). This method decomposes a series of data f into linear series of weighted orthogonal modes ϕ_m and associated coefficients c_m. The modes are ordered by their energy content and can be truncated to form a reduced-order model of the original data.

Each PIV field used in this work contains N data points and M temporal points. As $M < N$, the method of snapshots proposed by Sirovich (1987), and implemented in Gurka et al. (2006), is used. Initially, the data is collated into a single $N \times M$ matrix f with each row corresponding to a spatial point and each column corresponding to a snapshot. The symmetric correlation matrix R_{nm} is produced according to

$$R_{nm} = f^T f \tag{4.5}$$

the eigensolution of which yields eigenvectors ψ and corresponding eigenvalues λ such that

$$R_{nm}\psi = \lambda\psi. \tag{4.6}$$

The spatial POD modes can then be calculated by projection of these eigensolutions onto the original vectors

$$\phi_n = \sum_{m=1}^{M} \psi_n^m f_m \tag{4.7}$$

where ϕ_m is the mth POD mode and ψ_m^n is the nth element of ψ corresponding with the mth eigenvalue. The matrix of coefficients c is calculated by projecting the POD modes back onto the original data

$$c = \phi^T f \tag{4.8}$$

As this method of POD identifies spatially coherent structures, there is no requirement for temporal association between the snapshots. However, as the time step between slices is known, further analysis can be conducted on the variation in coefficient of each mode. If a PSD is conducted on the time series of modal coefficients, any characteristic frequency associated with the mode can be identified and hence related to other data.

Chapter 5

Adaptive Boundary Layer Control

The most frequently-used methods for controlling flow separation from an aerofoil were reviewed in Sec. 2.1.4. Of these, the most common is the passive vortex generator, which transports momentum from the freestream into the boundary layer, postponing separation. The efficacy of these devices is limited by the increase in parasitic drag produced at all conditions in the flight envelope. To overcome this limitation, this chapter describes the development of an adaptive structure which promotes the transfer of momentum but which can be retracted when not in use, reverting to an aerodynamically clean surface.

During the development of an adaptive 3D shock control bump, Rhodes (2012) described an optimisation methodology for the production of a general 3D morph. This is applied to an initially plane shell in Sec. 5.1. A significant limitation of this method is the development of geometry in which areas of high curvature are critical. The geometric function is therefore replaced with an aerodynamic objective in Sec. 5.2. The possible improvement in objective, before material yield, is limited by the production of in-plane strain within 3D morphs in regions of Gaussian curvature change. A high-strain, auxetic, lattice based structure is proposed to mitigate this penalty and applied to this problem in Sec. 5.4. Finally, the structure with optimised parameters is manufactured and the target deformation is validated in Sec. 5.5.

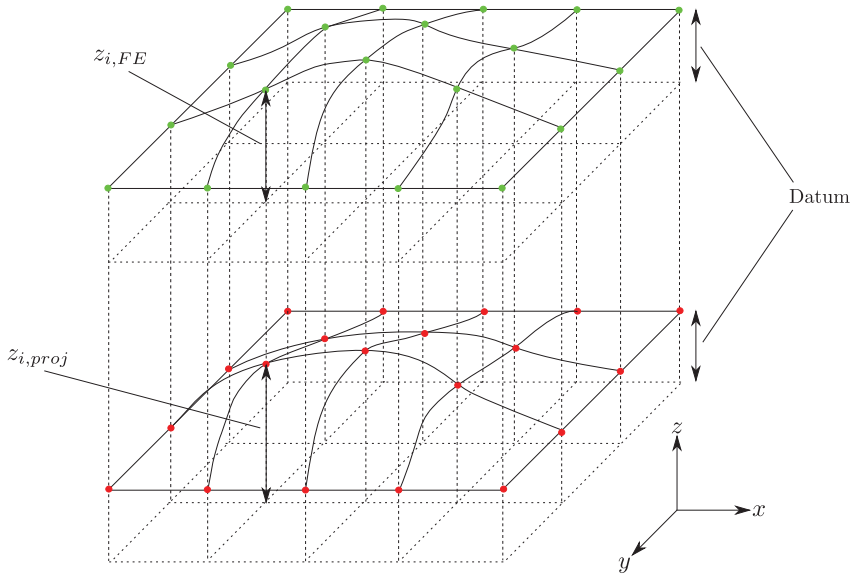


Figure 5.1: Comparison of morphed and target surfaces (Rhodes, 2012)

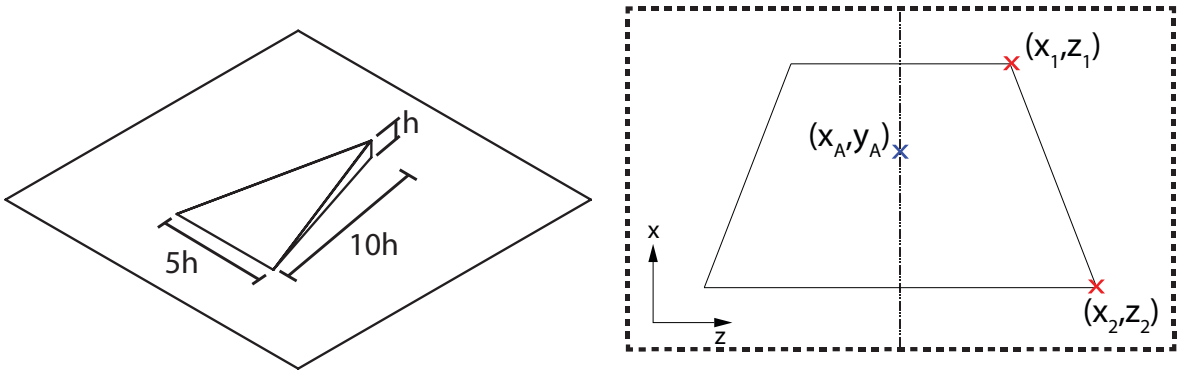
5.1 Geometric Objective Function

The use of a simple geometric objective function was described by Rhodes (2012) for the development of a 3D morph. In this method, a target geometry is selected from existing literature and a grid of n discrete comparison points are used to represent the target surface in Cartesian co-ordinates $z_t(x, y)$. Once the morphed geometry has been calculated, the achieved deformation $z_m(x, y)$ is compared at these co-ordinates and a scalar quantification k_z of the approximation quality is found by taking the root-mean-square of the area-weighted pointwise positional error

$$k_z = \sqrt{\frac{\sum_{i=1}^{n} \left(\frac{z_{t_i} - z_{m_i}}{A_i} \right)^2}{n}} \tag{5.1}$$

where z_{t_i} and z_{m_i} are the target and achieved surface height above a common datum, A_i is the area associated with each point, and n is the number of points.

When selecting a target geometry, it is necessary to consider the physical constraints which limit the possible shapes which may be produced by an adaptive surface. The principle restriction on the final geometry is that, in order for the system to be reusable, the deformation must be elastic. The peak stress produced in the surface is therefore limited by the material yield stress. For a simple shell under pure bending, using the Kirchoff-Love hypothesis, the resulting moment within the surface is found with equation



(a) (b)

Figure 5.2: (a) Target geometry and (b) optimisation domain

$$\begin{bmatrix} M_x \\ M_y \\ M_{xy} \end{bmatrix} = \frac{2t^3 E}{3(1-\nu^2)} \begin{bmatrix} 1 & \nu & 0 \\ \nu & 1 & 0 \\ 0 & 0 & 1 \end{bmatrix} \begin{bmatrix} \kappa_x \\ \kappa_y \\ \kappa_{xy} \end{bmatrix} \tag{5.2}$$

where all variables are as previously defined. It therefore follows that for any variation in geometry to be elastic, the induced bending moment must be finite. This in turn requires the curvatures to be finite and thus the surface to be C^1 continuous.

Of the existing vortex generators reviewed in Sec. 2.1.4, the most common is an arrangement of vanes protruding perpendicularly from the wing surface at an angle to the streamwise flow and terminating sharply. Whilst this produces a very efficient mixing mechanism, these vanes are typically only the thickness of the base material. The plan area which they occupy, and hence from which a morphing version must be developed, is very small. Since there is no bulk displacement of the boundary, the positional error produced by the curvature of a continuous surface prevents the shape being reproduced with significant fidelity, making this geometry unsuitable for use as a morphing target.

Any geometry to be used as the target shape which is to be approximated by deforming a continuous surface must: have a finite projected area on the source surface, so that the additional positional error produced by the addition of curvature is limited; and be effective in its native form. For this work, a forwards wedge VG with height 2 mm, the baseline fluid boundary layer thickness, such as that shown in Fig. 5.2(a) meets both of these requirements.

The optimisation process described above was applied to a symmetric surface with layout as shown in Fig 5.2(b). The material used in this work is Stainless Steel 1.4310. This is selected as, being a material used for shim stock, it is available at the required thickness at high accuracy. The parameters used in this design optimisation, and the upper and lower bounds for the variables manipulated by the optimisation algorithm, are given in Tab. 5.1.

Description	Symbol	Lower Bound	Upper Bound	Initial Condition
Boundary Vertex (mm)	x_1	72.5	106.0	80.0
Boundary Vertex (mm)	z_1	10.0	50.0	30.0
Boundary Vertex (mm)	x_2	19.0	52.5	40.0
Boundary Vertex (mm)	z_2	10.0	50.0	35.0
Actuation Location Parameter	P_A	0.1	0.9	0.5
Actuation Height (mm)	y_A	0	10.0	1.0
Yield Stress (GPa)	σ_{yield}	—	1.0	–

Table 5.1: Optimisation design variables $\mathbf{x}$ and their constraints $\mathbf{x_{LB}}$ and $\mathbf{x_{UB}}$

5.1.1 Shell Simulation Setup

The domain to be considered is discretised into an array of equally spaced quadrilaterals. These are represented structurally as finite-strain Mindlin-based shell elements. Each node has 6 degrees of freedom and the numerical quantities are interpolated linearly between points. These quantities are calculated at four integration locations across each cell at 5 through-cell locations. This is implemented in Abaqus as element type *S4*.

The actuation is applied to the plate by the displacement into the plate's surface of an analytical cylinder with diameter $d = 2 \times 10^{-3}$ m. Deformation of the simulated domain is produced by a frictionless contact interaction between the two bodies. This method of deformation allows the actuation to occur at any point on the surface without altering the cell topology. The contact also distributes the displacement actuation across a finite area as opposed to an infinitesimal point which can produce non-physical strains around the actuation.

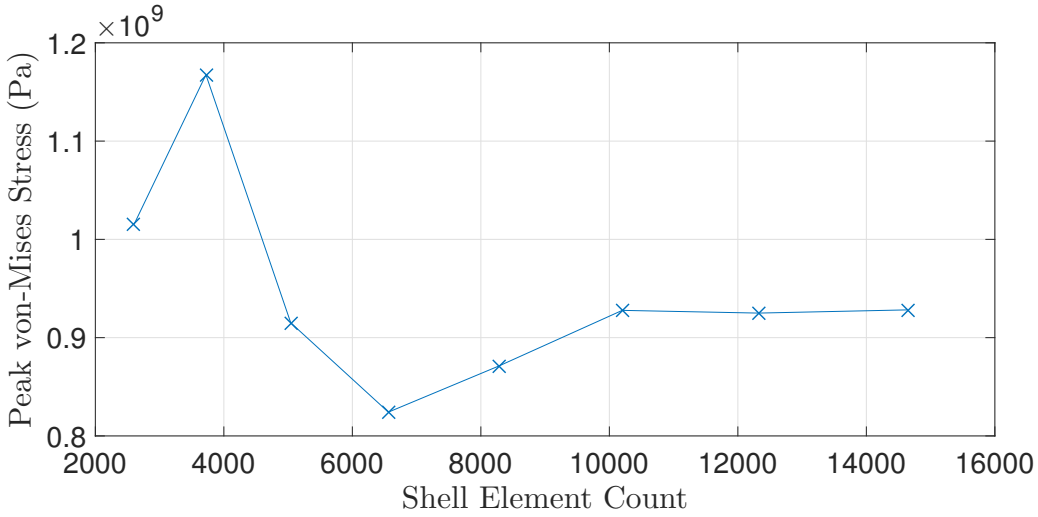


Figure 5.3: Grid convergence results, variation of peak stress with cell count

The domain is constrained around the periphery in all degrees of freedom, maintaining continuity in both position and surface gradient with the original surface. This is necessary to produce the final desired design from a continuous, aerodynamically clean, skin. A grid convergence study was conducted to determine the number of elements required to obtain an accurate solution. The maximum domain extent considered was selected as a 'worst case' scenario and a displacement of 1 mm was applied to the centre of the plate. The resulting stress and displacement of the surface mid-planes is shown in Fig. 5.3. The asymptotic behaviour of the results is visible from a cell count of greater than 1×10^4 and the element count is therefore fixed at 101×101.

5.1.2 Geometric Optimisation

The optimisation algorithm was run until convergence behaviour is shown in Fig. 5.4. Also shown in this plot is the peak von Mises stress within the surface. As the objective function decreases, a decrease is also seen in the peak stress in the surface. Following the work of Rhodes (2012) who concluded that in plane stress was a key limiting factor in such morphs, this appears anomalous and so is now discussed further.

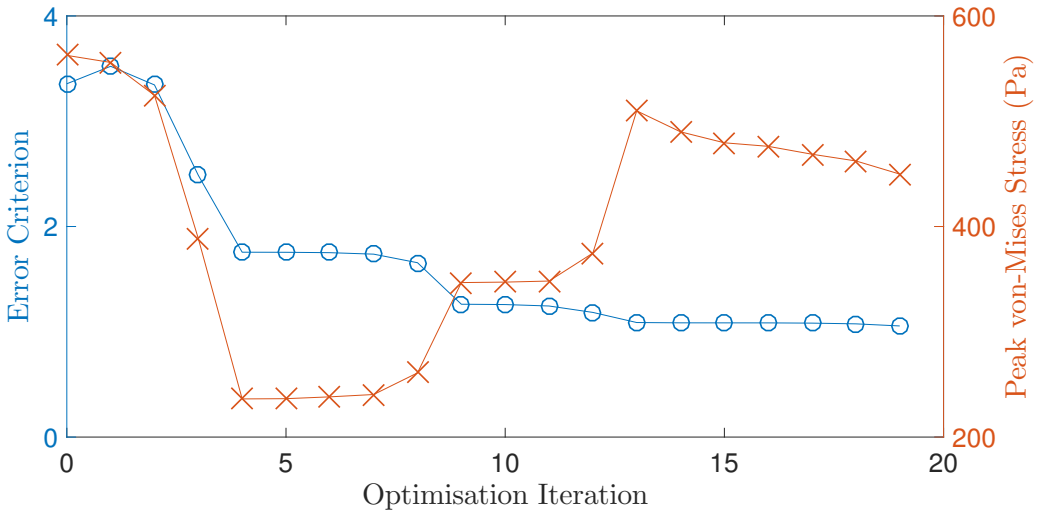
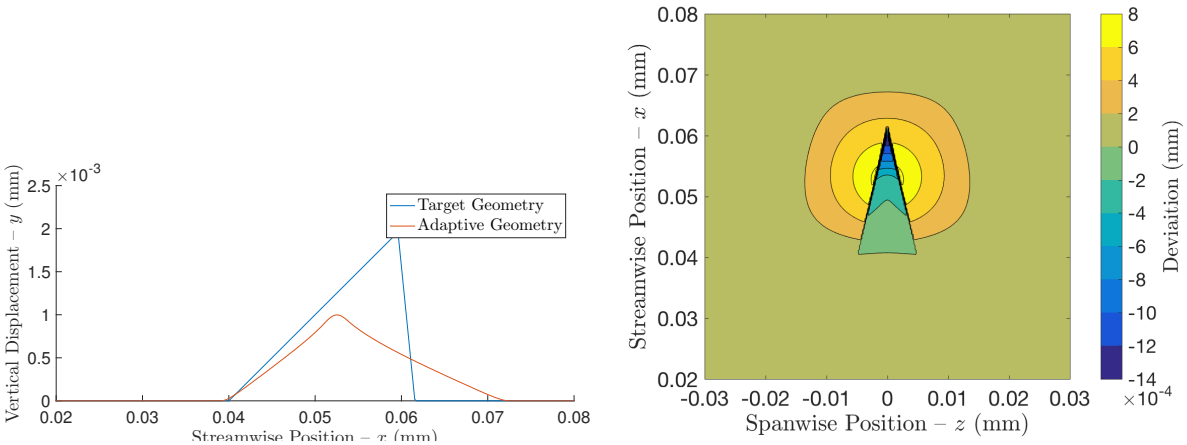


Figure 5.4: Geometric convergence and peak von Mises stress

Description	Symbol	Final Value
Boundary Vertex (mm)	x_1	0.0725
Boundary Vertex (mm)	z_1	0.015
Boundary Vertex (mm)	x_2	0.039
Boundary Vertex (mm)	z_2	0.022
Actuation Location Parameter	P_A	0.40
Actuation Height (mm)	y_A	1.0
Yield Stress (GPa)	σ_{yield}	0.4500

Table 5.2: Optimal design parameters for minimising RMS positional error using an actuated uniform plate

Figure 5.5(a) shows a centreline section of the resulting deformed surface in comparison to both the initial and target geometry. While the final geometry appears to superficially represent the target, the actuation magnitude can be seen to have reduced significantly from the original height. As described above, this is not due to the yield stress penalty function but is instead due to the inability of the surface to accurately represent the steep gradients present in the target geometry. This is confirmed in the distribution of positional error magnitude across the surface which is shown in Fig. 5.5(b).



(a) Plate centerline

(b) Plate displacment error distribution

Figure 5.5: Optimal geometry for minimising RMS positional error using an actuated uniform plate

5.1.3 Influence on a Simulated Boundary Layer

In order to quantify the effect of this geometry on a boundary layer, the deformed geometry was inserted into a CFD simulation as described in Sec. 3.3. The fluid domain in this work represents turbulent flow over a plate and is described by the boundaries

$$\begin{aligned} 0 \leq x \leq 0.22 \ \text{mm} \qquad & \text{(streamwise)} \\ 0 \leq y \leq 0.025 \ \text{mm} \qquad & \text{(surface normal)} \\ -0.05 \leq z \leq 0.05 \ \text{mm} \qquad & \text{(spanwise)} \end{aligned}$$

A multi-block structured mesh was produced for the baseline case. As CFD simulations have been shown to be heavily mesh dependent, the use of a common, structured, grid topology allows for more comparable results than unstructured meshes as well as providing an increase in convergence rate Blazek (2005). The streamwise and spanwise grid spacings are specified in terms of non-dimensional wall units $\Delta x_+ \approx 100$ and $\Delta z_+ \approx 35$ where

$$\Delta x_+ = \frac{x}{\nu}\sqrt{\frac{\tau_w}{\rho}} \tag{5.3}$$

in line with common empirical requirements (Tucker, 2014).

The mesh therefore has $220 \times 34 \times 280$ (x, y, z) grid points with the nodes in x and z spaced evenly across the domain. The first y coordinate for each point in the $x-z$ grid is

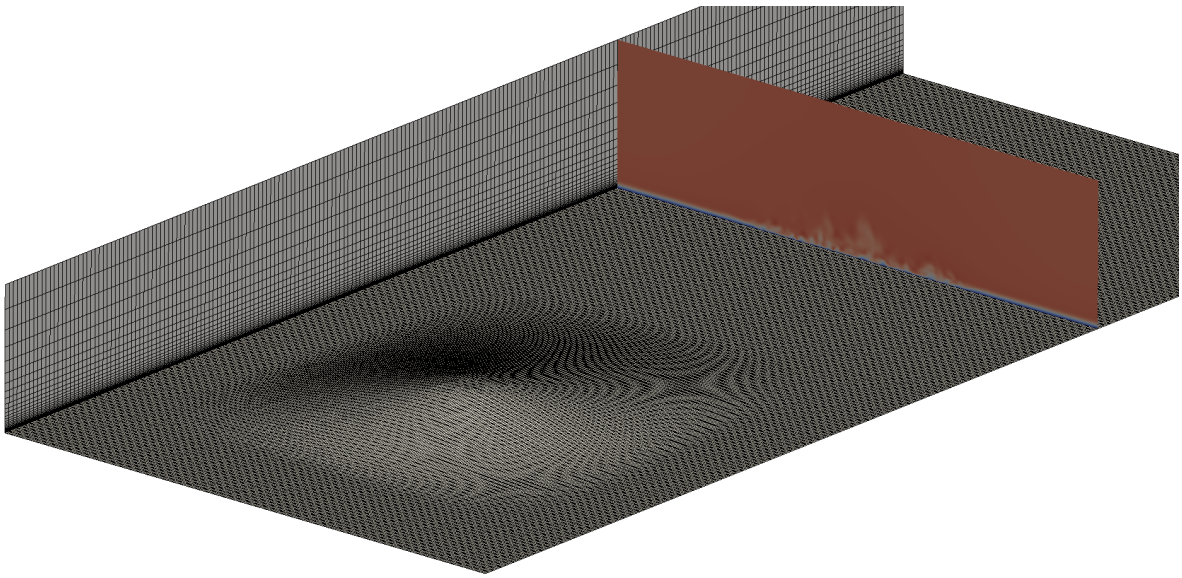


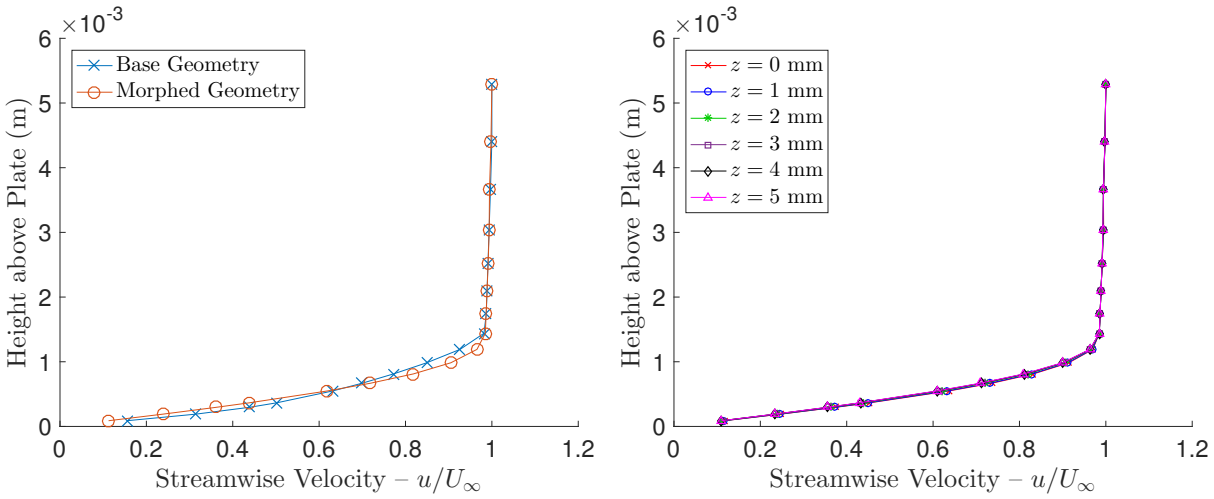
Figure 5.6: Plate CFD Mesh

located according to the interpolation above and a constant expansion ratio is applied to the y coordinates. The first wall-normal grid point is located with non-dimensional wall distance $y_{+1} \leq 1$ across the domain ensuring sufficient resolution to capture the boundary layer.

In the morphed case, the vertices on the boundary representing the adaptive geometry are translated to provide the required deformed surface geometry. The displacement was then propagated throughout the mesh while maintaining a uniform cell growth rate from the wall along each meshline.

The model was run until convergence and the resulting boundary layer profiles are plotted in Fig. 5.7. There is little difference in the velocity profiles following actuation, however the near-wall velocity, critical for separation resistance, is seen to decrease indicating a momentum loss.

In order to understand this result, it is necessary to again consider the mechanism behind the effectiveness of vortex generators. As described previously, the presence of a geometry modification changes the path of the fluid streamlines passing over it and so alters the spanwise pressure distribution. The existence of pressure gradients causes a spanwise velocity, and so streamwise vorticity at the fluid boundary. Towards the trailing edge of the VG, the boundary layer separates, shedding this vorticity into the flow where it causes mixing and so causes a transfer of momentum through the boundary layer. In this case,



(a) Mean velocity profiles

(b) Velocity profiles at different spanwise locations downstream of the morphed geometry

Figure 5.7: Boundary-layer profiles downstream of deformed geometry

while the modified geometry does deform causing a change in pressure, the downstream curvature of the morph does not represent that of the target. The streamwise adverse pressure gradient on the downstream side of the morph is therefore not sufficient to cause local separation and so the near wall vorticity instead dissipates in the near wall region. The additional gradients also instead caused increased viscous loss and a decrease in overall momentum.

The resulting problem, acting on viscous forces within a fluid flow, is nonlinear with respect to geometry position and highly sensitive to curvature distribution. For a geometric objective to be effective, a combination of higher order terms must be included. This then becomes a multi-objective problem and the relative weights of each term are unknown *a priori*. Instead, a different approach is needed for the quantification of device efficacy during the optimisation.

5.2 Aerodynamic Objective

The previous section has shown that it is necessary to consider the nonlinear effect of the adaptive geometry on the boundary layer during the optimisation process. The most complete measurement of this effect would be to experimentally test each resulting geometry experimentally. However, the experimental time to complete this is prohibitive

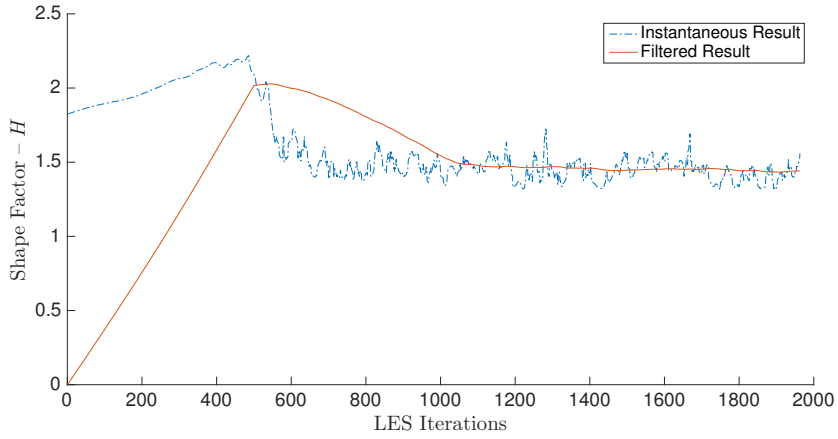
and due to the finite differencing method used during the optimisation, in order to find the local gradient, any experimental error would significantly affect the results and hence cause the algorithm to incorrectly traverse the design space.

As an alternative to experimentation, the LES above is used to calculate the downstream effect of the adaptive section on the fluid. To quantify the level of boundary-layer momentum transfer caused by each surface, a suitable fluid metric must be selected to transform the 3D velocity data into a scalar value. In quantifying the efficacy of isolated traditional vortex generators, previous authors have used a multitude of independent flow characteristics such as vorticity, vortex path and longevity. While these methods are useful in describing the precise fluid behaviour, the results cannot be easily reduced to a scalar quantity which may be used during the optimisation. Instead, the boundary layer shape factor H as defined in Eq. 2.5 will be used to quantify the distribution of momentum within the boundary layer.

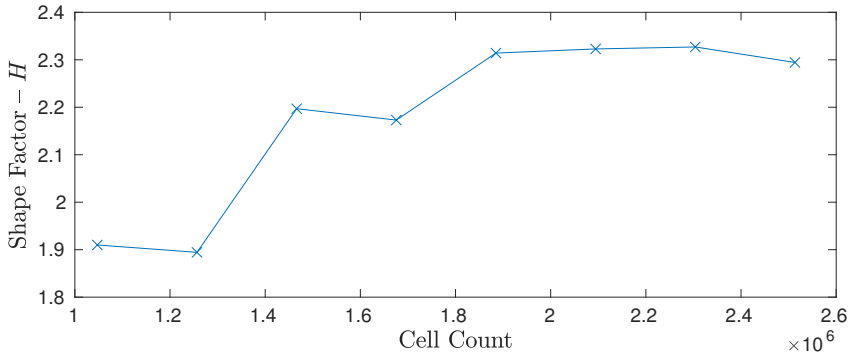
A high value of H corresponds to a flow such as that found in an adverse pressure gradient (Schlichting and Gersten, 2000) with little momentum near the wall. Conversely, a low value represents a highly turbulent flow which is resistant to separation and therefore provides the basis for a suitable objective function to be minimised by the optimisation algorithm. LES provides a time-resolved solution and so contains both temporal and positional variation. H is therefore calculated as the mean from 11 uniformally distributed spanwise positions in the range $-5 \leq z \leq 5$ mm at the same streamwise position as in the previous study $x = 150$ mm. The simulation was judged to be converged when the asymptotic behaviour of the rolling mean of 500 time iterations was observed as shown in Fig. 5.8(a).

In order to confirm the simulation contained sufficient resolution, a grid convergence study was conducted. A representative surface, based on the use of the full morphing domain and with a 2 mm actuation applied at the centre of the plate, was used to provide the geometry variation in the plate surface. The results of this study are shown in Fig. 5.8(b). Convergent behaviour is observed for grids with element counts above $\approx 2 \times 10^6$ cells over this domain. This is in line with the empirical results of Tucker (2014) described previously, corresponding to 2.09×10^6 elements, and so these values are used in all future simulations.

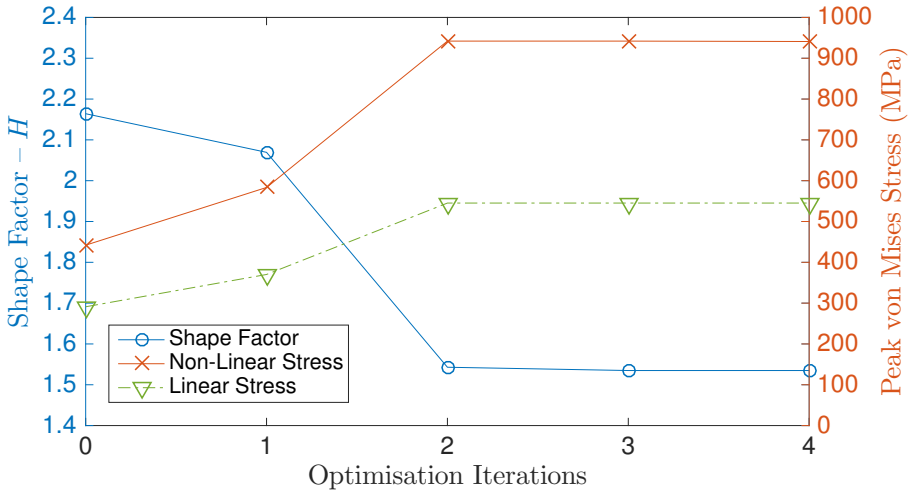
The optimisation process was repeated with the aerodynamic objective and using the same design variables, boundary conditions and initial values as before. The optimisation



(a) Convergence of LES objective function



(b) Grid convergence of LES simulations



(c) Plot of optimisation function convergence (○) and corrosponding peak von Mises stress for nonlinear (×) and linear (▽) cases

Figure 5.8: Convergence plots of the objective function for (a) each subiteration call; (b) CFD grid; and (c) optimisation iterations

Description	Symbol	Final Value
Boundary Vertex (mm)	x_1	69.93
Boundary Vertex (mm)	z_1	29.95
Boundary Vertex (mm)	x_2	0.20
Boundary Vertex (mm)	z_2	34.97
Actuation Location Parameter	P_A	0.50
Actuation Height (mm)	y_A	2.80
Peak Stress (GPa)	σ_{max}	0.942

Table 5.3: Optimal design parameters for minimising H using an actuated uniform plate

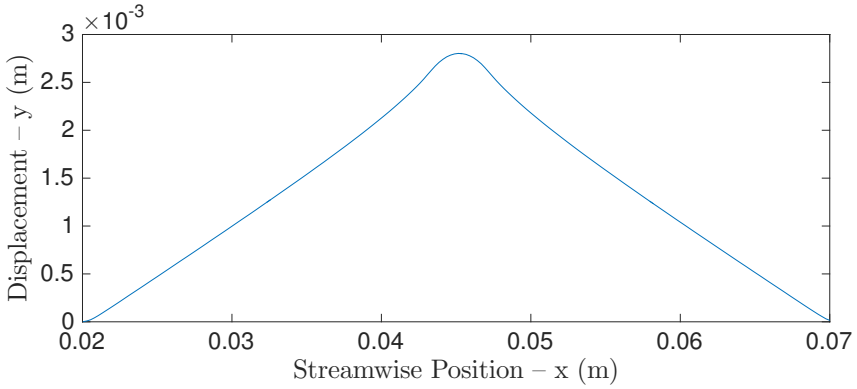
	Shape Factor H
Base Condition	1.81
Discrete VG	1.31
Adaptive Surface	1.54

Table 5.4: Comparison of boundary layer shape factors

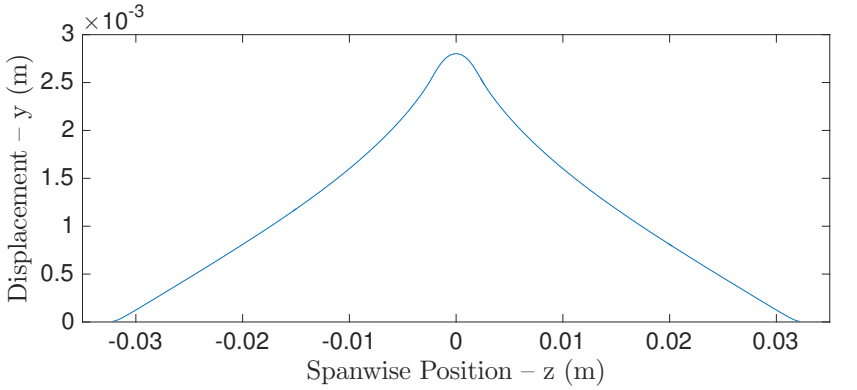
ran for four iterations at which point no further improvement was possible. The values of shape factor and peak stress are plotted in Fig. 5.8. The initial design parameters used to start the optimisation produce a shape factor of $H = 2.16$. A rapid improvement in H is observed over the first two iterations after which no further improvement is seen. Over the same period, a rapid increase in peak von Mises stress is present, which approaches the yield criterion.

Streamwise and spanwise sections of deformed geometry through the actuation point are shown in Fig. 5.9. Unlike the case with the geometric objective, the peak deformation is seen to increase from the initial conditions. The effect on the computed downstream boundary layer profiles are shown in Fig. 5.10. The computed velocity profile following the original target forward wedge VG is also shown for comparison and shape factors for both geometries are shown in Tab. 5.4

The shape factor following the adaptive structure reduces significantly, indicating a transfer of momentum towards the wall from the freestream. This is observed in the boundary-layer velocity profiles by an increase in near wall velocity for $y < 2$ mm. Further from the wall a large, developed, wake is visible indicating significant mixing and subsequent increased boundary layer thickness. In comparison, the static VG produces a similar level of near wall velocity increase but with a distinct wake, away from the wall and apart from

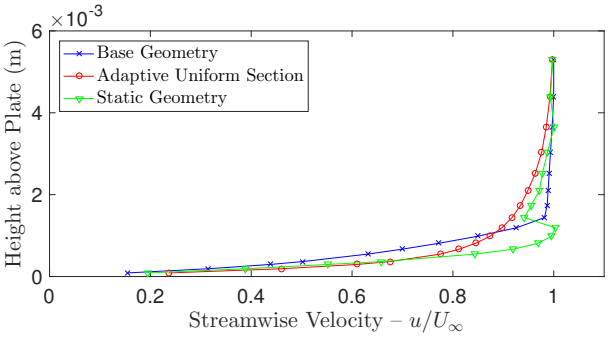


(a) X-Y section at $z = 0$ m (mid-plane)

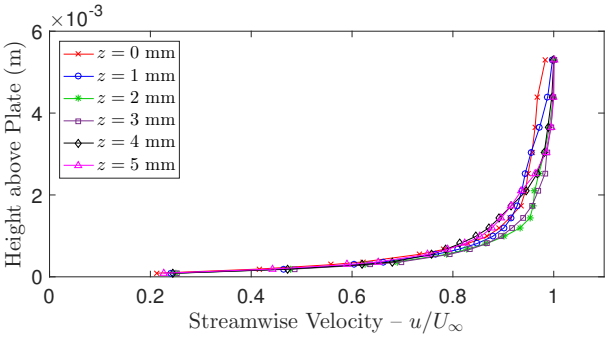


(b) Z-Y section at $x = 0.045$ m (peak deformation)

Figure 5.9: Deformed geometry resulting from the converged optimisation function using a shell section



(a) Mean velocity profiles



(b) Velocity profiles from different spanwise locations behind adaptive gemetry

Figure 5.10: Mean boundary layer profiles for the 'clean' condition (×), the optimised deformation (○), and a fixed static vortex generator (▽).

the boundary layer. This is represented by a further improvement in shape factor and lower overall momentum deficit.

Plotted alongside the peak nonlinear stress in Fig. 5.8(c) is the equivalent linear stress, obtained considering only bending loads. While an increase in stress due to bending is observed, as actuation height increases, the final linear stress levels form approximately 60% of the total levels. This demonstrates that, while the bending stress levels are significant, if the induced membrane stresses can be reduced then a further improvement in H may be possible.

5.3 Influence of Gaussian Curvature on Morphing Structures

In the profile morphing applications reviewed in Sec. 2.2, the principle method of producing the required geometry change is a small change in surface curvature $\kappa_{(x,y)}$ and so an increase in bending stress σ_B across the section. If the desired alteration in geometry is unachievable through curvature change alone, then the elongation or contraction of the surface is necessary but is associated with a linear change in mid-plane membrane stress σ_M. Under these conditions, the distribution of curvature change and material elongation, and therefore the geometry of the deformed surface, is difficult to solve and frequently simplified by assuming geometric linearity. The bending and elongation may then be solved separately and the stress distribution obtained by the superposition of bending and membrane stresses

$$\text{Peak stress:} \quad \sigma_x = \sigma_{B_x} + \sigma_{M_x} \tag{5.4a}$$

$$\text{Bending stress:} \quad \sigma_{B_x} = \frac{Et}{2\left(1-\nu^2\right)}\left(\partial\kappa_x + \nu\partial\kappa_z\right) \tag{5.4b}$$

$$\text{Membrane stress:} \quad \sigma_{M_x} = \frac{E}{\left(1-\nu^2\right)}\left(\epsilon_x + \nu\epsilon_z\right) \tag{5.4c}$$

This approach loses accuracy for cases with high in-plane loading. However it remains suitable for a qualitative investigation of the required magnitude of each component.

The curvature at a point of any surface may be described by two principle curvatures κ_1, κ_2 which are the maximum and minimum curvatures respectively. The product of these values forms the Gaussian curvature κ

$$\kappa = \kappa_1\kappa_2 \tag{5.5}$$

which provides detail to the local topology of the surface. For values of $\kappa > 0$, the sign of both principle curvatures is the same and so describes a bowl shaped surface. $\kappa < 0$ requires curvatures of opposite sign and so describes a saddle. For flat or prismatic surfaces, such as a 2D aerofoil section (Fig. 5.11(a)), where either one or both principle curvatures are zero, $\kappa = 0$. Such surfaces with $\kappa = 0$ are termed 'developable' surfaces as they can be formed from a flat sheet through bending alone. To form any other shape it is necessary for regions of the material to extend or contract locally.

A relationship between local material strain and change in Gaussian curvature was described by Calladine (1983) as

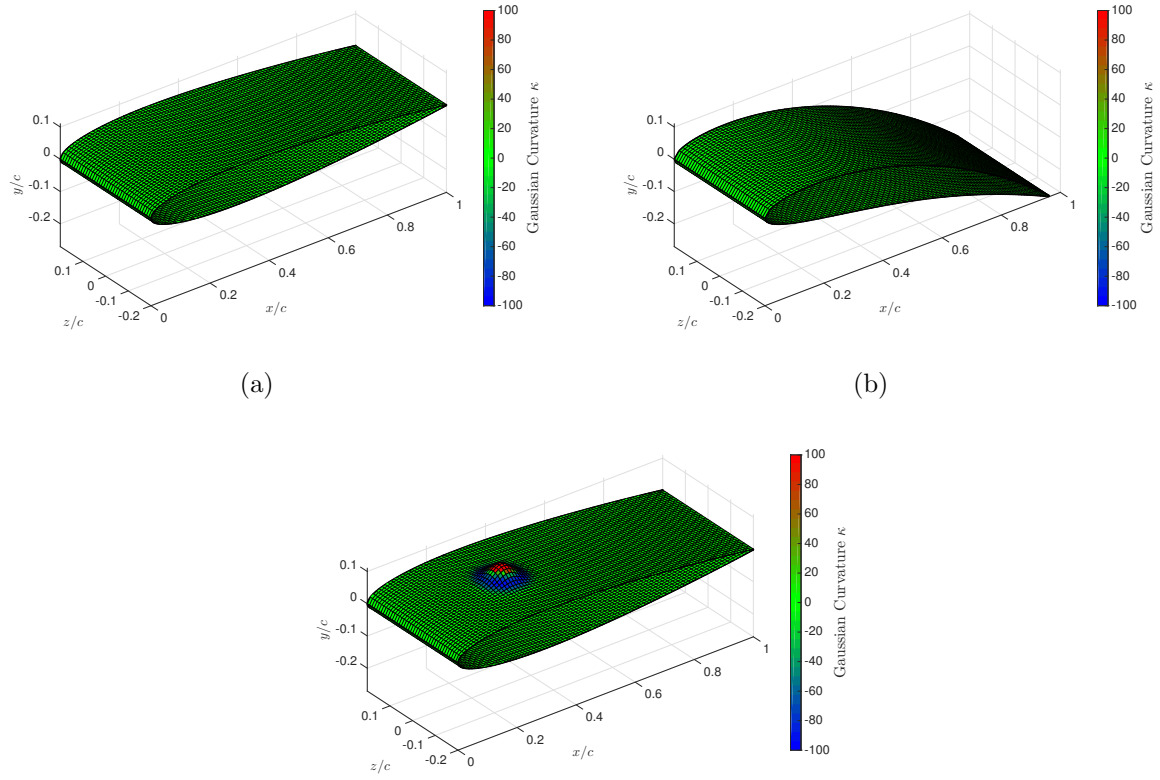
$$\Delta\kappa = -\frac{\partial^2 \epsilon_z}{\partial x^2} + \frac{\partial^2 \gamma_{xz}}{\partial x \partial z} - \frac{\partial^2 \epsilon_x}{\partial z^2} \tag{5.6}$$

where γ is the twist in the surface and all other terms are as previously defined. This is the basis from which most profile morphing proposals are derived. When the morph is actuated, the distribution of streamwise curvature varies across the chord providing the required geometry change. However, throughout the actuation the spanwise curvature remains at or near zero (Fig. 5.11(b)). The membrane strain in a skin induced during such '2.5D' morphs by a change in Gaussian curvature is negligible and so the morph is achievable through bending alone. For this work the aim is to produce a localised near-wall mixing effect and, as reviewed in Sec. 2.1.4, this therefore requires a spanwise variation in the fluid boundary. An exaggerated example of such a morph is shown in Fig. 5.11(c). Since the section in the actuated case is no longer prismatic, regions of non-zero Gaussian curvature exist on the surface. The through-morph $\Delta\kappa$ is therefore also non-zero and thus is accompanied by in-plane membrane strain.

The strain levels imposed are directly related to the severity of the morph required and in addition to those due to the bending of the material. A typical aerospace material, Aluminium 7075-T6, has a yield strain of 0.65%. This will severely limit the magnitude of any 3D morph and so any steps which may be taken to mitigate this are therefore desirable.

5.4 Lattice Structure

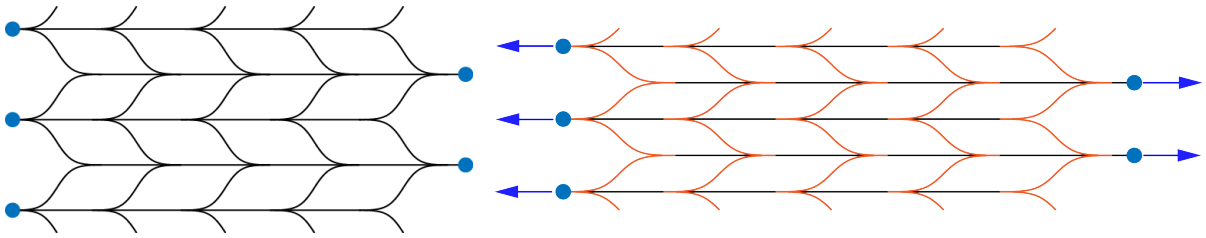
In Sec. 2.2.2 the use of specialist skins for aerofoil profile morphs was reviewed. In these examples, a global change in one or two dimensions was desired without compromising



(a) (b)

(c)

Figure 5.11: Gaussian curvature distributions on three wing segments: (a) unmodified geometry; (b) the same section following a camber variation (zero Gaussian curvature); and (c) the original section with a local, out-of-plane, geometry change (non-zero Gaussian curvature)



(a) Before deformation (b) After deformation

Figure 5.12: Example of a bending-dominated lattice under in-plane normal loading.

stiffness in the third. One of these techniques, replacing the skin with a 2D lattice structure, allows the tailoring of material properties by design to the required actuation.

Two-dimensional lattices are produced by tessellating a unit cell of interconnected beams across a domain. When the surface is loaded the constituent beams deform through either bending or stretching. A method of determining which of these is the principle deformation type was developed by Deshpande et al. (2001). In this method the rigid joints of the lattice are replaced with pin-joints and the resulting structure is checked for determinancy. If the pinned lattice is kinematically determinate then the structure is stretching dominated. These are stiff lattices which are frequently used for weight saving (Vasiliev et al., 2001).

If the pinned lattice is kinematically indeterminate however, the rigid lattice is bending dominated. When placed under load, the pin-jointed mechanisms causing the indeterminacy in the pinned lattice allow regions to rotate without material elongation. While the rigid lattice is by definition kinematically determinate and the beams unable to rotate at the joints however, Gibson and Ashby (1999) showed that, if the beams are slender, the local bending of the rigid lattice results in a similar global deformation. In addition, from Eq. 5.4b, since stress is related to $t \ll \ell$, a high level of bending is achievable before yield.

Fig. 5.12 shows an example of a bending dominated lattice. In a continuum, the in-plane loading shown would typically result in the production of membrane strain, severely limiting the achievable, elastic, displacement. Instead, in the lattice, a bending moment is produced in the highlighted elements, causing them to rotate from their original position. As the compliance is distributed throughout the surface this flexibility is available for extensions in both directions, unlike some of the skins reviewed earlier.

5.4.1 Unit Cell Topology

A large variety of tesselatable unit cells have been developed with a wide range of bulk material properties. Olympio and Gandhi (2007) and Bubert et al. (2010) used a lattice to provide a high strain skin for profile morphing applications. In addition to allowing a significantly larger elastic extension than would be possible with traditional materials, the particular lattice topology with a bulk Poisson's ratio $\nu = 0$ also removes the detrimental spanwise loading due to Poisson's effects.

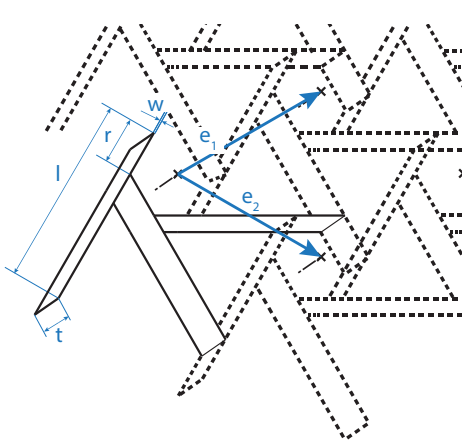
For the device to be developed in this work, the elongation and curvature of the surface must occur in both directions when actuated. Referring again to Eqs. 5.4, the use of a structure with $\nu < 0$ will reduce the detrimental internal loading due to Poisson's effects. When combined with the increase in membrane yield strain of a bending dominated lattice and the decoupling of bending and membrane stiffnesses, this will significantly increase the range of elastically achievable geometries.

The topology selected to implement this combination of properties is the Hex-Chiral lattice proposed by Prall and Lakes (1997). This design has a theoretical bulk Poisson's ratio $\nu = -1$. The lattice is defined by the length of the spars l, the hub radius ratio r/l, the beam width w and the material thickness t. These parameters are shown graphically in Fig. 5.13(a). The adjustment of these parameters allows the tailoring of the surface properties as required.

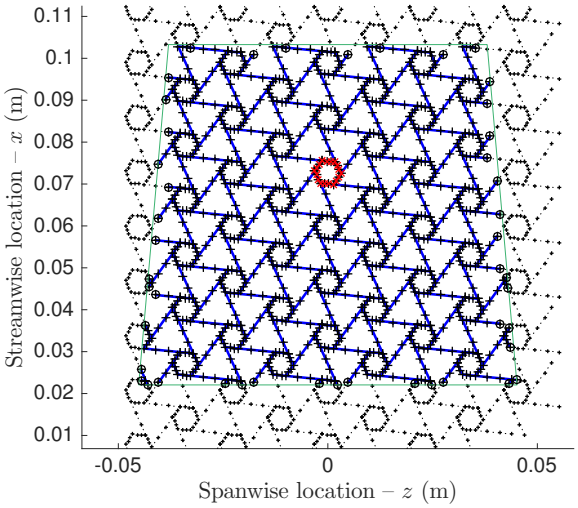
5.4.2 Beam Element Simulation

In order to evaluate the deformation field which results from a lattice based surface, a number of Timeshenko beam elements are used to produce the characteristic unit cell (Fig. 5.13(a)). As with the beam elements previously described, each node has six degrees of freedom and numerical quantities are interpolated linearly between points. These elements are implemented within Abaqus as type *B31*. A grid convergence study was conducted on the number of elements per bar of the unit cell based on the maximum possible domain size. The convergence of discritisation level to peak stress are shown in Fig. 5.14.

In order to populate the adaptive domain with the lattice, a seed unit-cell is located with the hexagonal cell hub centred over the desired actuation position. Since a lattice



(a) Parameters of the hex-chiral lattice



(b) Chiral lattice topology

Figure 5.13: (a) the unit-cell parameters which define the lattice, and (b) 2D lattice simulation with hex-chiral geometry.

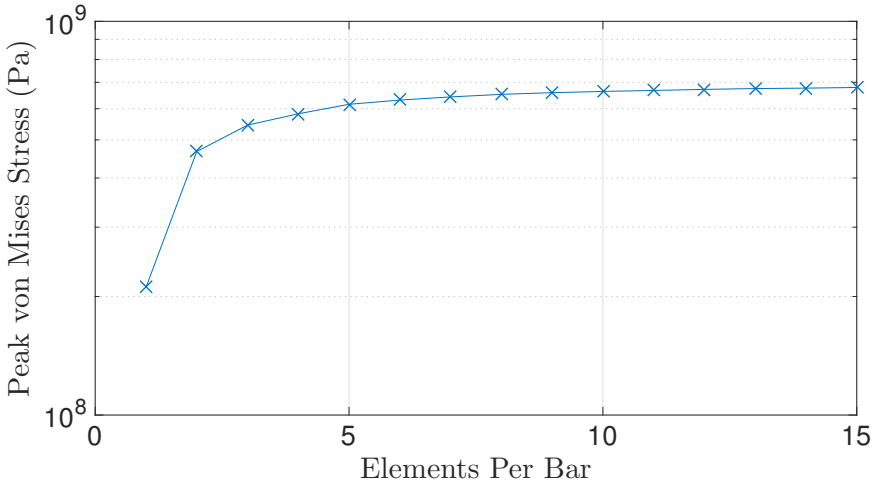


Figure 5.14: Variation of peak stress with beam element count

contains a high open area ratio, this positioning is necessary to ensure that actuation at the target location is possible.

From the seed cell the unit-cell is tessellated along the repetition vectors until the domain is filled. Duplicated nodes, due to the connections between unit cells, and any nodes outside of the domain boundary are then removed. All nodes connected to a single beam represent the boundaries of the domain and so are constrained in all degrees of freedom. Actuation is applied to the nodes forming the central cell hub in the form of a fixed displacement load normal to the surface. The other degrees of freedom of these actuation nodes are constrained. This is representative of the connection of an actuator to a solid hub. A schematic of a typical simulation is shown in Fig. 5.13(b).

5.4.3 Lattice Optimisation

Using the hex-chiral lattice geometry, the optimisation process described in Sec. 5.1 was repeated. The original design variables remained as previously defined and the additional parameters required to fully define the lattice unit-cell: spar length l, relative core radius r/l and spar width w were also included. A full list of variables and their bounds is given in Tab. 5.5.

Description	Symbol	Lower Bound	Upper Bound	Initial Condition
Spar Length (mm)	ℓ	2.5	10.0	6.0
Core Radius (ratio)	r/ℓ	0.1	0.45	0.3
Boundary Vertex (mm)	x_1	72.5	106.0	70.0
Boundary Vertex (mm)	z_1	10.0	50.0	30.0
Boundary Vertex (mm)	x_2	19.0	52.5	20.0
Boundary Vertex (mm)	z_2	10.0	50.0	35.0
Actuation Location Parameter	P_A	0.1	0.9	0.5
Actuation Height (mm)	y_A	1.0	10.0	3.0
Yield Stress (GPa)	σ_{yield}	—	1.0	–

Table 5.5: Lattice design parameters and their constraints

The optimisation process was repeated for five iterations and checked for convergence. A rapid decrease in objective function is observed in Fig. 5.15 at the first iteration after which the improvements are incremental. The first iteration is also associated with an

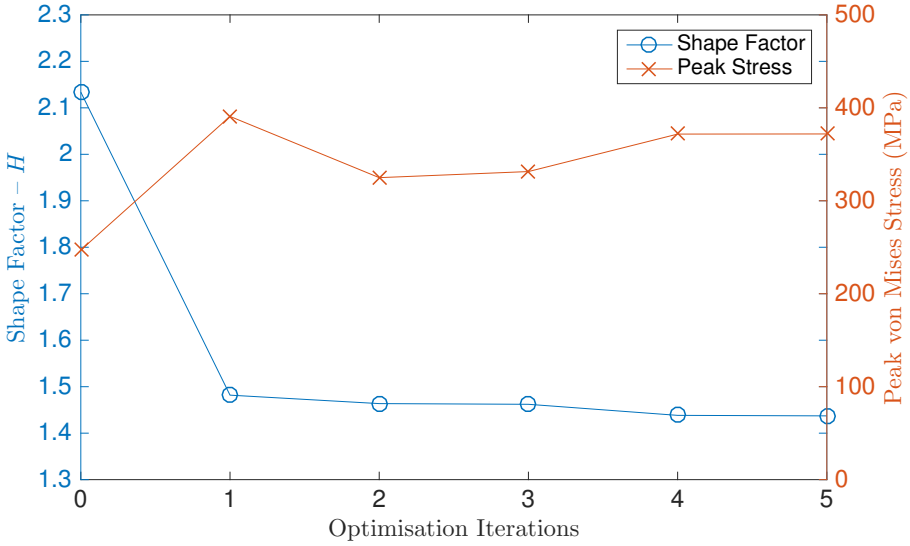
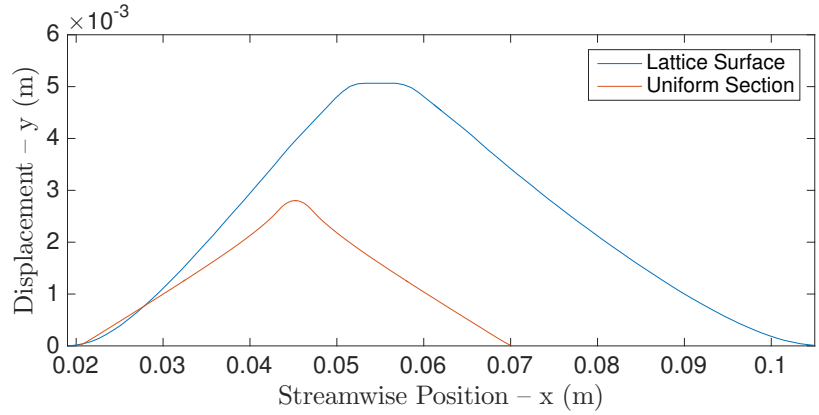


Figure 5.15: Plot of optimisation function convergence with Shape factor (○) and corresponding peak von Mises stress (×)

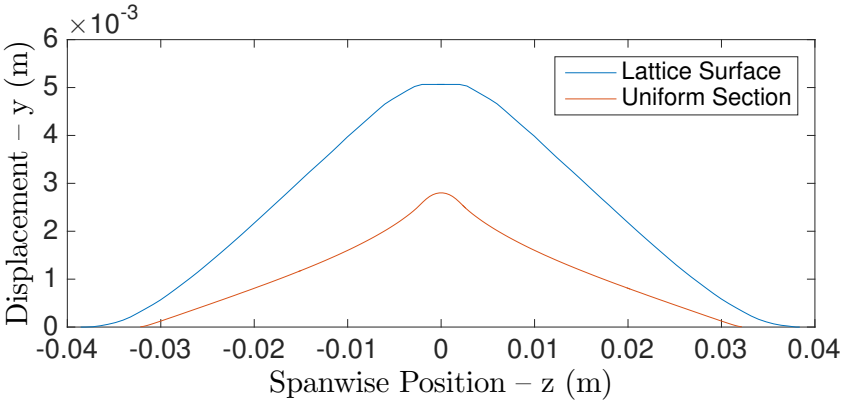
increase in peak stress which then stabilises. Unlike the previous case, however, the peak stress remains significantly below the yield criterion of the material. Sectional views of the deformed geometry are shown in Fig. 5.16 and the geometry from the uniform skin is also included for comparison.

Description	Symbol	Final Value
Spar Length (mm)	ℓ	7.94
Core Radius (ratio)	r/ℓ	0.302
Boundary Vertex (mm)	x_1	106.0
Boundary Vertex (mm)	z_1	34.9
Boundary Vertex (mm)	x_2	19.0
Boundary Vertex (mm)	z_2	39.0
Actuation Location Parameter	P_A	0.419
Actuation Height (mm)	y_A	0.00506

Table 5.6: Lattice design parameters and their optimal values



(a) X-Y section at $z = 0$ m (mid-plane)



(b) Z-Y section at $x = 0.055$ m (peak deformation)

Figure 5.16: Deformed geometry resulting from the converged optimisation function. The deformation achieved with a simple shell in the previous section is included for comparison.

5.4.4 Experimental Validation

A reproduction of the deformed geometry was produced as described in Sec. 4.5 for testing experimentally. The selective removal of material to form the lattice structure significantly increases the flexibility of the surface, allowing the formation of larger deformations. In order to ensure that the deformed surfaces maintains the intended geometry under the pressure loading present in use, the mean pressure field calculated during the LES is applied to the deformed lattice in an additional FEA. The mean magnitude of nodal displacement under aerodynamic loading is 1.048×10^{-4} m. The additional deformation is equivalent to 2.07% of the peak deflection. A rigid version of the target geometry therefore suitably represents the lattice surface in the following experiment.

The facility used is a closed circuit wind tunnel with working section 0.457×0.457 m (18" $\times$ 18") and length 3.5 m. The base experimental model was a polished aluminium plate with dimensions 220×150 mm with an elliptic leading edge. The model was mounted 1 m downstream of the 6:1 contraction. The model incidence was adjusted to provide a pressure gradient of $\frac{dp}{dx} \leq 0.2$ Pa/m at working velocity.

The sPIV laser sheet was directed to be perpendicular to both the oncoming flow and the model surface at $x = 150$ mm. Two Phantom Miro 1 MPix high-speed cameras were arranged with one on either side of the tunnel. The camera field of view is 74×40 mm (spanwise $\times$ wall normal) and the final PIV interrogation windows are 16×16 pixels (0.194×0.194 mm) with 75% overlap. A schematic of the model setup is shown in Fig. 5.17.

The resulting boundary layer velocity profiles are shown in Fig. 5.18 and the corresponding values for shape factor are given in Tab. 5.7. The experimental data for the baseline case compare well with the computational results however the velocity is slightly overestimated by the CFD simulation. The alterations of the boundary layer downstream of the adaptive device are qualitatively captured, however the geometry change produces a greater momentum transfer towards the wall than predicted. This leads to a greater velocity deficit in the wake. Increased wake losses are undesirable as they lead to increased viscous drag. However, as an adaptive structure the proposed solution is retractable and thus the drag penalty is not present when the control is not required.

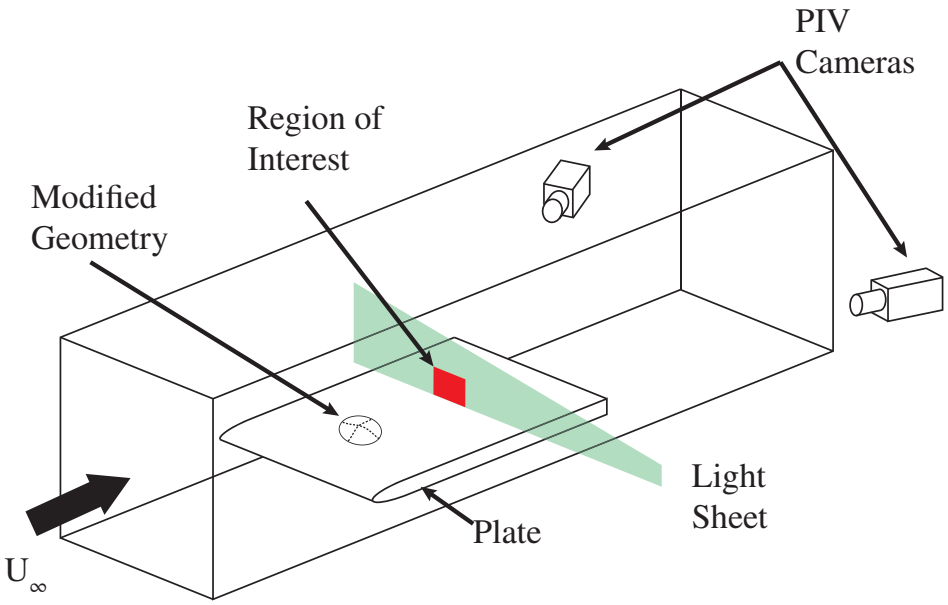


Figure 5.17: Scheme for Plate Experiment in 18-inch Tunnel

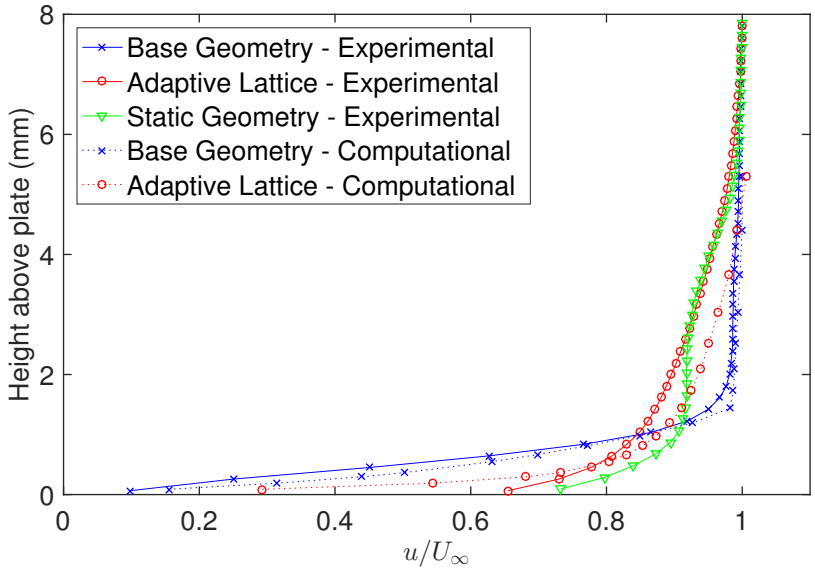


Figure 5.18: Mean boundary layer profiles for the 'clean' condition (×), a discrete forwards wedge vortex generator (▽) and with the optimised deformation (○). Experimental and computational results for all cases are shown as solid (—) and dotted (· · ·) lines respectively.

Shape Factor H	Computational	Experimental
Base Condition	1.81	2.06
Uniform Section	1.54	–
Forwards Wedge VG	1.31	1.12
Adaptive Geometry	1.42	1.16

Table 5.7: Comparison of boundary layer shape factors

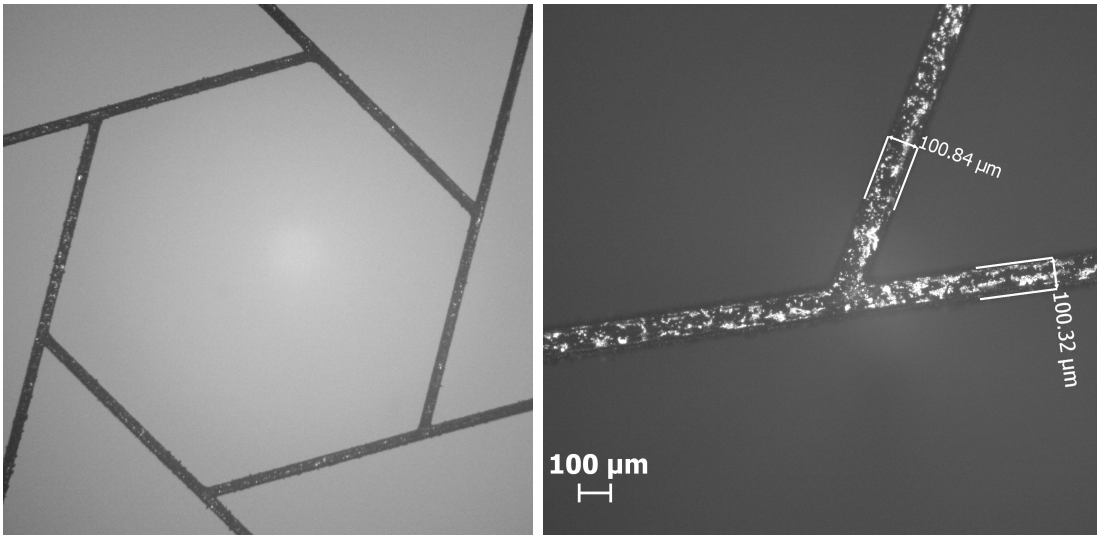


Figure 5.19: Typical node of the manufactured lattice viewed under an optical microscope

5.5 Implementation

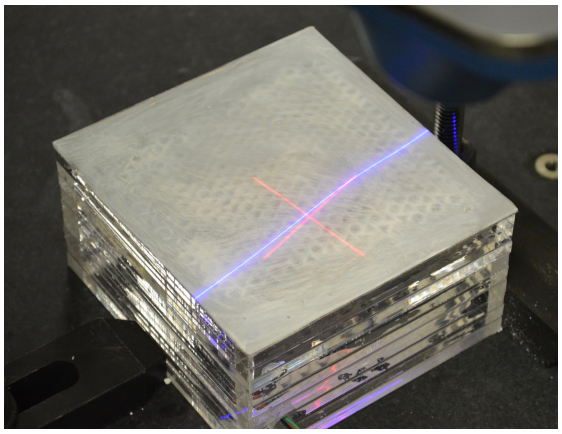
Having experimentally demonstrated the beneficial impact of the predicted geometry change on the flow, the physical structure was produced to confirm the morphed surface topology and the elasticity of the proposed design. The lattice is manufactured to the parameters from the optimisation study from 0.1 mm thick stainless 1.4310 spring steel with thickness tolerance ±4 µm as described in Sec. 4.5. The machined structure is inspected under a calibrated microscope and, of the samples tested, the maximum discrepancy from the target thickness was +1.2 µm. A magnified node from the lattice is shown in Fig. 5.19 with associated thickness measurements.

Once inspected for geometrical accuracy, the lattice is encapsulated in a 0.5 mm thick elastomer skin of EcoFlex silicone 00:50 rubber. This skin provides a necessary impermeable boundary over the voids of the lattice. The rubber skin is not included in the FE model as, with a Young's Modulus $E \approx 29.5$ kPa, the stiffness of the skin is significantly

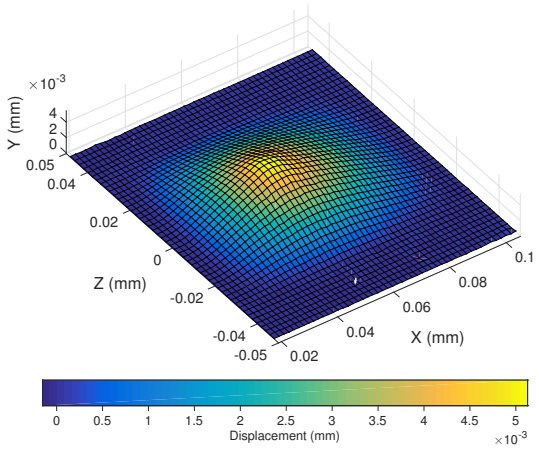
lower than that of the lattice and thus has a negligible effect on the geometry of the deformed surface. To produce a skin devoid of air bubbles or other imperfections, the Silicone is de-gassed in a vacuum chamber for 10 minutes prior to application. The lattice is located inside a mould and a measured volume of silicone is applied and levelled over the surface. Once cured, the procedure is repeated for the reverse side.

The encapsulated lattice structure is fixed to a plastic housing for measurement and is shown in Fig. 5.20(a). Actuation is provided by a Haydon Kirk G4 19000 stepper motor driven linear actuator. This actuator has a step angle of 7.5°/step and a linear travel of 12.5 μm/step. The motor is driven with a MSD415 micro-stepping motor driver which further subdivides each step into 64 increments giving a theoretical positional increment of 0.20 μm.

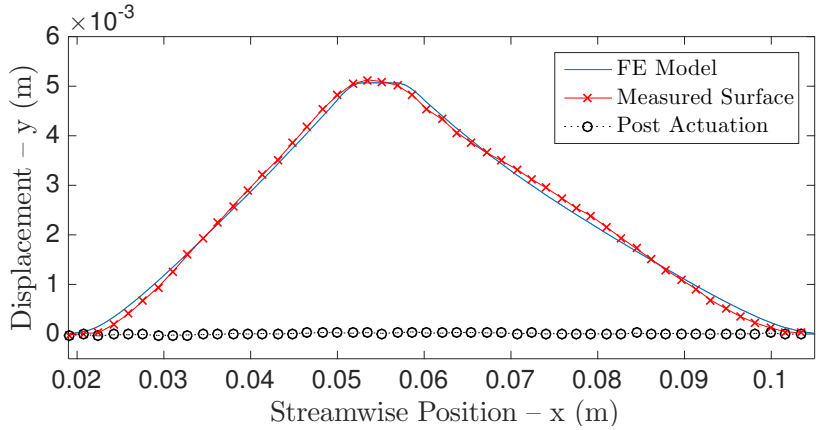
A baseline measurement was taken of the lattice surface before it was deformed to the specified actuation height. The measured surface in the deformed state is shown in Fig. 5.20(b). Streamwise and spanwise sectional measurements through the actuation location are shown in Figs. 5.20(c) and (d) and compared to the FE result. The measured surface is seen to compare well with the computed geometry. The model was re-measured in the un-actuated position and this data is also included in these plots. These data demonstrate that the structure returns to the baseline case following actuation and thus that the deformation is fully elastic.



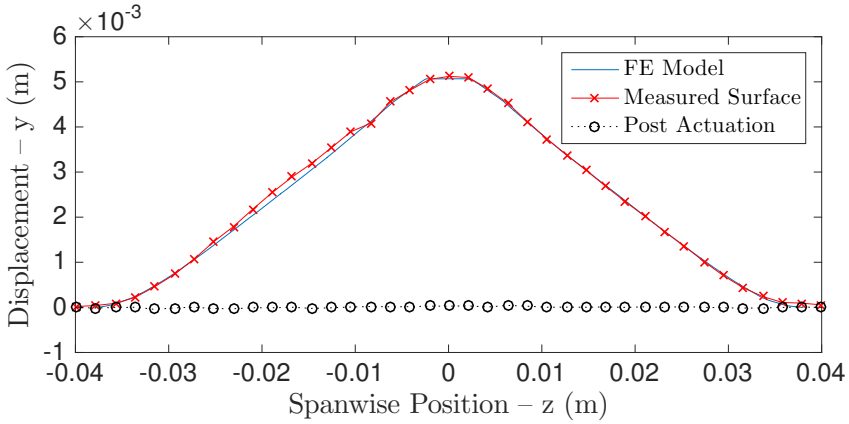
(a) Deformed lattice model during laser measurement



(b) Measured surface deformation



(c) X-Y section at $z = 0$ m (mid-plane) showing the actuatued and unactuated positions



(d) Z-Y section at $x = 0.055$ m (peak deformation) showing the actuatued and unactuated positions

Figure 5.20: Measurement and comparison of manufactured lattice displacement to finite element predictions.

5.6 Discussion

In this chapter the development of a local, elastic, 3D adaptive structure to re-energise a fluid boundary layer has been described. A gradient based optimisation method is used to identify the optimal parameters within the complex design space. The use of a dynamic penalty function allows a nonlinear yield stress constraint to be incorporated into the process without the loss of gradient information.

Initially, the design methodology followed was taken from current literature in which the optimisation objective is to mimic an existing static geometry. This is achieved by minimising the positional RMS error between the deformed surface and the target geometry. This geometry must be selected such that a mapping between the original morphing surface and target geometry are possible. In this case, the most common separation control device, the vane-type VG, is discarded as the required geometry height $z(x, y)$ is a non-singular function of the surface co-ordinates. Instead, the selected geometry was that of a forward wedge VG, the geometry of which meets this requirement.

The boundaries of the clamped domain, actuation point and deformation height were defined as the design parameters for optimisation. The optimisation was conducted using a 0.1 mm thick Stainless Steel alloy EN 1.4310 as the base material. Once converged, the resulting morphed geometry was incorporated into an LES of a plate with a zero pressure gradient to evaluate the effectiveness of the device at re-energising the near wall flow.

The boundary layer downstream of the device was seen to thicken without increasing the momentum in the near wall flow. Examining the positional error distribution over the surface, this is determined to be due to the necessary compromise, which exists in any adaptive surface, between position and curvature distribution. Previous morphing structures, including those for which this method was developed, are principally concerned with modifying the bulk, inviscid, flow across an aerofoil. This can be produced effectively by altering the location of the fluid boundary which in turn alters the surface curvature.

In order for a VG to be effective, in addition to the production of a variation in spanwise pressure gradient, the flow must then locally separate from the surface. This releases the near wall vorticity, produced by the spanwise pressure gradients, into the rest of the flow field and sets up the desired mixing effect. In the case of a static VG, without the elasticity or continuity constraints of an adaptive surface, this is achieved with a sharp discontinuity of gradient at the device trailing edge. The distribution of curvature, as

well as position, is therefore critical to the efficacy of such a device and this information must be incorporated into any geometric objective. The appropriate weighting for these higher order displacement terms is not known *a priori* thus making the problem very difficult to pose. In addition, for an adaptive VG, the local separation must be achieved with continuous elastic curvature. With these additional constraints, which directly impact the objective, the optimal geometry may bear little resemblance to an effective, unconstrained, solution.

A replacement objective function is proposed in which the LES, employed previously to quantify the performance of the adaptive device, is used. The downstream shape factor H is instead used to quantify the distribution of momentum through the boundary layer. Minimising H drives the algorithm to a solution with higher near-wall momentum and thus greater resistance to separation.

The optimisation was repeated with the new objective function and a reduction in computed shape factor from 1.81 to 1.54 is achieved. A rapid increase in von-Mises stress was observed as a key limitation in making further gains. In-plane membrane stresses formed approximately 40% of the total peak stress in the structure and are caused by the necessary elongation of material required to vary the Gaussian curvature of a surface.

The use of a 2D auxetic ($\nu < 0$) lattice as the deformable surface is proposed in order to increase the yield strain of the material, and so increase the achievable deformation. In addition, the ability to vary the unit cell topology independently of the material thickness allows the decoupling of bending and membrane stiffnesses and so the tailoring of the bulk material properties to the required task. The optimisation process was repeated with the lattice unit cell parameters added to the optimisation variables. A further improvement in shape factor to $H = 1.42$ is achieved with the lattice based surface.

The effect of the optimised geometry on a boundary layer over a plate was validated in a sPIV wind tunnel experiment on a flat plate model at $Re = 3.5 \times 10^5$. The deformed surface geometry was reproduced using a high precision 3D printer. The resulting boundary layer velocity profiles compare well with the baseline condition however the simulation accuracy decreases with increasing surface complexity. The desired momentum transfer from the freestream to the boundary layer is however qualitatively captured and an improvement in downstream shape factor is observed.

Following the validation of the effect of the deformed geometry on the boundary layer, a physical model was produced to confirm both the fidelity of the FE simulation and the

elasticity of the deformation. A micromachining laser was used to produce the lattice geometry from 0.1 mm thick Stainless Steel shim stock. The manufactured lattice was inspected for dimensional accuracy before being cast into a low-modulus silicone surface. The device geometry was measured using a 3D laser scanning probe and compared well with the FE predictions. The surface was remeasured following the actuation and returned to the datum location, demonstrating the elasticity of the deformation.

5.7 Summary

A novel device for energising the boundary layer has been developed using a 2D lattice surface. The bending dominated chiral lattice allows large strains and positive Gaussian curvature change as required for significant out of plane geometry modification in a finite domain. The optimal topology has been determined using a computational fluid result as the objective function. The resulting geometry for a flat plate has been tested experimentally and the results compare favourably to those calculated by the objective function for this condition. Unlike the canonical flow over a flat plate, the separating flow field from a curved surface of an aerofoil is topologically complex. The following chapter investigates this flow to further understand the intended application of this device.

Chapter 6

Cellular Separation

This chapter presents the results of an experimental investigation into the behaviour of an unsteady stall cell on the suction surface of a NASA GA(W)-1 aerofoil. The experimental model and wind tunnel set-up are described in Sec. 6.1. The results of a preliminary investigation to confirm the existence and periodicity of the stall cells on the model are reported in Sec. 6.2. From these results a fixed operating point is selected and further investigations on the mean velocity and surface pressure are conducted in Sec. 6.3 and 6.4. Analysis of the surface pressure signals in the frequency domain in Sec. 6.5 identify two time scales in the pressure fluctuations and proper orthogonal decomposition is applied to the velocity fields in Sec. 6.6 to identify the dynamic modes responsible. Finally, conclusions are drawn from these results and analogies to other canonical flows are discussed in Sec. 6.7.

6.1 Experimental Setup

Experiments regarding the separation of flow from an aerofoil were conducted in the Donald Campbell tunnel. This is a closed-circuit wind tunnel with a working section of 1.38 m $\times$ 1.22 m $\times$ 3.0 m with a contraction ratio of 4.92 : 1. The air is driven through a four-bladed fan with a maximum free-stream velocity of approximately 40 ms^{-1}. The turbulence intensity Tu at 25 ms^{-1} is less than 0.1%.

The experimental model, described below, is suspended from a drag balance in the roof of the tunnel. The mechanical nature of the drag balance makes it unsuitable for measuring

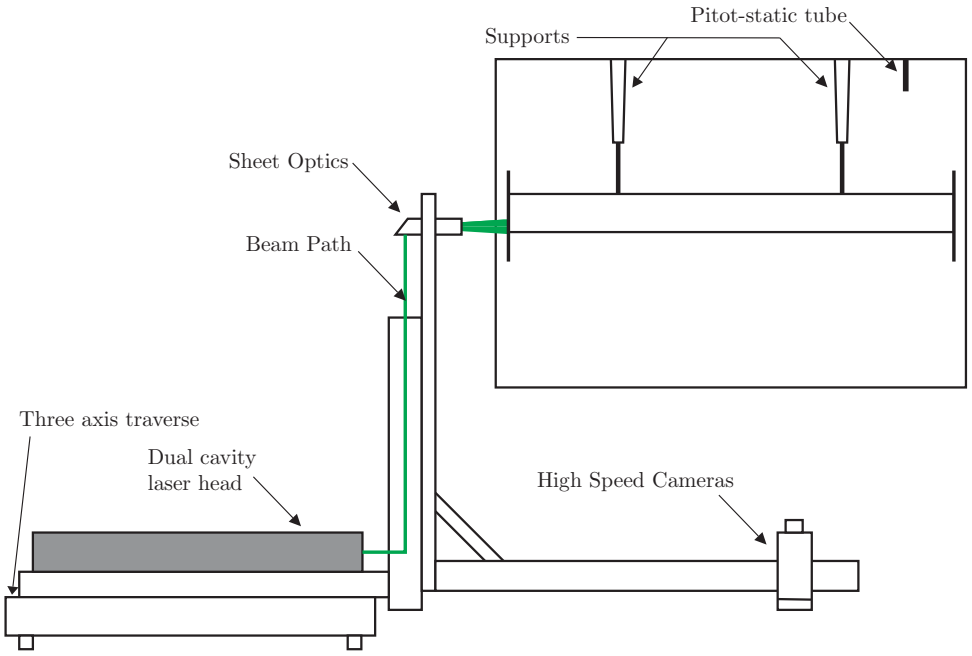
unsteady forces, such as those from a separating aerofoil, however provides a suitable rigid mounting point. The model is mounted within the tunnel in an inverted orientation to allow optical access through customised glass panels in the floor and side wall for laser based flow measurement.

The PIV laser, cameras and optics are mounted on a 3-stage linear traverse. Once aligned, this allows the light sheet and cameras to move in the same frame of reference. This enables recording of data from planes near to the model for which it would otherwise not be possible to obtain an accurate calibration. The PIV equipment was used in two arrangements to obtain different fields of view. The light sheet may either enter: through the side wall, parallel to the model, with cameras arranged underneath the tunnel as shown in Fig. 6.1; or through the tunnel floor, perpendicular to the model chord, with cameras are mounted on either side of the working section. The overlapping field of view for the cameras is 178.6 × 133.7 mm (spanwise × streamwise) and each 32 × 32 interrogation window corresponds to 1.1 × 1.1 mm.

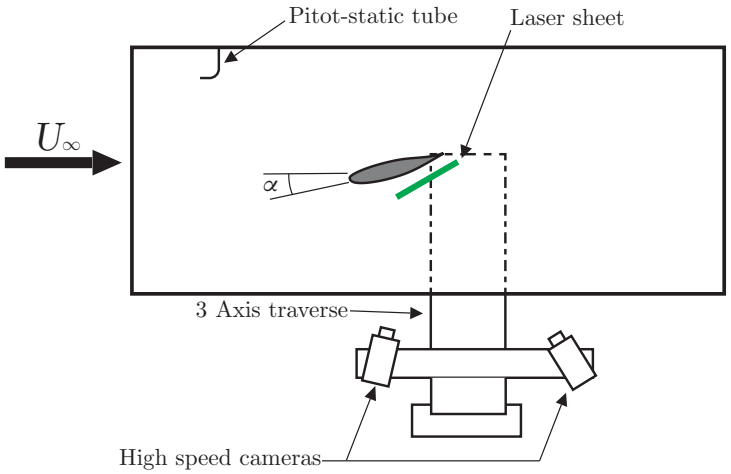
6.1.1 Dynamic Pressure Fluctuations

As reviewed above, it has been previously proposed that the frequency of fluctuations in separating wakes are linked to significant oscillations in the freestream flow. To account for this, measurements were made of the background pressure fluctuations using a PCB Piezotronics 377B20 microphone, and turbulence intensity using a Streamline CTA hot-wire system. In both cases the signal was sampled at 40 kHz for 1200 s and the pre-multiplied spectra of the resulting signal is shown in Fig. 6.2. The frequency is normalised using the characteristic length of the model in the principle configuration investigated ($D = 0.22 \sin(15°)$).

In both cases the principle peak appears at normalised frequency $St \approx 0.079$ ($f_p \approx 34.7$ Hz) and this relates to the blade passing frequency of the four-bladed fan rotating at a measured 8.19 Hz. Noise is visible in the spectra at higher frequencies around $St \approx 1.0$. The source of these oscillations is unclear, however they are observed nearly an order of magnitude higher than those anticipated in this work and so pose limited risk to the experiment.

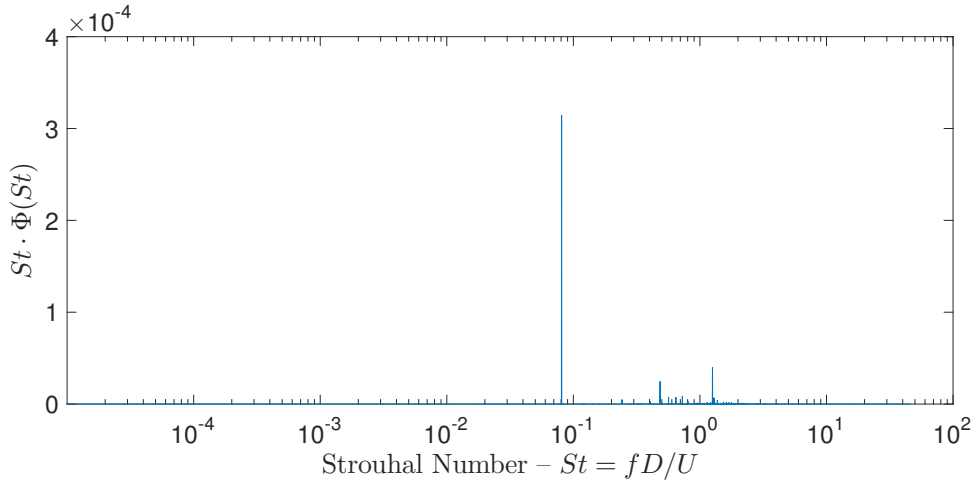


(a) Front View

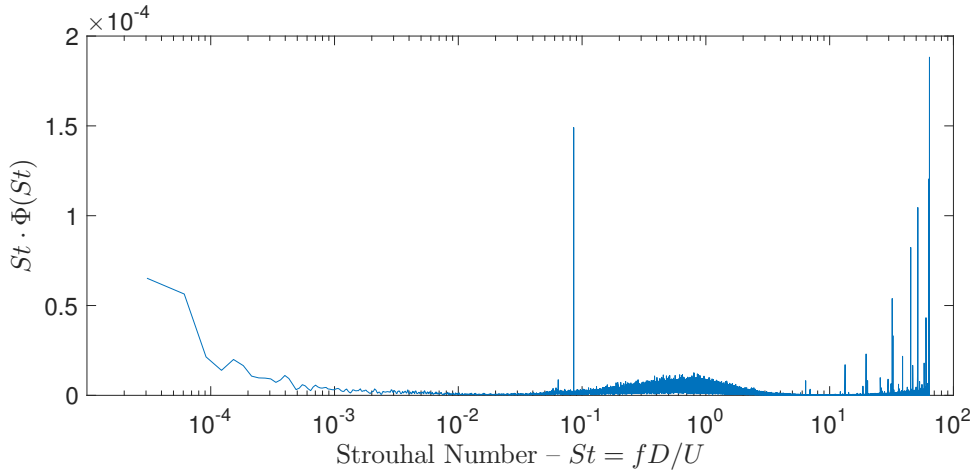


(b) Side View

Figure 6.1: Experimental setup of the GA(W)-1 model in the Donald Campbell wind tunnel



(a) Frequency Spectrum of Freestream Pressure Fluctuations



(b) Frequency Spectrum of Streamwise Velocity Fluctuations

Figure 6.2: Freestream Characteristics of 5×4 Wind Tunnel at $U = 24.5$ ms^{-1}

6.1.2 Wind Tunnel Model

The aerofoil model used in this experiment is an unswept NASA GA(W)-1 aerofoil profile as described by McGhee and Beaseley (1973). This is a sub-critical high-lift aerofoil profile which has been shown to exhibit 3D separation in previous research (Flynn et al., 2001). It is the aim of this thesis to identify and study the characteristics of naturally forming stall cells in the pre-$C_{L_{max}}$ range of incidence. Previous experimental studies (Winkelmann and Barlow, 1980; Yon and Katz, 1998) indicate that in this range a stable pattern of stall cells is observed on a model with sufficient aspect ratio. Based on this research, in order to obtain three stable cells, two complete and two half-cells, the model aspect ratio must be in the range $6 < AR < 9$.

To allow the largest operating Re range and measurement resolution of the model, $AR = 6$ was selected. The model is separated from the tunnel walls to mitigate the effect of the tunnel boundary layer and the remaining span of the tunnel is used for the model bounding dimensions, giving a span of 1.32 m and a chord of 220 mm. The maximum blockage (at $\alpha = 20°$) of the test section is approximately 6%.

The model was manufactured in five segments using a Connex Objet 350 3D printer before being assembled and hand finished to provide a continuous surface. These segments are supported using two 8 mm diameter steel rods running the full span of the model. Steel ribs connect these spars and the model is mounted from these in three locations. Two main pivoted struts run from the pressure side of the aerofoil and one central tail sting runs from near the suction surface trailing edge to $x/c = 2$ and used for incidence control.

A series of removable panels are included on the suction surface of the wing to allow both the surface profile and instrumentation to be altered between experiments. The forward panels are deigned to be replaced with self-reacting morphing panels later in the project. The rear panels may be altered as required to provide instrumentation to identify regions of recirculating flow. Gaps between the panels and the base model geometry are smoothed with a sandable polyurethane filler to provide a continuous surface. Acrylic end plates are used to prevent wing tip effects.

6.1.3 Boundary Layer Conditioning

Under natural conditions the aerofoil selected exhibits a laminar separation in the range of Reynolds number under consideration. Depending on conditions, this may form a laminar

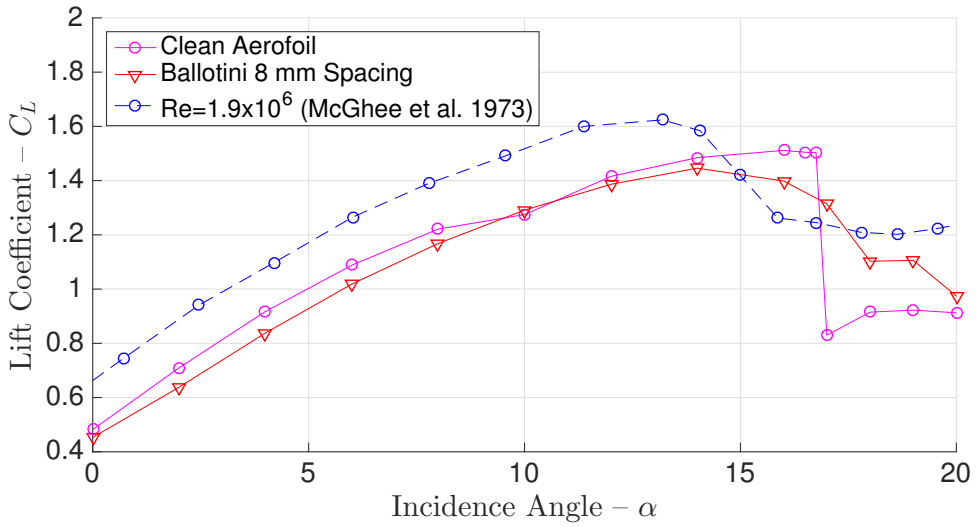


Figure 6.3: Effect of Ballotini on Lift Coefficient

separation bubble at $x/c \approx 0.05$ (Yang and Hu, 2008). The transitional behaviour over a laminar separation bubble can act as a source of low frequency pressure fluctuations (Zaman et al., 1989) which are unreleated to turbulent separation.

As this work focuses only on turbulent separation, independent of the upstream transitional behaviour, the boundary layer is tripped to turbulence at $x/c = 0.04$ upstream of the position of any potential separation bubble. A strip of glass spheres termed ballotini with diameter $0.4 < d < 0.8$ mm was applied in the desired location and adhered to a thin layer of varnish at each location. The ballotini were applied with 8% coverage as recommended by Versmissen (1974).

The effect of the ballotini on the lift coefficient of the aerofoil, as measured using the tunnel force balance, is shown in Fig. 6.3. The clean aerofoil demonstrates a sudden drop in lift over a 0.5° range indicative of laminar, leading edge, separation. With the boundary layer trip in place, the lift curve is seen to be more benign and qualitatively comparable to the high Re case from McGhee and Beaseley (1973).

6.2 Selection of Experimental Conditions

Several authors, reviewed in Sec. 2.1.3, have described the existence and distribution of naturally occurring stall cells on the surface of an aerofoil with moderate to large AR. For certain incidence angles, dependent on Re, α, and aerofoil profile, the patterns are

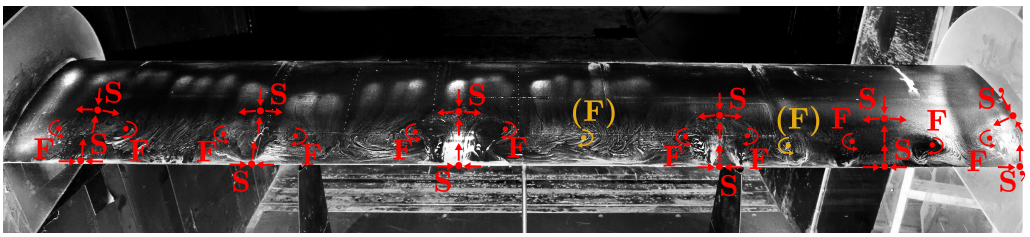
self-stabilising and for other incidences the distribution 'switches' randomly between two configurations. In order to study the characteristics of stall cells on the surface of the GA(W)-1 aerofoil without introducing artificially created disturbances, a set of conditions under which a stable pattern is observed must be found.

6.2.1 Skin Friction

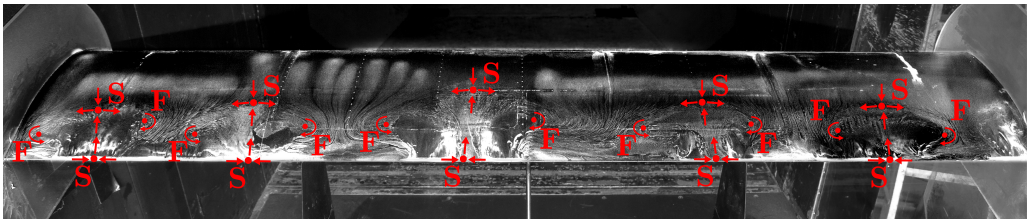
Oil flow visualisation was conducted at a range of incidences to qualitatively capture the layout of skin friction lines on the wing surface. The experiment was run with a free-stream velocity of 25 ms^{-1} and the selected incidence angle until the paraffin evaporated, fixing the skin friction patterns. Figure 6.4 shows a typical series of surface flow patterns observed over the partially-stalled incidence range. The critical points have been marked, along with the local flow directions, in each image based on the observations made during of a number of experiments. A repeating series, consisting of two saddle points (marked S) and two counter-rotating foci (marked F), is observed at each incidence, indicating a periodic array of stall cells. As the number of nodes and saddles are equal, the topological rules described in Sec. 2.1.1 are maintained. In the regions between the Focus-Saddle-Focus structures, the undisturbed oil flow pattern is seen to continue farther along the chord toward the trailing edge than in the vicinity of the saddle point. This is particularly evident in Fig. 6.4(e) but can be observed in all cases and is indicative of regions of attached flow between the cells. As reported by previous authors, and reviewed in Sec 2.1.3, the separated area within each cell is seen to increase with incidence angle. Clear

At $\alpha = 12^\circ$ and 16° the stall cell positions were observed to switch between two stable distributions during a single run. Both distributions were repeatable and spatially offset by approximately half of the spanwise period. No characteristic time period was observed with each layout remaining steady for between approximately 2 – 30 seconds before switching to the alternate layout. In Fig. 6.4(a) this is demonstrated by the isolated foci (marked in yellow) visible in the oil flow pattern.

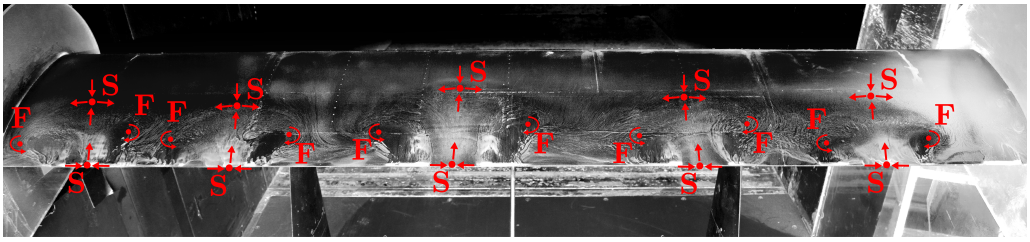
Oil flow visualisation provides a rapid and reliable method to investigate the near wall flow topology over a large surface. Due to the nature of this method however, the results are time-averaged and it is therefore only possible to obtain a qualitative understanding of the mean surface flow of an unsteady flow field. In order to obtain quantitative data on the topology and stability of a stall cell another method must be used.



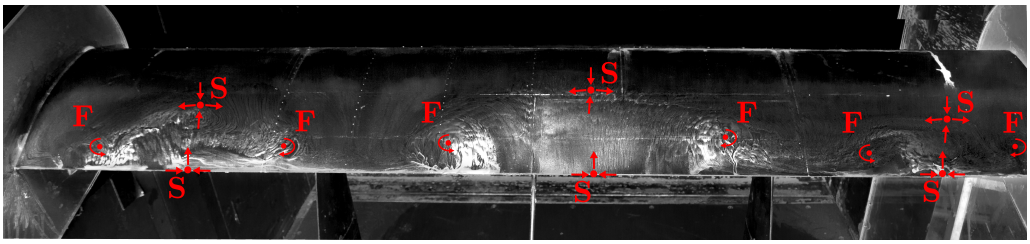
(a) 12°



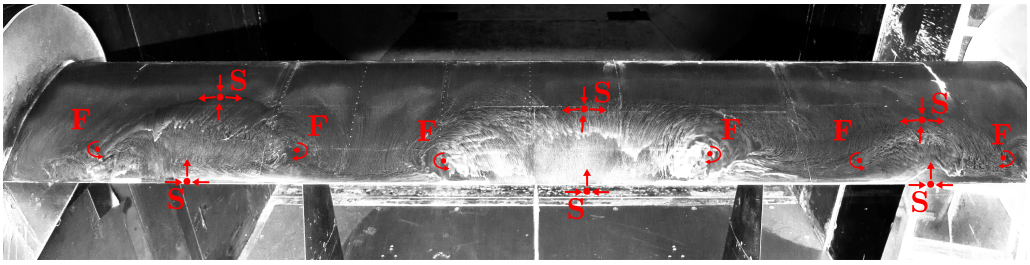
(b) 14°



(c) 15°



(d) 16°



(e) 17°

Figure 6.4: Surface oil flow visualisation of the wall shear stress distribution for a NASA GA(W)-1 aerofoil at $Re \approx 3.5 \times 10^5$. Critical points are overlayed and distinguished between Saddles – S, and Foci – F.

6.2.2 Velocity Field

In order to interrogate the highly three-dimensional flow field non-intrusively, a series of stereo Particle Image Velocimetry sPIV experiments were conducted and processed in accordance with the procedure described in Sec. 4.4. Of particular interest for this work is the three-dimensionality of the separating stream surface. The experiment was therefore initially arranged to section the separating region into a series of offset planes parallel to the trailing edge.

To allow the study of stall cell topology and its inherent dynamics it is necessary to select a condition where the mean position of the cell is steady. Preliminary investigations were therefore conducted through the range of incidences where stall cells were observed in the previous investigation. A variation in velocity was also investigated to evaluate the sensitivity of cell size and position to the chord Reynolds number. Based on the results of this preliminary study, an incidence of $\alpha = 15^\circ$ at $Re = 3.5 \times 10^5$ was selected as these conditions produced a stable array of cells of a size to allow a reasonable resolution with the instrumentation on the model. The spanwise location of the subject area was selected in each case to capture the key features of the stall cell: the central saddle point S, a focus F, and the attached flow surrounding the cell.

6.3 Mean Velocity Field

The velocity field parallel to the model trailing edge was recorded at seven planes defined by the vertical distance between the light sheet and the model trailing edge y_{TE}. The mean flow field was computed using data from eight independent acquisition sessions, each recording 2734 vector fields. All data has been normalised by the free-stream velocity associated with each acquisition session.

The left-hand sub-figures of Fig. 6.5 (a, c, e ...) show the in-plane streamlines and are coloured by the mean velocity magnitude. The characteristic 'mushroom' shape of stall cells which was visible in the surface oil flow visualisation is clearly observed in the planes closest to the wall. As the plane moves away from the model the upstream location of the separating streamsurface can be seen to retreat downstream. As this occurs the focus, originally visible at spanwise position relative to the saddle point $z_s/c = 0.49$, moves towards the centreline of the cell, narrowing the overall separated width.

The recorded turbulence intensity at these planes is shown alongside the mean values in sub-figures (b, d, f ...). The in-plane streamlines are again shown for reference. A region of high velocity fluctuation is visible upstream of the saddle point which extends spanwise across the separating streamsurface away from the wall.

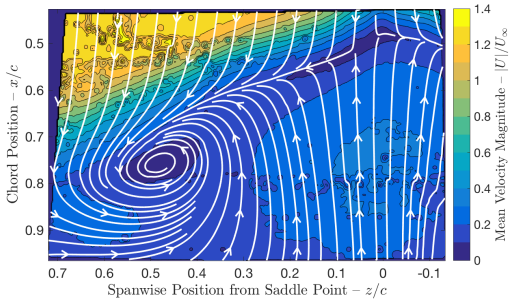
A region of measurement noise exists in the region upstream of the focus in planes $y = 15$ mm and 20 mm. This area suffered from high levels of background reflection from the model during experimentation and, on occasion, caused the sensor to saturate. In saturated regions, PIV cross-correlation is not possible, or is inaccurate due to the lack of variation in the intensity readings. This contamination is also not removable through background subtraction for the same reason. In this instance however, the contamination is not located in a region of high importance to the current study and can be seen to reduce as the height increases.

In order to capture the downstream behaviour of the separating region, the experiment was reconfigured to record a series of parallel planes at fixed spanwise extents throughout the cell and extending into the wake. The velocity fields for four parallel planes, located at spanwise distances from the saddle point z_s are shown, alongside the recorded turbulence intensity in Fig. 6.6.

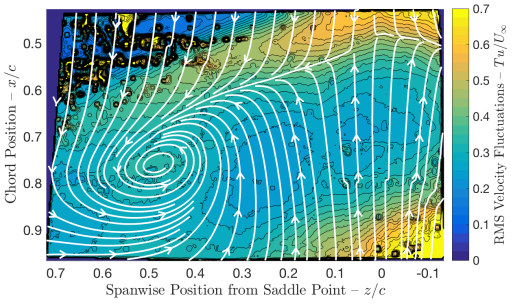
The mean flow fields, sub-figs. 6.6(a, c, e, g) show in-plane streamlines and are coloured by spanwise velocity w. The contour $w = 0$ is shown in bold in the mean velocity plots for clarity. At the saddle point, the main recirculation vortex is clearly visible at $x/c \approx 0.95$ and $y/c \approx 0.25$. The secondary trailing edge vortex is also visible at $x/c \approx 1.25$. A slight spanwise velocity gradient is visible through the separation line and this is most probably due to positional error of the light sheet with respect to the true mean spanwise location of the saddle point.

At position $z_s/c = 0.24$, the recirculation vortex is visible at $x/c \approx 1.05$ and $y/c \approx 0.2$. A significant negative spanwise velocity gradient is now visible in the flow field with upstream flow moving away from the saddle point and downstream flow travelling into the stall cell. The contour $w = 0$, shown in bold, passes though the focus of the recirculation vortex. This demonstrates that the vortex is inclined to the plane at this position.

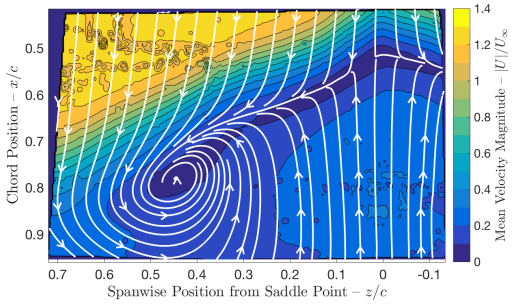
The velocity field at the spanwise position of the focus in Fig. 6.5(a) is shown in Fig. 6.6(g). The streamwise position of the focus in the previous figure corresponds with the position of the $w = 0$ contour and lies on the boundary of the recirculating region. An additional separation vortex is visible near to the trailing edge however the spanwise velocity is



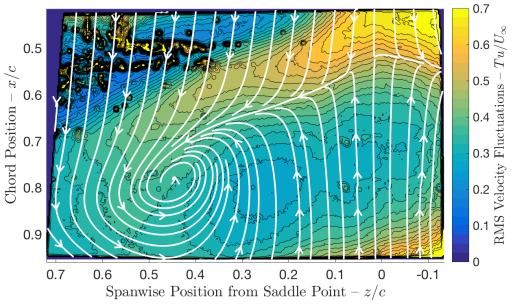
(a) $\bar{U}$ at $y_{TE} = 15$ mm



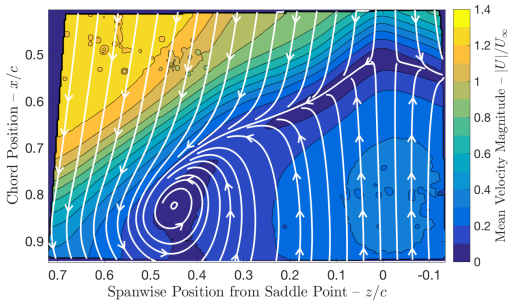
(b) Turbulence intensity at $y_{TE} = 15$ mm



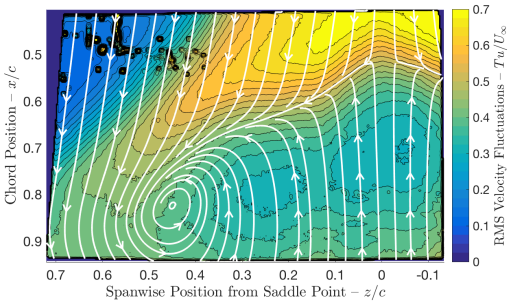
(c) $\bar{U}$ at $y_{TE} = 20$ mm



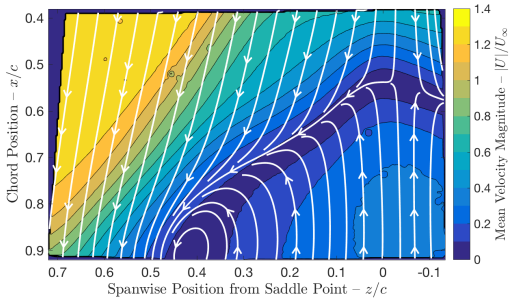
(d) Turbulence intensity at $y_{TE} = 20$ mm



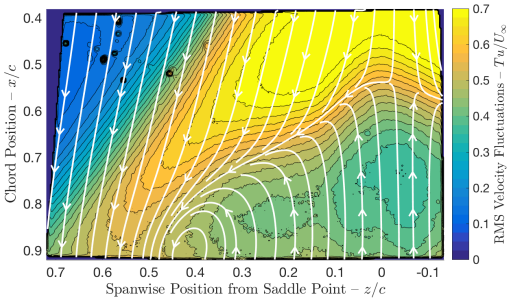
(e) $\bar{U}$ at $y_{TE} = 25$ mm



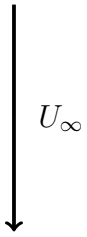
(f) Turbulence intensity at $y_{TE} = 25$ mm

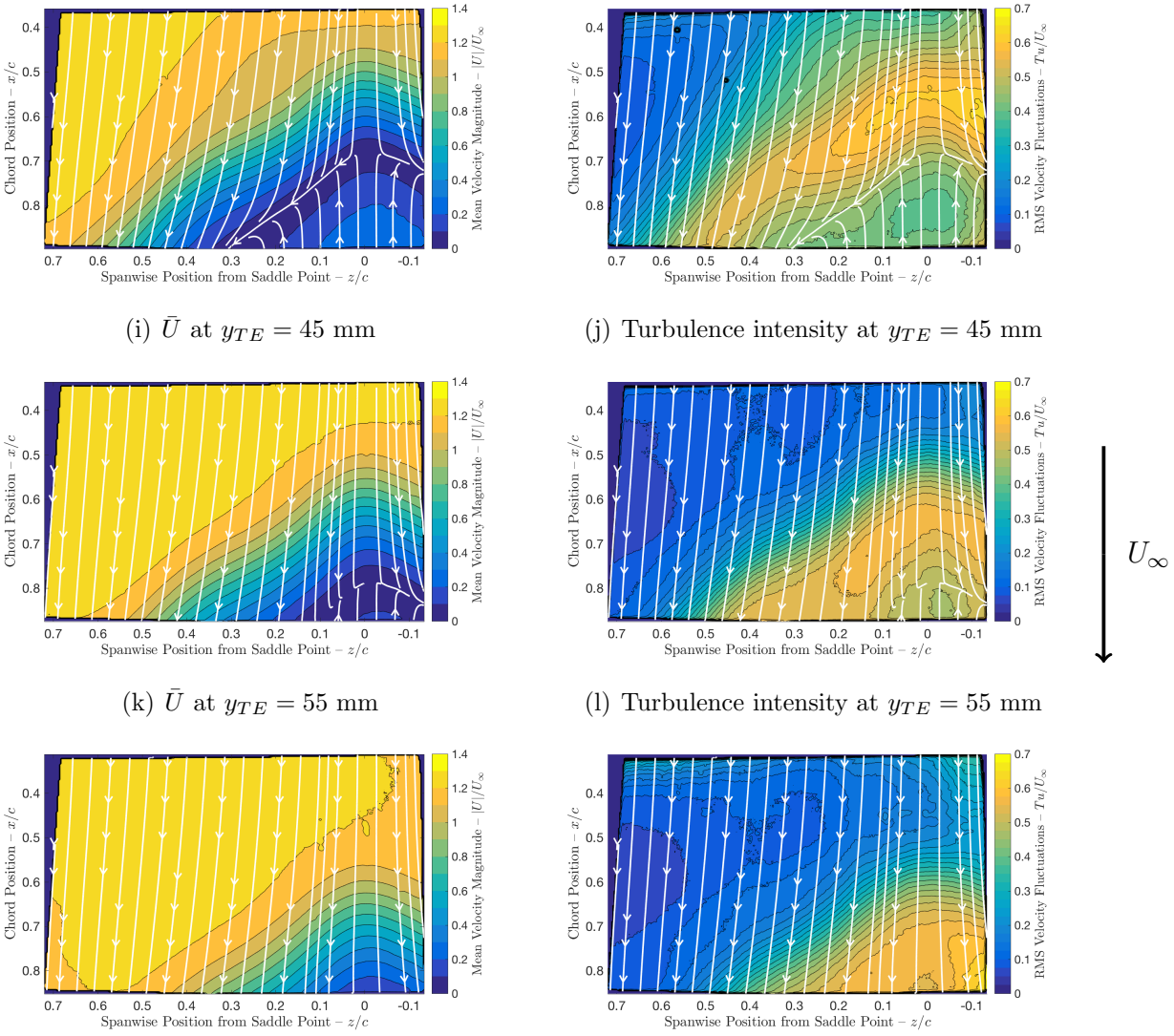


(g) $\bar{U}$ at $y_{TE} = 35$ mm



(h) Turbulence intensity at $y_{TE} = 35$ mm





(i) $\bar{U}$ at $y_{TE} = 45$ mm

(j) Turbulence intensity at $y_{TE} = 45$ mm

(k) $\bar{U}$ at $y_{TE} = 55$ mm

(l) Turbulence intensity at $y_{TE} = 55$ mm

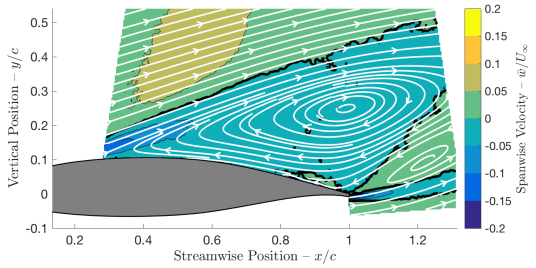
(m) $\bar{U}$ at $y_{TE} = 65$ mm

(n) Turbulence intensity at $y_{TE} = 65$ mm

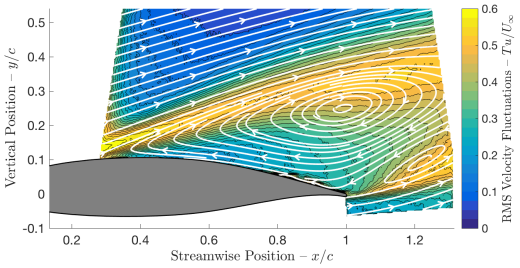
Figure 6.5: Mean velocity (a, c, e, g) and turbulence intensity (b, d, f, h) for a series of spanwise planes parallel to the trailing edge of a NASA GA(W)-1 aerofoil at $Re = 3.5 \times 10^5$ and $\alpha = 15°$.

negative across the vortex area. This vortex remains visible outside of the stall cell, at $z_s/c = 0.63$. At this position, the $w = 0$ contour is also visible however is now in an area of positive streamwise velocity. This is in agreement with the TE parallel planes presented previously.

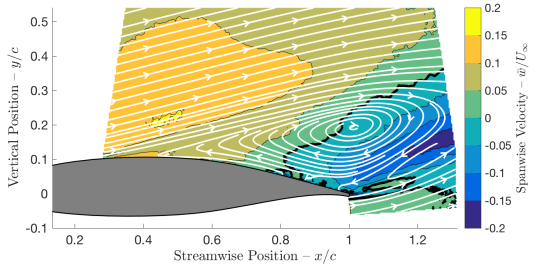
Regions of high turbulence intensity (Tu) are visible upstream of the separating streamline in all plots. As the flow moves downstream, both the area and intensity of high Tu increases. A similar increase is visible downstream of the TE vortex. These two regions merge downstream of the stall cell at $z_s/c = 0.24$ and 0.49. While the same secondary vortex is visible in $z_s/c = 0.49$ and 0.63, the intensity levels are significantly lower. Scattering from the experimental model prevented accurate measurements being made in the proximity of the aerofoil surface. This is particularly noticeable at $z_s/c = 0.24$ and 0.63.



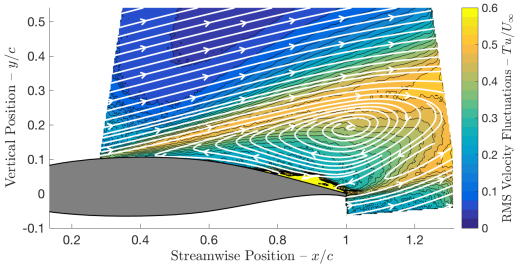
(a) w at $z_s/c = 0$ (saddle point)



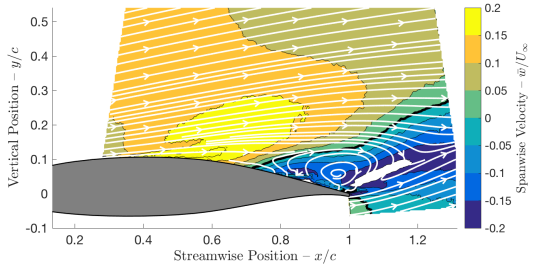
(b) Turbulence intensity at $z_s/c = 0$ (saddle point)



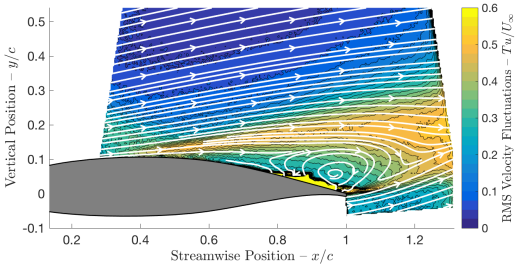
(c) w at $z_s/c = 0.24$



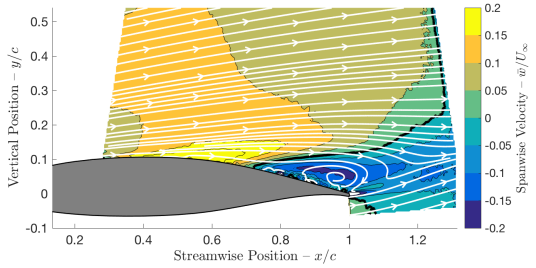
(d) Turbulence intensity at $z_s/c = 0.24$



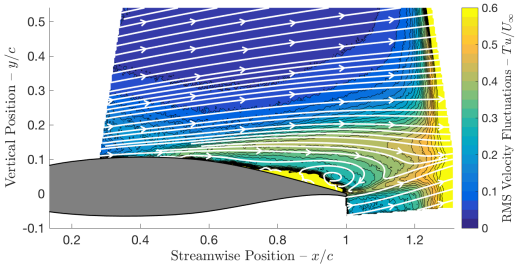
(e) w at $z_s/c = 0.49$ (focus)



(f) Turbulence intensity at $z_s/c = 0.49$ (focus)



(g) w at $z_s/c = 0.63$



(h) Turbulence intensity at $z_s/c = 0.63$

Figure 6.6: Mean spanwise velocity w (a, c, e, g) and turbulence intensity (b, d, f, h) for a series of streamwise, wall normal, planes NASA GA(W)-1 aerofoil at $Re = 3.5 \times 10^5$ and $\alpha = 15°$

. Solid black contour highlights the location of $w = 0$.

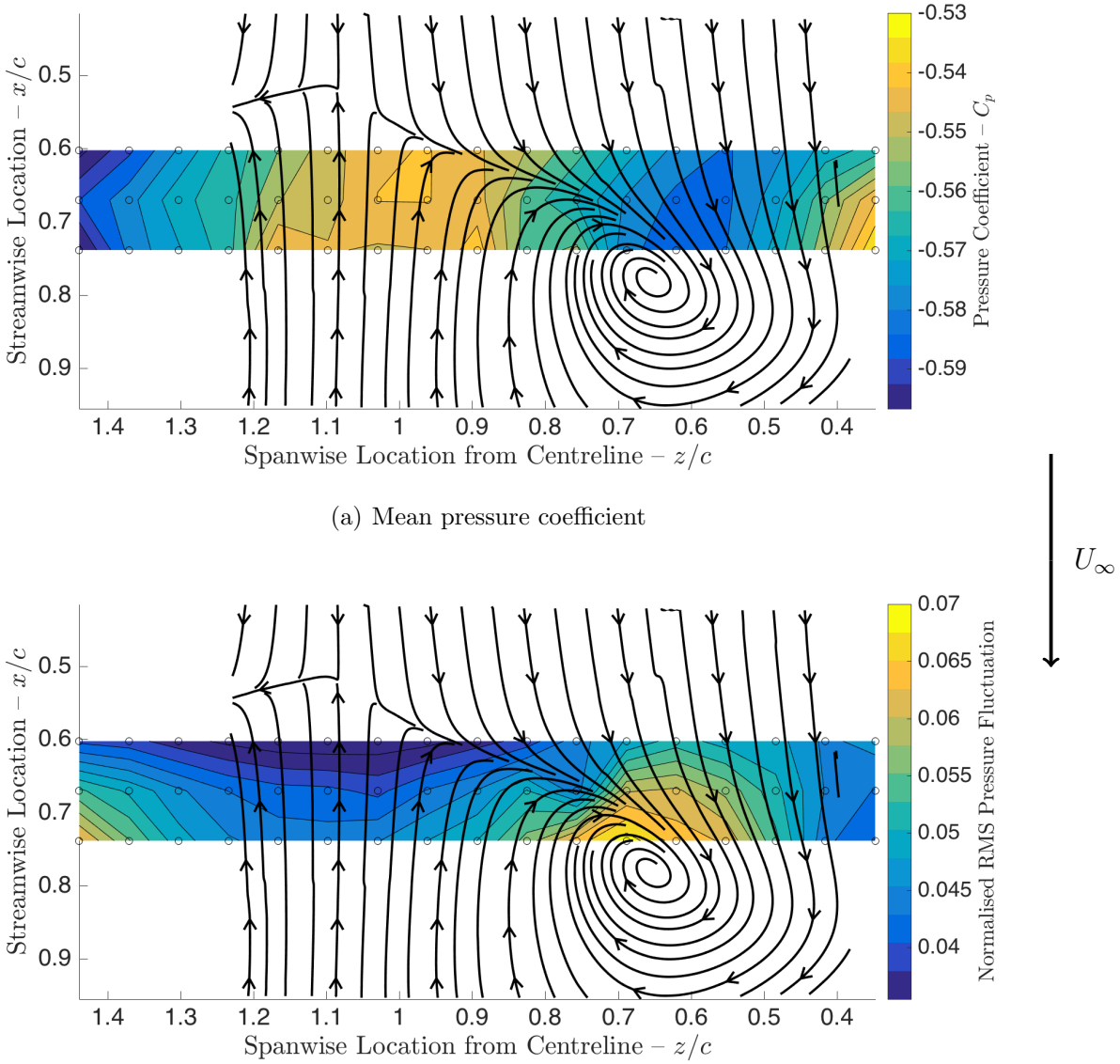
6.4 Mean Surface Pressure

A surface plot of the mean pressure coefficient is shown in Fig. 6.7(a). This data is collected from an array of surface pressure tappings spaced at 15 mm ($0.07c$) intervals at locations marked with ($\circ$). Streamlines from the previous dataset have been overlayed for spatial reference.

A spanwise variation is visible, across the stall cell identified in the PIV data, with a region of higher mean pressure towards the centre of the cell and lower pressure towards the focus located at $z/c \approx 0.65$. An additional low pressure region is visible towards the outboard edge of the array. Extrapolating from the size and topology of the cell visible in the PIV window, this is believed to be due to the second edge of the stall cell.

These data support the hypothesis of Moss and Murdin (1971), reviewed previously, who predict that areas outboard of a stall cell will remain attached longer and thus have lower pressure coefficients at downstream stations. For the purposes of stall cell detection from surface pressure measurement however, the differences are small, $\Delta C_p \approx 0.06$, in a region of unsteady flow.

The RMS of the fluctuating component of surface pressures is shown for comparison in Fig. 6.7(b). Again, a spanwise variation is visible with regions of significantly increased fluctuation levels in the region of the stall cell foci. The region immediately downstream of the saddle point shows a low level of fluctuation which increases with streamwise position.



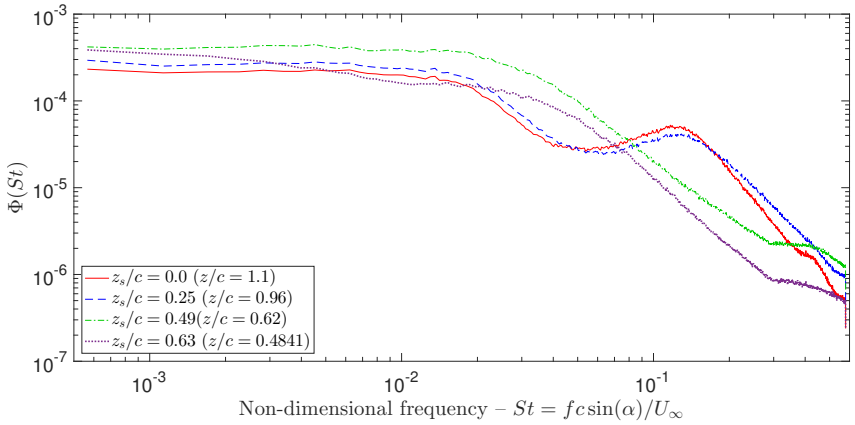
(a) Mean pressure coefficient

(b) RMS pressure fluctuaions

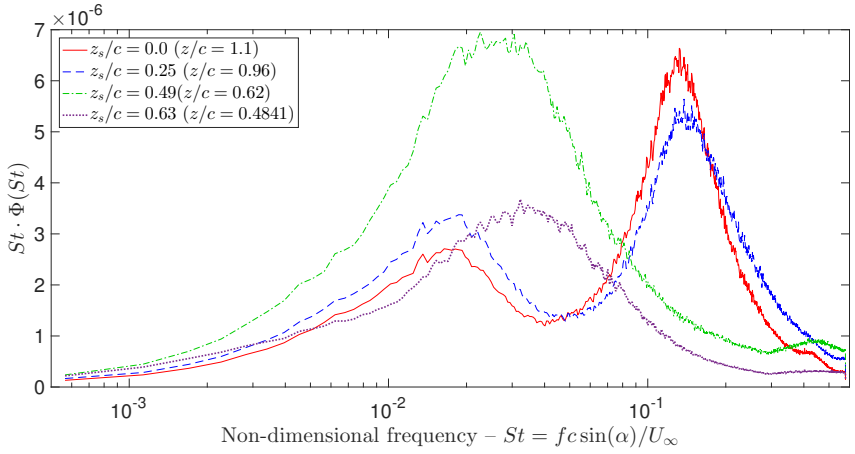
Figure 6.7: Mean surface pressure across a stall cell on a GA(W)-1 aerofoil at $\alpha = 15°$ and $Re = 3.5 \times 10^5$. Flow from top to bottom of each figure.

6.5 Frequency Distribution of Surface Pressure Fluctuations

Figure 6.8 shows the pre-multiplied energy spectra $St \cdot \Phi(St)$ distribution of surface pressure fluctuations against the corresponding Strouhal number St. Data is presented from four spanwise positions with constant chordwise location $x/c = 0.74$. The surface pressure was sampled at 500 Hz for 3600 s and is normalised by dynamic pressure.



(a) Power spectral density



(b) Pre-multiplied spectra

Figure 6.8: Surface pressure spectra from four positions across a stall cell at $Re = 3.5\times10^5$ and $\alpha = 15°$.

While the surface pressure varies little throughout the separated region, the spectral density of the fluctuating component can be seen to vary between two distinct frequency ranges. At the centre of the cell, $z_s/c = 0$ a high-energy oscillation can be seen at

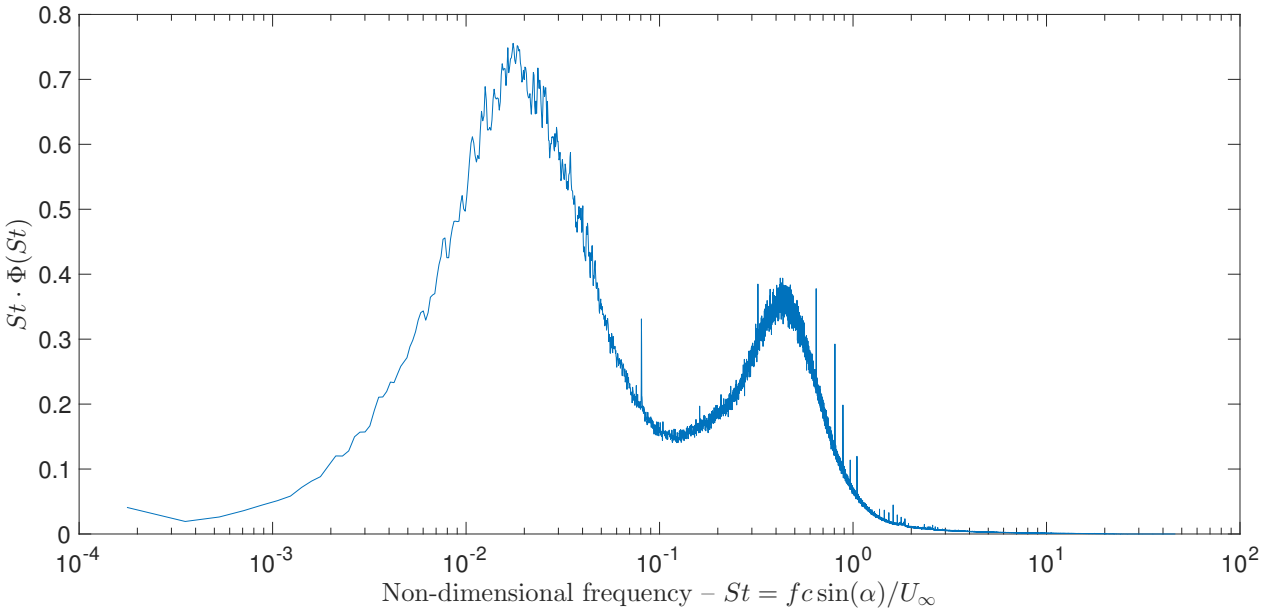


Figure 6.9: Surface pressure spectra from a high frequency transducer located near the cell boundary

frequency $St \approx 0.16$, the anticipated frequency range for von Kármán type vortex shedding. An additional oscillation is visible at a frequency an order of magnitude lower at $St \approx 0.02$, however this occurs with a significantly lower amplitude.

As the sampling location moves spanwise towards the edges of the cell, the magnitude of the peak relating to von Kármán shedding decreases in intensity while the second, lower frequency, oscillation is seen to grow. At position $z_s/c = 0.49$, the high frequency oscillation is no longer distinguishable while the low frequency signal grows significantly. Beyond the mean cell extent at position, $z_2/c = 0.63$, the overall levels of fluctuation are reduced but a broad, low-frequency, signal is still visible in the spectrum. The presence of both signals within the pressure history for signals $z_s/c = 0.0$ and 0.25 at varying amplitudes indicates that the two features are independent with varying impact, rather than a single source with a gradual change in time constant.

Figure 6.9 shows the PSD spectrum of the high frequency pressure transducer mounted in the model. The signal from this sensor is sampled at 40 kHz and is located near the boundary of the cell between the saddle and focus point. The two spectral peaks in the low frequency transducer plots previously presented are clearly visible. However there are no further features of significant energy in the remaining frequency range.

6.6 Modal Decomposition of Velocity Fluctuations

To identify the flow dynamics responsible for the surface pressure fluctuations, discussed in the previous section, the fluctuating component of a number of velocity fields will now be investigated. As the sPIV frames and pressure data are sampled at the same frequency, any features resolved by the pressure data should also be visible in the velocity data. Proper Orthogonal Decomposition (POD) is an effective method to mathematically extract spatially coherent structures from turbulent flow fields and their relative energy content (Berkooz et al., 1993). Once the coherent features have been extracted into POD modes, a linear series of coefficients can be found by projecting the POD mode back onto the original vector field. In this way a time series of the relative weights of each mode may be examined in the frequency domain.

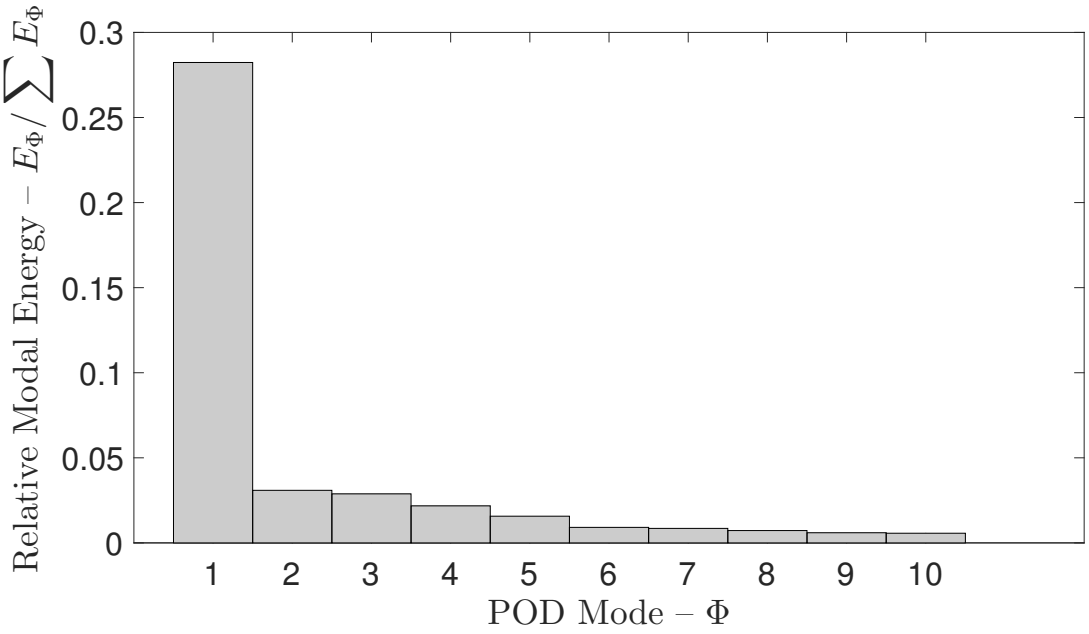
Decompositions have been conducted on three planes of importance within the flow field: two XY planes, those intersecting the saddle point and foci, and one XZ plane at $y_{TE} = 20$ mm. Each dataset consists of the normalised velocity from four unique experiments of 2734 fields per experiment. The inclusion of multiple experiments allows windowing to be used to reduce the variance of the resulting PSD. As the data are independent, no overlap is used in the windowing process as a discrete step between experiments would introduce additional error to the analysis. Due to the size of each dataset, the POD is only conducted on the in-plane velocity components. The mean velocity field is subtracted from each dataset prior to conducting the decomposition.

For each dataset, presented in Figs. 6.10 to 6.12, the relative energy content of the first 10 POD modes is shown in sub-figure (a). This is followed by the detail for the six most energetic modes. For each, the vorticity distribution of the vector field for each POD mode is shown alongside the spectral content of the POD coefficients. The streamlines corresponding to the mean flow are overlaid on the vorticity contours to provide a visual reference.

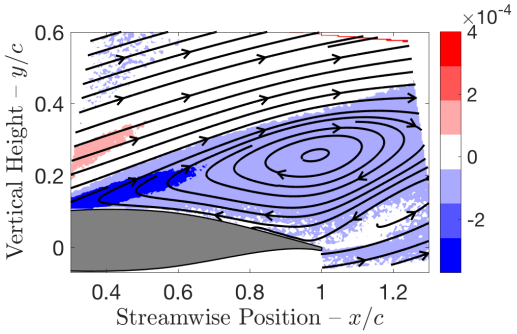
In both streamwise/wall normal planes, the most energetic modes are seen to act over the cell area. The modal coefficients relating to these large coherent variations are seen to occur at non-dimensionalised frequency $St \sim \mathcal{O}(10^{-2})$. The exception to this trend is seen in mode $m = 2$ in plane $z_s/c = 0.49$ (Fig. 6.10(e)), where a narrow spike occurs at $St \approx 10^{-1}$. The energy in this mode is located near to the trailing edge of the aerofoil. Examination of the source images indicates that this is due to a fluctuating reflection of the laser sheet from the wing surface.

The energy content for the remaining modes is concentrated at higher frequencies with $St \sim \mathcal{O}(10^{-1})$. The vector fields forming these modes contain coherent concentrations of vorticity with alternating sign which are significantly smaller than the mean stall cell. These are arranged along the shear layer separating the mean recirculating region and the free-stream. These structures are typical of von Kármán shedding from bluff body wakes and occur in the frequency range observed by previous authors.

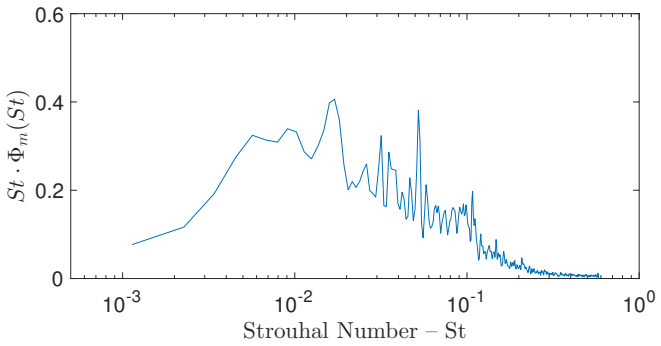
The decomposition of the wall parallel plane, at $y_{TE} = 20$ mm, again demonstrates a similar pattern. The most energetic modes show a consistent alteration of the stall cell. The changes in these modes are concentrated near the streamline forming the boundary of the stall cell. The energy content of the modal coefficients of these large scale variations again occurs at $St \sim \mathcal{O}(10^{-2})$. In modes $m = 4$ and 6, smaller structures with alternate directions of vorticity are visible around the mean boundary of the stall cell. These occur with higher frequencies and appear to relate to the von Kármán shedding visible in the streamwise/wall normal planes.



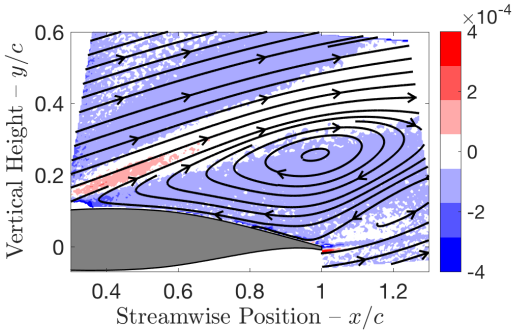
(a) Relative energy content of the first 10 POD modes



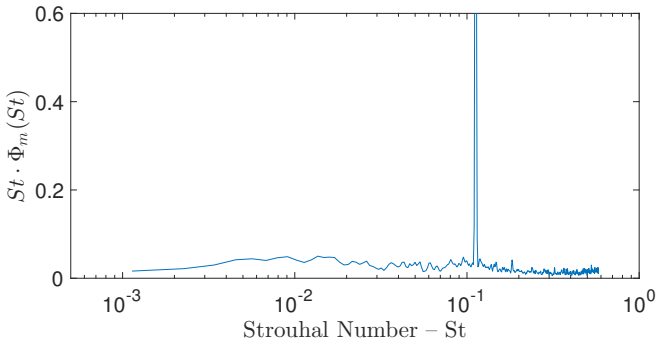
(b) Vorticity distribution $m = 1$



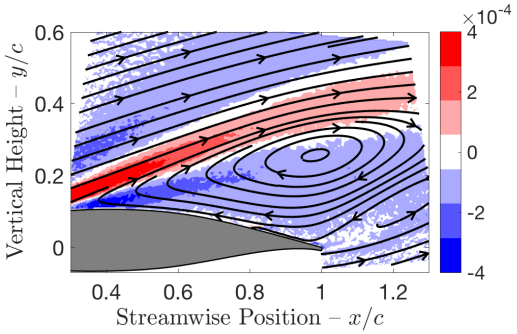
(c) Frequency distribution $m = 1$



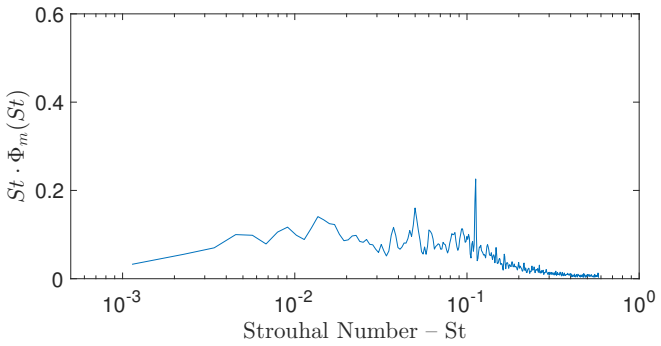
(d) Vorticity distribution $m = 2$



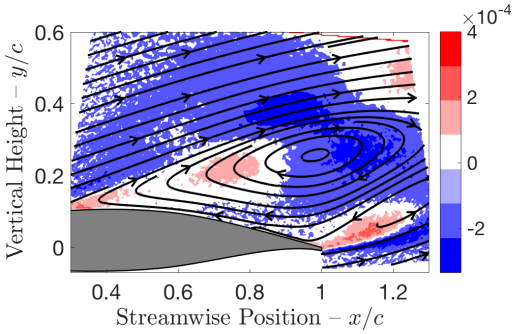
(e) Frequency distribution $m = 2$



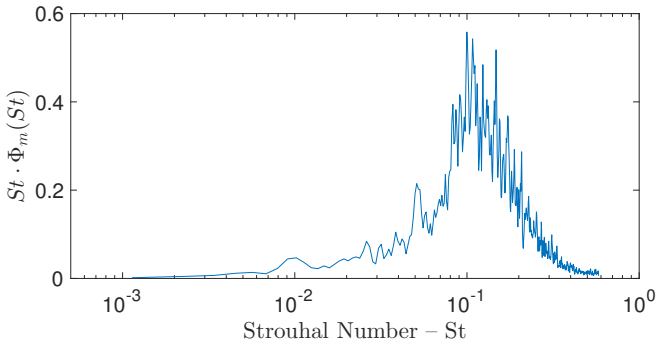
(f) Vorticity distribution $m = 3$



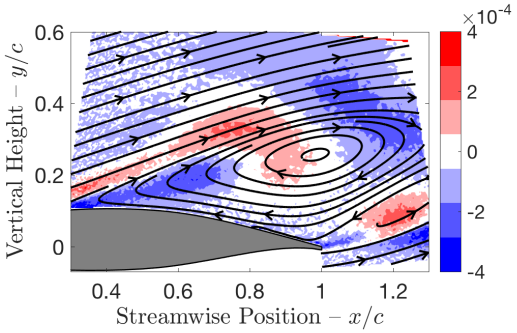
(g) Frequency distribution $m = 3$



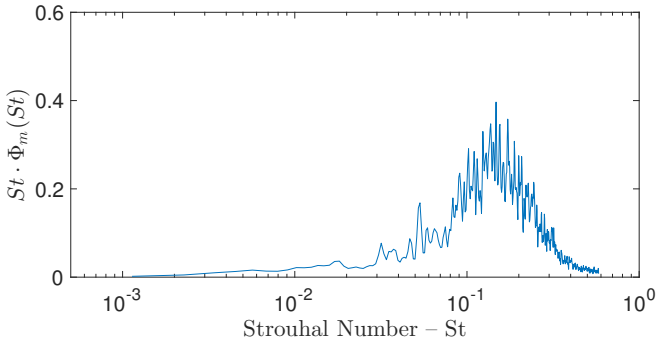
(h) Vorticity distribution $m = 4$



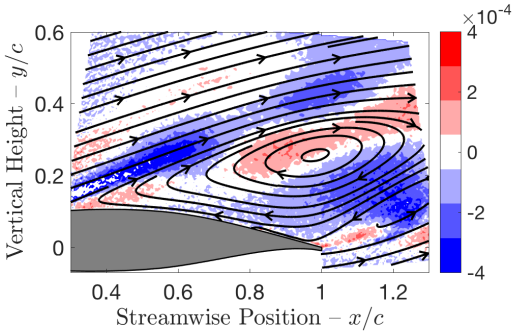
(i) Frequency distribution $m = 4$



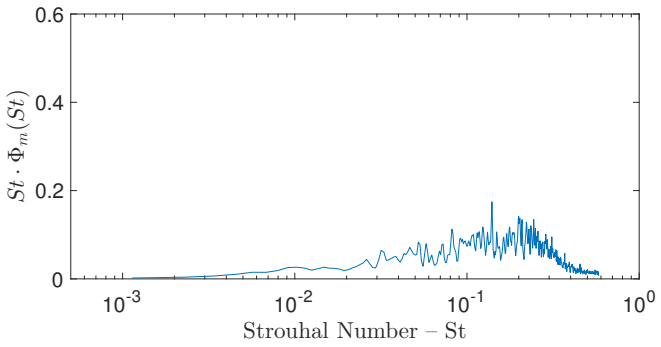
(j) Vorticity distribution $m = 5$



(k) Frequency distribution $m = 5$

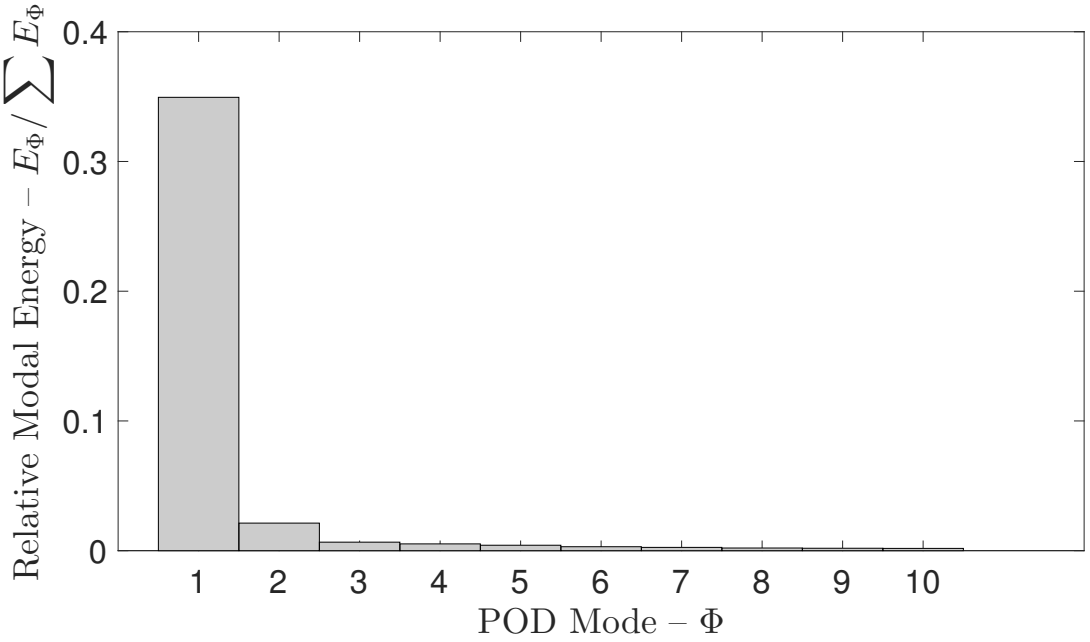


(l) Vorticity distribution $m = 6$

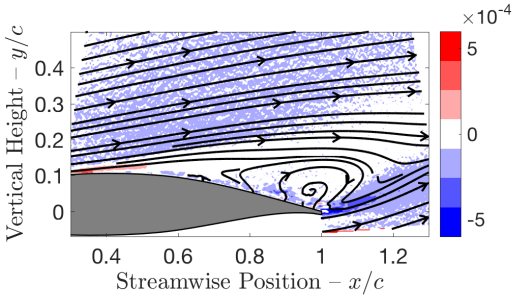


(m) Frequency distribution $m = 6$

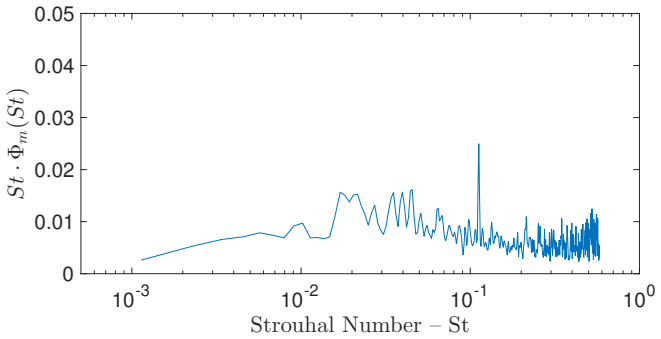
Figure 6.10: POD Modes for streamwise × wall normal plane at $z_s/c = 0$



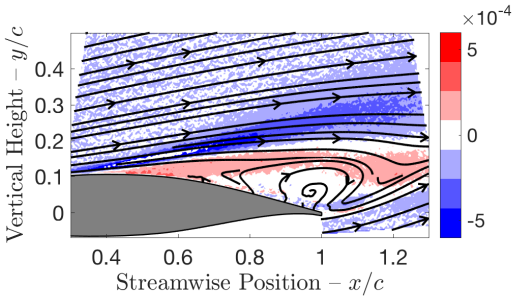
(a) Relative energy content of the first 10 POD modes



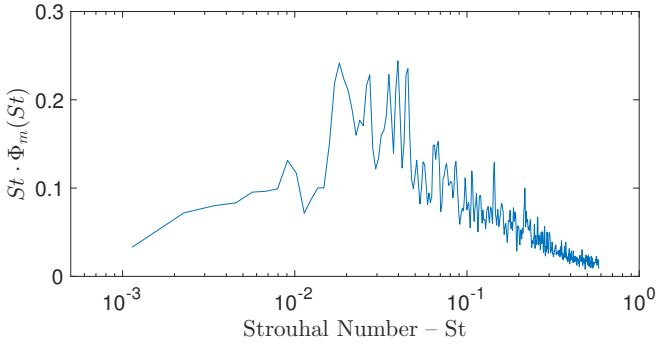
(b) Vorticity distribution $m = 1$



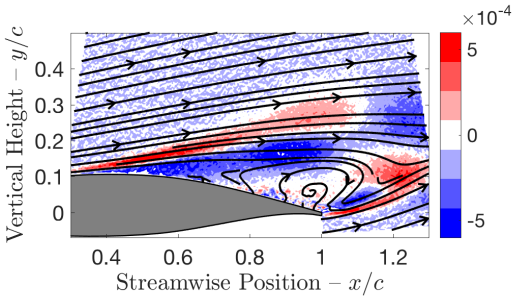
(c) Frequency distribution $m = 1$



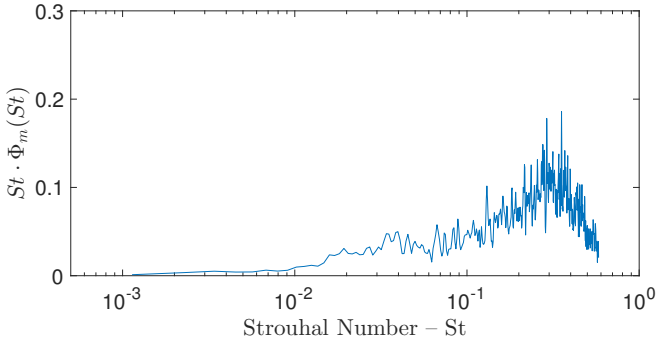
(d) Vorticity distribution $m = 2$



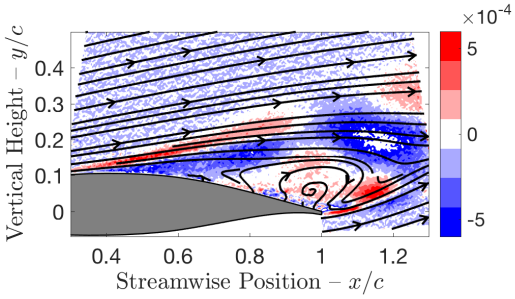
(e) Frequency distribution $m = 2$



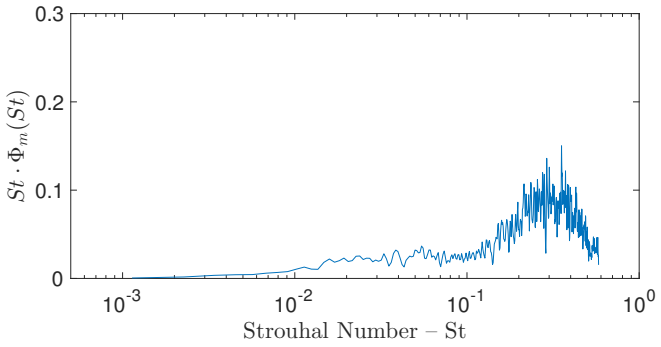
(f) Vorticity distribution $m = 3$



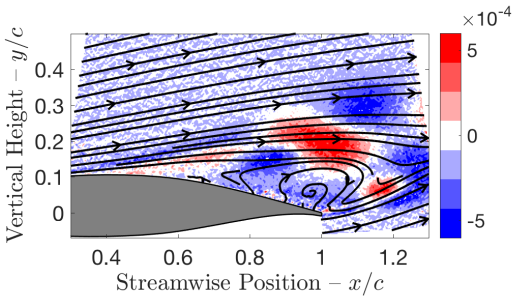
(g) Frequency distribution $m = 3$



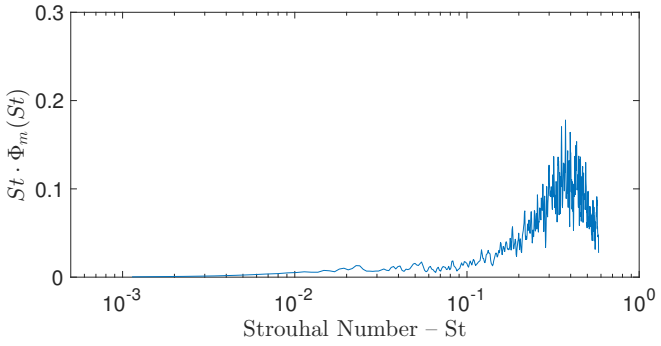
(h) Vorticity distribution $m = 4$



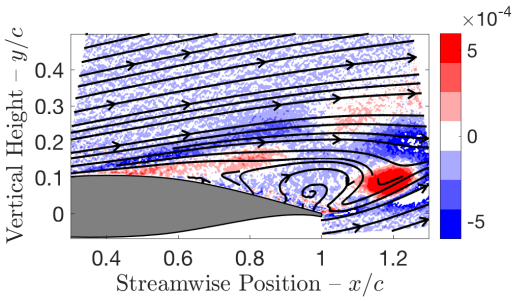
(i) Frequency distribution $m = 4$



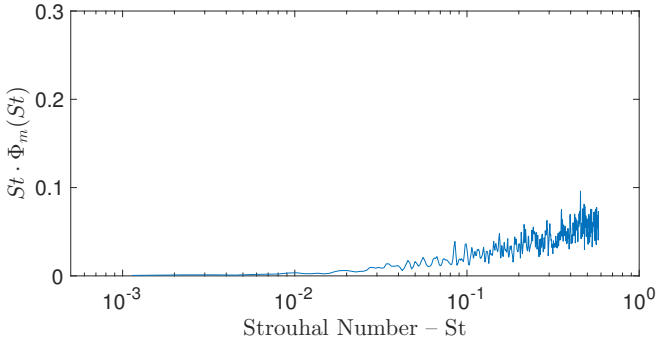
(j) Vorticity distribution $m = 5$



(k) Frequency distribution $m = 5$

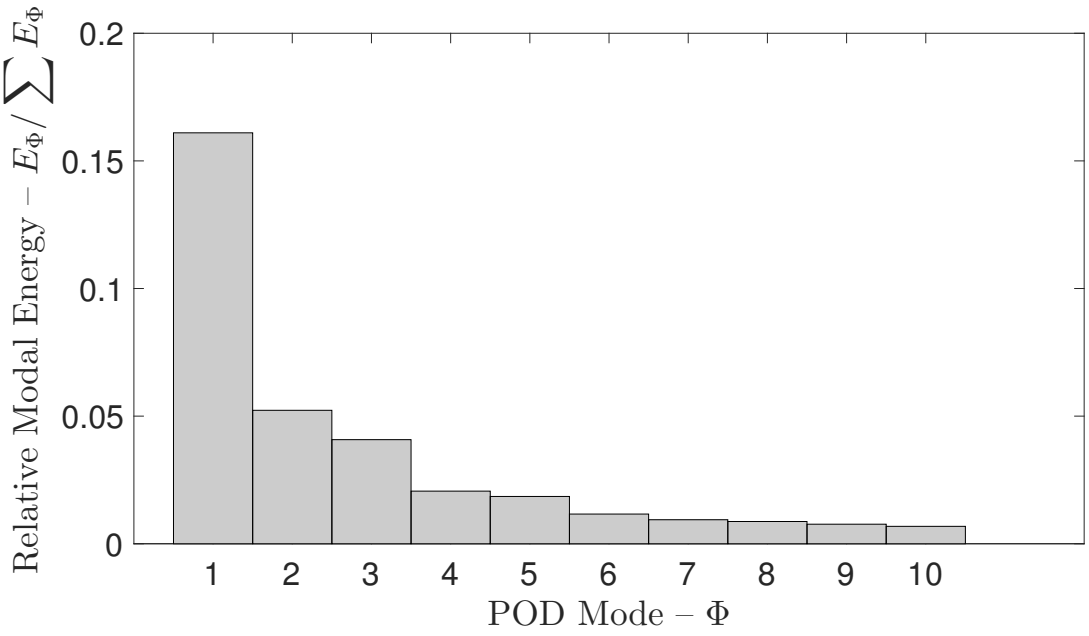


(l) Vorticity distribution $m = 6$

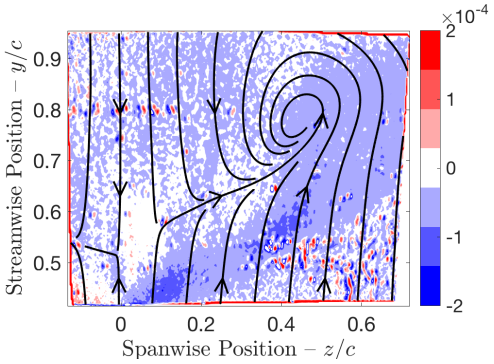


(m) Frequency distribution $m = 6$

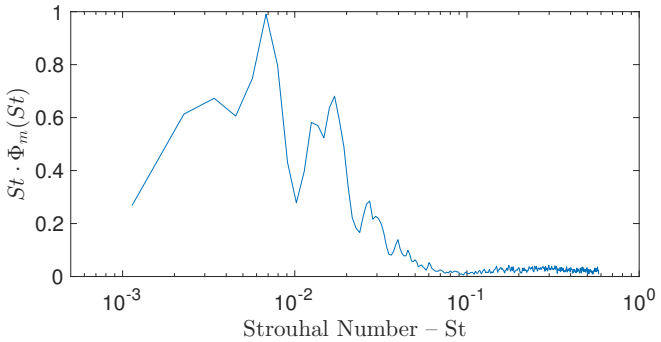
Figure 6.11: POD Modes for streamwise × wall normal plane at $z_s/c = 0.49$



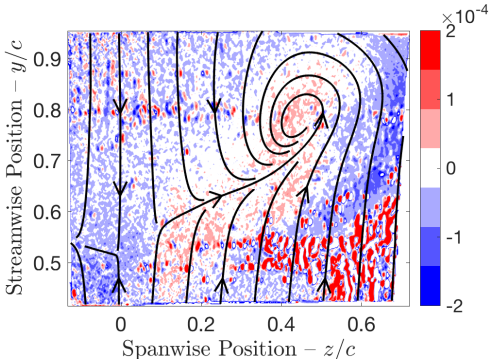
(a) Relative energy content of the first 10 POD modes



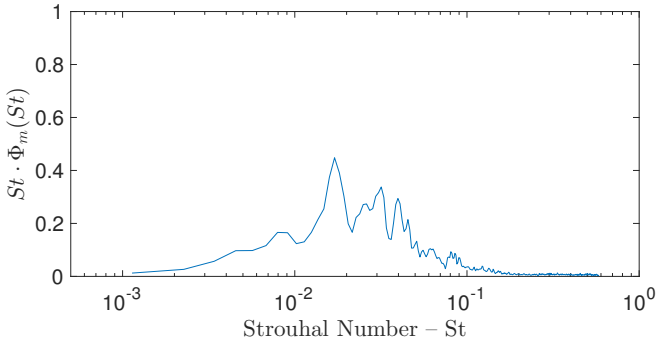
(b) Vorticity distribution $m = 1$



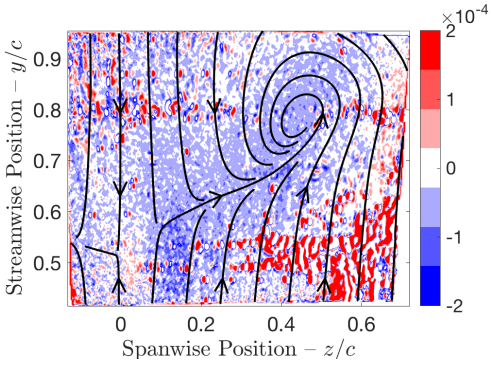
(c) Frequency distribution $m = 1$



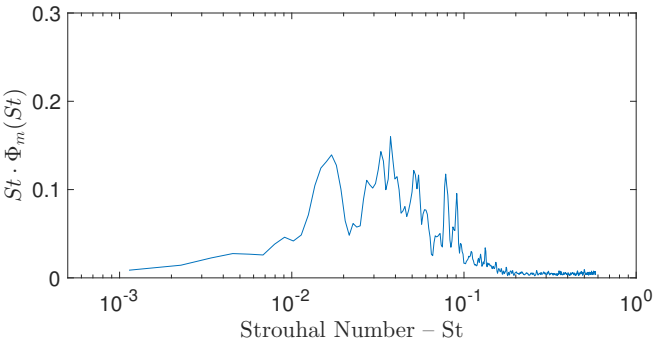
(d) Vorticity distribution $m = 2$



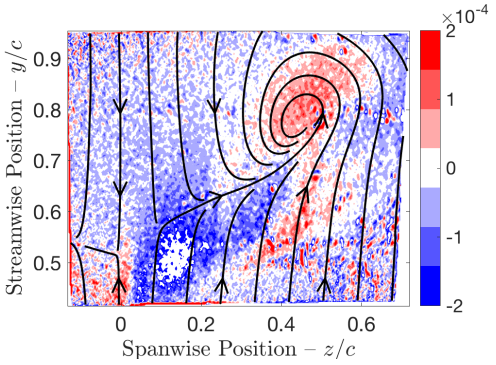
(e) Frequency distribution $m = 2$



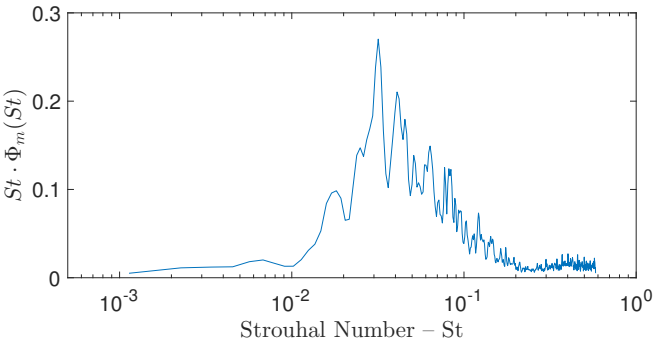
(f) Vorticity distribution $m = 3$



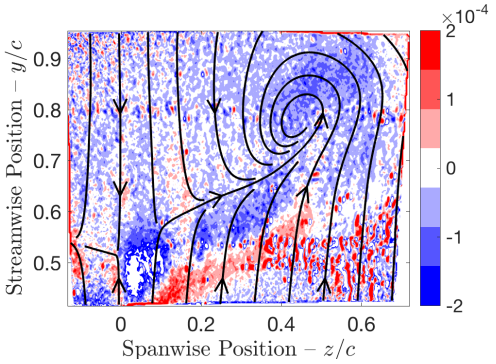
(g) Frequency distribution $m = 3$



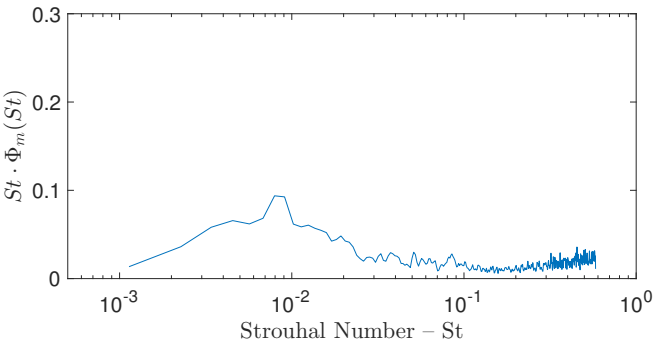
(h) Vorticity distribution $m = 4$



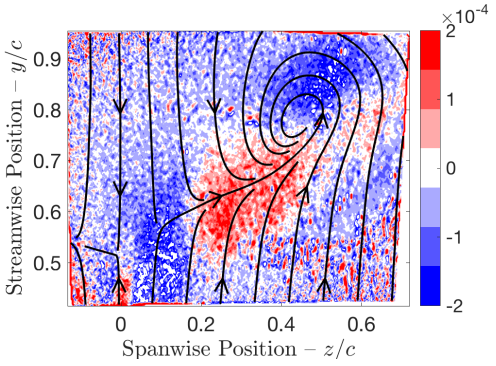
(i) Frequency distribution $m = 4$



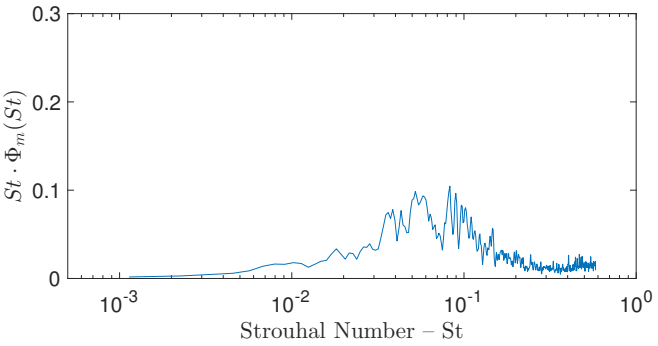
(j) Vorticity distribution $m = 5$



(k) Frequency distribution $m = 5$



(l) Vorticity distribution $m = 6$



(m) Frequency distribution $m = 6$

Figure 6.12: POD Modes of the wall-parallel plane at $y_{TE} = 20$ mm

The noise in the vector fields visible in the mean flow fields presented previously is particularly noticeable in the wall parallel decomposition. These regions are small, however do act as a source of error in these images.

6.7 Discussion

The partially separated flow topology of the NASA GA(W)-1 aerofoil, and its spatial evolution away from the model has been investigated. Initially, surface oil flow visualisation was conducted to confirm the predicted spanwise periodic distribution of stall cells on the wind tunnel model. Conditions of $Re = 3.5 \times 10^5$ and incidence $\alpha = 15°$ were selected due to the presence of a single, stable, pattern of stall cells of appropriate size for the measurement apparatus. Mean and time-resolved data were presented and these will now be discussed separately.

6.7.1 Mean Flow

The mean and fluctuating components of the flow fields from two sets of perpendicular sPIV planes, one spanwise, parallel to the model trailing edge, and the other in the streamwise/wall normal direction, were presented to establish the time-averaged flow topology. The wall parallel data cover approximately two-thirds of a stall cell and show the characteristic 'mushroom' topology, described by previous authors. A 3D separation region is shown, bounded in the visible region by a vortex with focus at $x/c \approx 0.7$ and $z_s/c = 0.49$. At stations further from the model, the bounding vortex is seen to move downstream and towards the centre of the cell.

Examination of the streamwise/wall normal planes identifies a single pair of counter-rotating, spanwise, vortices in all frames. These are referred to as the Separation Line Vortex (SLV) and Trailing Edge Line Vortex (TELV) by Manolesos and Voutsinas (2015). The SLV is located above the suction surface of the aerofoil and, in the data presented as part of this thesis, has constant spanwise position of $x/c \approx 1.0$.

The height and strength of the SLV varies with spanwise position within the cell. At the centre of the cell the vortex centre has height $y/c = 0.25$ above the aerofoil and this decreases with spanwise position. At the spanwise location at which the focus is identified in the wall parallel planes, the SLV remains visible at $x/c \approx 1.0$. The $w = 0$ contour,

found within a strong spanwise velocity gradient and negligible streamwise velocity such as is anticipated through a wall normal vortex, is also visible and distinct at $x/c \approx 0.7$.

The existence of both features, distinct from each other, within the same mean flow field is contrary to the original model proposed by Weihs and Katz (1983). Instead, these data support the model more recently proposed by Manolesos and Voutsinas (2015) in which the SLV and TELV are distorted by the amplification of an initial 3D perturbation by a Crow-type instability of the vortex cores. Instead of splitting to form independent ring vortices as Weihs and Katz suggest, the instability induces two secondary, counter-rotating, vortices which intersect the wing surface.

Contour plots of turbulence intensity show that high levels of fluctuations exist around both the upper and lower separating streamlines. These disturbances continue into the wake and correspond well with the reports of 'flapping' of the separation bubble of Zaman et al. (1989). Despite similar sizes of SLV at $z_s/c = 0.49$ (focus) and 0.63 (outside the cell) the intensity of fluctuations decreases outside of the stall cell limit.

6.7.2 Unsteady Flow

Analysis of the energy content of the fluctuating surface pressure signals in the frequency domain shows a variation in characteristic frequency across the span of the stall cell. Towards the centre of the cell a spectral peak is visible in the fluctuations at non-dimensional frequency $St \approx 0.2$. A smaller, but defined, peak is also visible at $St \approx 0.02$.

At the spanwise location of the identified focus, the high frequency fluctuations are no longer visible in the pressure spectra and the low frequency oscillations are instead seen to dominate. At a mid-station between the saddle and focus points, the relative energy content is seen to change between the high and low frequency components. The energy contained in the $St \approx 0.2$ fluctuation decreases while the energy in the $St \approx 0.02$ increases. Outboard of the recorded cell bounds, the low frequency variation remains visible, however it is at a lower intensity.

Proper Orthogonal Decomposition (POD) was used to extract spatially coherent structures from the time dependent flow. This was conducted at two spanwise locations and one plane parallel to the model trailing edge. Two distinct types of fluctuations were observed in the decomposed datasets. The most energetic modes in both streamwise/wall

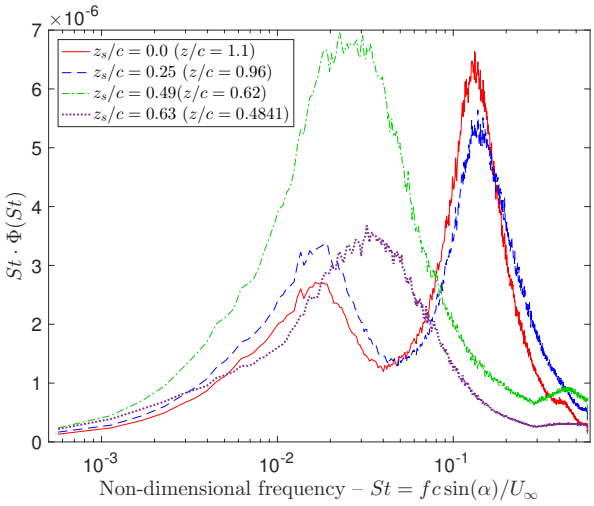
normal planes were an alteration in vorticity across the recirculating region. Fourier decomposition of the POD mode coefficients shows that these large modes occur with a frequency around $St \approx 0.02$. Fluctuations in wing loading have been reported previously by authors studying the near-stall characteristics of high-lift aerofoils since Jones (1934). Investigation of smoke patterns by Zaman et al. (1989) concluded that these oscillations were due to a vertical flapping of the separated region caused by background tunnel fluctuations.

Smaller structures, with alternating sign of vorticity, are observed with lower relative energy content. These structures are clustered around the upstream and downstream separating shear layers. Frequency analysis of the modal coefficients shows that these structures occur at $St \approx 0.2$, an order of magnitude higher than that associated with the larger structures. The combination these properties match the canonical description of the anticipated bluff-body shedding.

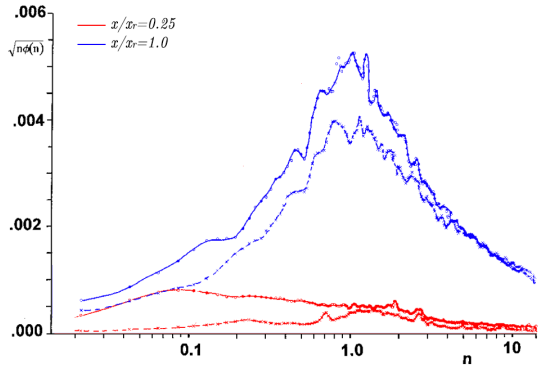
The most energetic POD modes from the spanwise/wall parallel plane show the cell to vary in spanwise size at the same frequency as the vertical growth in the recirculating region. This is previously unreported and, in combination with the surface pressure measurements presented, provides an alternate explanation for the low-frequency oscillations in lift previously reported in the literature.

Low-frequency periodic 'pumping' of separation regions has been reported previously in a range of separated flows and these are compared in Fig. 6.13. The periodic growth and reduction of the separation bubble behind a backward facing step is described by Eaton and Johnston (1982) and Heenan and Morrison (1998) (Fig. 6.13(b)). The same phenomenon is seen on an axisymmetric model by Oxlade (2013) and Rigas et al. (2014) (Fig. 6.13(c)) and on an Ahmed body by Cabitza (2014). A similar variation in the frequency of fluctuations in pressure spectra are also observed around the shock foot in unsteady shock-wave boundary layer interactions (Dussauge et al., 2006) as shown in Fig. 6.13(d). Although the characteristic non-dimensional frequency varies in each of these cases, it is always approximately one order-of-magnitude lower than that associated with the shear layer instability. It is therefore deduced that the variation lies in the characteristic length which is used for normalisation.

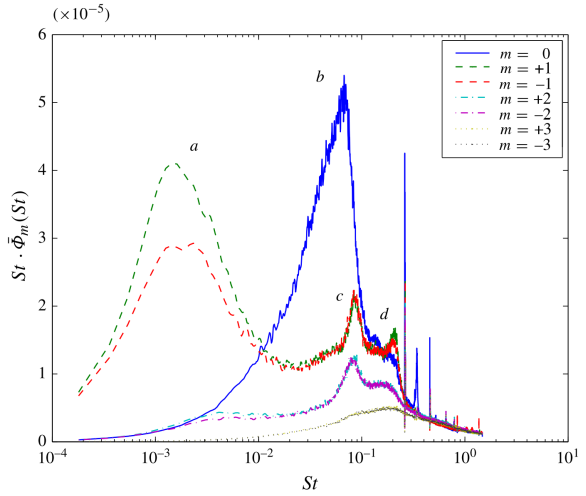
A key difference between the previous examples of separation bubble pumping and that presented in this work is the location of the separation point or line. In each of the examples described, the flow separates from a sharp, defined edge and the pumping



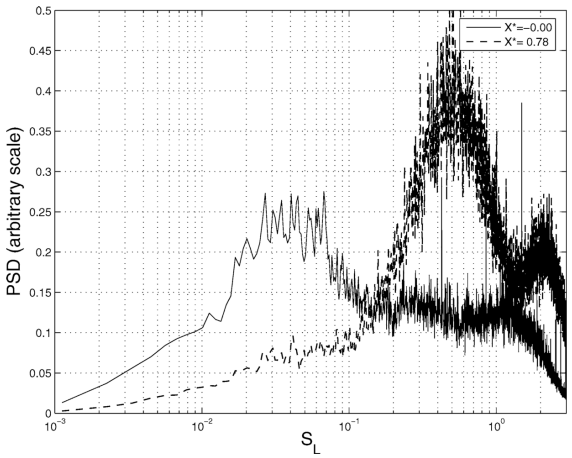
(a) Spectra of pressure fluctuations from the current work. $z_s/c = 0.0$ lies at the centre of the stall cell and $z_s/c = 0.49$ corrosponds to the edge of the separated region.



(b) Spectra of pressure fluctuations behind a backward facing step. x_r is the streamwise coordinate of the reatachment point (Heenan and Morrison, 1998).



(c) Specra of POD modes of the pressure fluctuations behind an axisymetric bluff body (Oxlade, 2013). The labeled peaks indicate: b – the bubble pumping mode, and d – the vortex shedding dynamic.



(d) Spectra of pressure fluctuations at the shock foot ($X^* = 0$) and interaction zone ($X^* = 0.8$) of a shock wave/boundary layer interaction at freestream Mach 2.3 (Dussauge et al., 2006)

Figure 6.13: Comparison of frequency distribution of pressure fluctuations from within separating regions across a range of flows.

alters the downstream pressure recovery and so the model base pressure. In the case of an aerofoil however, the boundary layer separates from a surface with continuous curvature. The location or topology of the separation line is therefore not known *a priori* but instead is a function of the upstream boundary layer momentum and the adverse pressure gradient.

The vertical change in the separation bubble, observed in this experiment and previously by Zaman et al. (1989), alters the streamwise separation point at any given spanwise location of the cell. This alters the path of the inviscid free-stream around the aerofoil and thus the pressure in the recirculating region. This change is, however, small compared to the local mean pressure and the oscillations caused by the periodic roll-up and shedding of the separation bubble. In their work on a backward-facing step, the maximum RMS surface pressure fluctuations observed by Heenan and Morrison (1998) correspond with the mean reattachment point of the separation bubble. This occurs because, at this point of mean reattachment, the pumping separation bubble causes periodic switching between attached and separated flow. In this work, the spanwise enlargement and contraction of the separated region causes a similar variation in surface pressures, however this time around the edge of the cell. It is therefore concluded that this large fluctuation in pressure over a moderate area of the aerofoil is a significant cause of the variable wing loading previously reported in this frequency range.

For these experiments, background readings of pressure and velocity fluctuations have been recorded in Sec. 6.1.1. These readings, taken at $f = 40$ kHz using a piezoresistive microphone and hot-wire anemometer respectively, show that the only significant background fluctuation in the frequency range of interest occurs at $St \approx 0.08$. This corresponds with the blade passing frequency of the wind tunnel drive and is distinct from either of the modes presented above. The pressure signal from the high frequency Endevco sensor located near the cell boundary, between the saddle and focus points, is used to demonstrate that no higher frequency components are aliased onto the lower frequency transducers. It has therefore been shown that there is no evidence to presume that either fluctuation is due to the background tunnel flow.

Chapter 7

Point Actuation

7.1 Introduction

In the previous two chapters, the methodology for the design of an adaptive vortex generator, and a study on the topology and behaviour of separation from a turbulent aerofoil have been presented. In this chapter, these two approaches are incorporated to produce an adaptive separation control device from the initially curved surface found towards the leading edge of an aerofoil. Knowledge of the streamline topology is used to position the actuator to provide a control with large spanwise extent from a single source. This is tested initially with the application of a static VG upstream of the identified location in Sec. 7.2. An adaptive device is developed to replace the static VG on the aerofoil by applying the technique from Chapter 5 to an initially-curved surface in Sec. 7.3. The adaptive device is then fitted to the model and the resulting flow fields are compared in Sec. 7.4.

7.2 Actuator Placement

Vortex generators are traditionally applied in an equi-spaced line over the span of an aerofoil in locations which are necessary for safe flight. This approach assumes the existence of a constant 2D separation line along the wing.

The presence of the periodic quasi-steady 3D structures observed in Chap. 6 and recorded by those authors reviewed in Sec. 2.1.3 indicates that a non-uniform approach may be

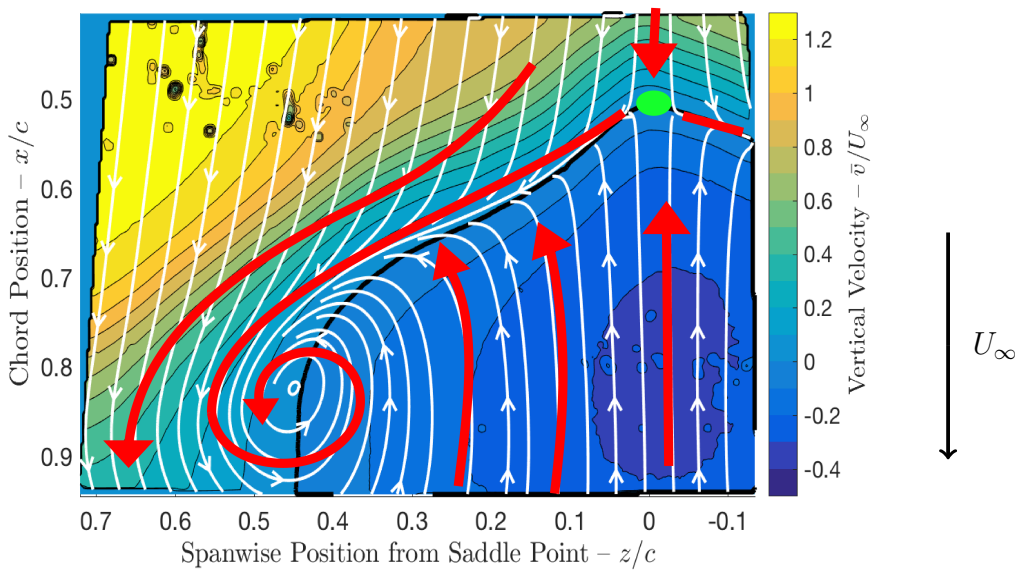


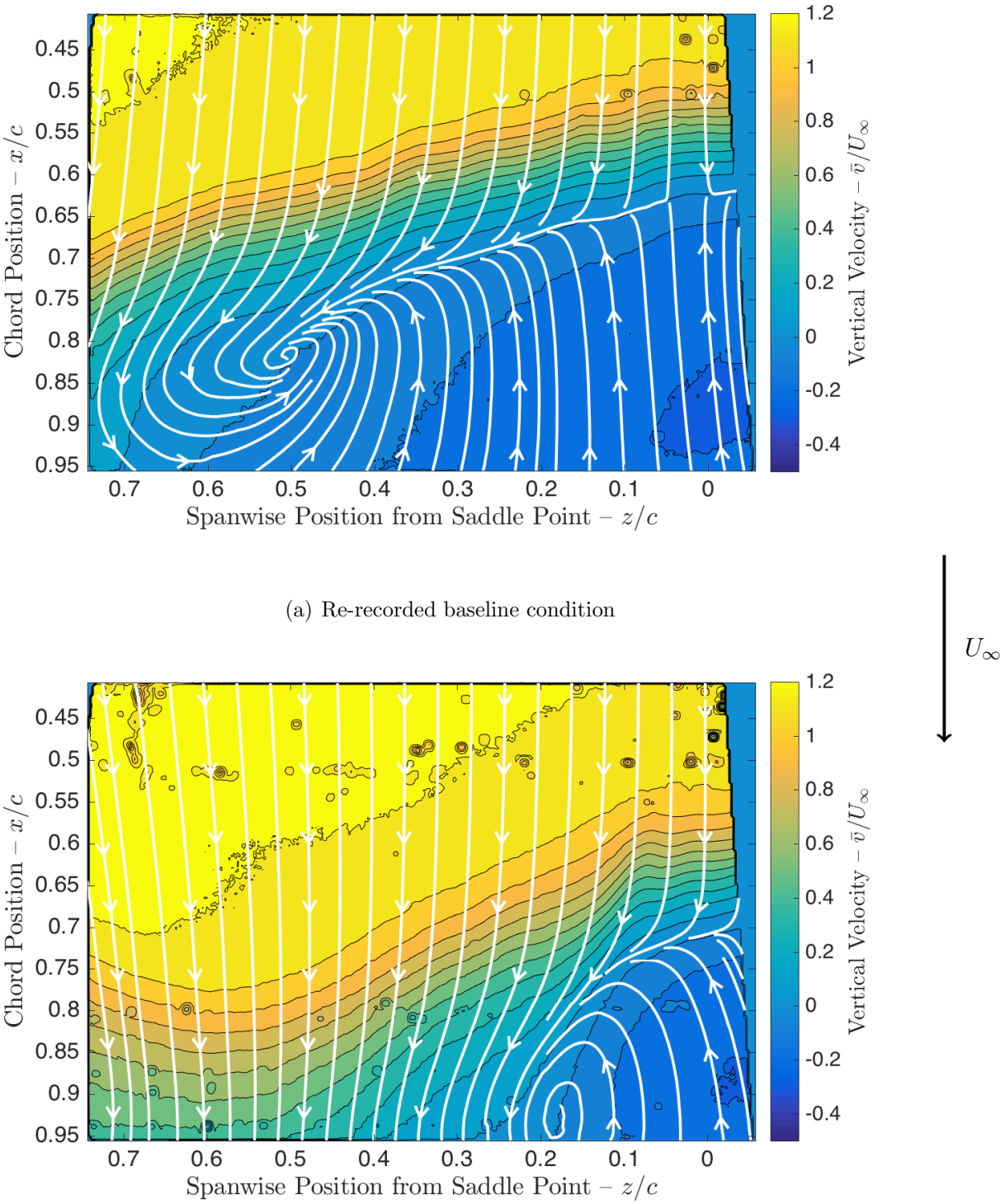
Figure 7.1: Convection of information along streamlines within a stall cell. The bifurcating saddle point is marked with (•).

effective.

The streamlines observed in the mean flow represent the convection of information through the flow field. At the saddle point, located on the fluid boundary at the upstream centre of the cell, the flow bifurcates to form the separating stream-surface which divides the freestream from the recirculating flow. Any alteration in the properties of the fluid on this streamline should therefore propagate around the cell (Fig. 7.1).

The discontinuous forwards wedge VG examined in Sec. 5.1 was applied to the aerofoil upstream of a saddle point at $x/c = 0.3$. The experiment conducted in Chap. 6 was repeated for the XZ plane $y_{TE} = 20$ mm from the aerofoil trailing edge. The baseline case was repeated for this experiment to ensure that any change between different experimental sessions was captured and a direct comparison can therefore be made. The resulting mean flow is shown in Fig. 7.2.

The recirculating region can be seen to reduce in size significantly following the application of the vortex generator. The upstream extent of the separation bubble retreats $\approx 0.07c$ however the spanwise extent is most significantly affected and, the distance between the saddle and focus visible in the PIV data, can be seen to contract by $\approx 60\%$ or $z/c \approx 0.32$.



(a) Re-recorded baseline condition

(b) After application of a static VG at $x/c = 0.3$ and $z_s/c = 0$

Figure 7.2: Flow field before and after application of a discrete VG to the wing

7.3 Adaptive Device Design

The methodology presented in Sec. 5.2 is used to evaluate the optimal values of design parameters for this new case. However, the constituent processes must be updated to adequately capture the more complex flow. The flow over an aerofoil section has two distinctions from the plate condition previously described, the adverse pressure gradient present over the device, and the initial streamwise curvature of the adaptive section.

The adaptive domain has the same surface dimensions as that used in the previous chapter, however in this case the model must be deformed to the initial shape prior to actuation. The curvature of the aerofoil section is small however, while the bending response is anticipated to be linear, the deformation is calculated considering geometric nonlinearity. This ensures compatibility of the solution for the subsequent out-of-plane deformation, applied following the initial step. This is where the equilibrium solution of minimum strain energy requires the 'unbending' of the initially curved surface to reduce overall material elongation while still meeting the boundary conditions in the membrane hypothesis (Calladine, 1983). After the surface is the correct initial shape, it is then deformed with an perpendicular actuation as before and the resulting geometry is mapped for use in the CFD.

In order to design the optimal device for this case, the surface pressure gradient must be calculated accurately within the CFD simulation. The LES model used previously is therefore updated to include the aerofoil geometry inside a structured polar mesh. A polar mesh is used as it allows a more uniform expansion of cells away from the wall as x spacing increases with y. The near-wall mesh spacings are maintained from those described previously.

The cell boundaries are perpendicular to both the aerofoil surface and the outer domain and transition smoothly between these two surfaces. The outer boundary is circular and has radius $r = 3c$ centred about the aerofoil mid-point and the spanwise domain extent is $z = \pm 0.05$ m. The boundary is separated into two semicircular elements for the inlet and outlet boundary conditions and are split at the tangents to the incident flow as shown in Fig. 7.3.

The shape factor is calculated at the same downstream locations as in Sec. 5.2, however the vertical integration must now accommodate the potential for reversed flow $u(y) < 0$

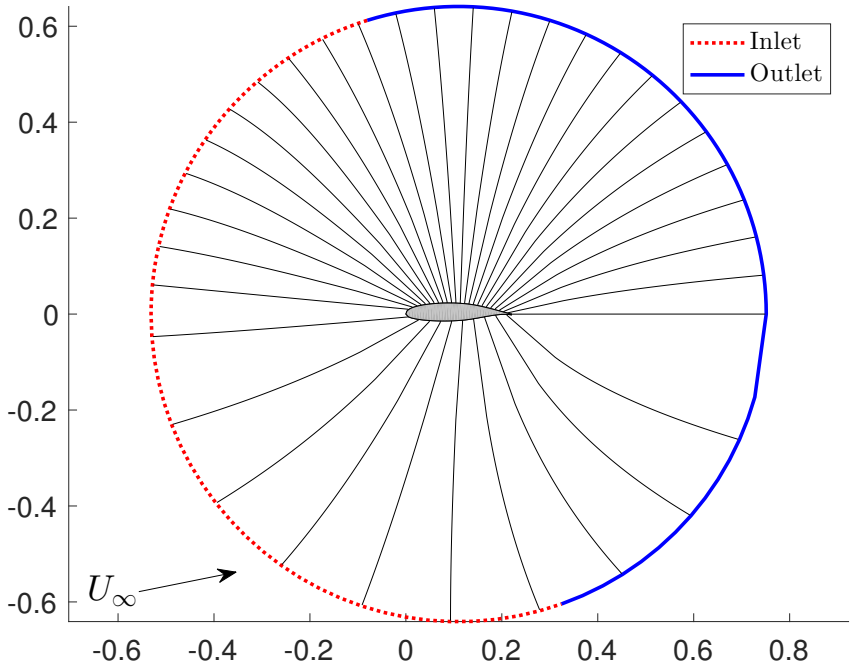


Figure 7.3: Polar mesh grid topology. Only one in four grid guidelines shown for clarity.

which, in Eq. 2.4, would reduce the momentum thickness. The equation for θ is therefore modified to

$$\theta = \int_0^\delta \left| \frac{u(y)}{U_e} \right| \left(1 - \frac{u(y)}{U_e} \right) dy \tag{7.1}$$

which behaves as anticipated.

The optimisation was conducted for four iterations and checked for convergence. The change of the objective function and peak stress is shown in Fig. 7.4. H is seen to decrease over the first two iterations followed by limited improvement over subsequent steps. As in the plate experiment, when using a lattice-based surface the peak stress constraint is not reached and so the final geometry is achieved within elastic limits. The final design parameters are shown in Tab. 7.1. The metallic lattice geometry was micro-machined and encapsulated following the same method used in Sec. 5.5. The lattice was then attached to a 3D printed support to produce the correct initial curvature and mounting locations for inclusion in the wind tunnel model. An example of an assembled device is shown in Fig. 7.5(a).

The deformed geometry was validated against the shape predicted by the FE analysis using the scanning process described in Sec. 5.5. Comparison between the physical and calculated geometry are shown for the mid-plane section through the actuation point in

Description	Symbol	Final Value
Spar Length (mm)	ℓ	10.0
Core Radius (ratio)	r/ℓ	0.121
Boundary Vertex (mm)	x_1	103.3
Boundary Vertex (mm)	z_1	38.0
Boundary Vertex (mm)	x_2	19.0
Boundary Vertex (mm)	z_2	45.14
Actuation Location Parameter	P_A	0.727
Actuation Height (mm)	y_A	2.64

Table 7.1: Lattice design parameters and their constraints for decreasing the boundary layer shape factor over an aerofoil section

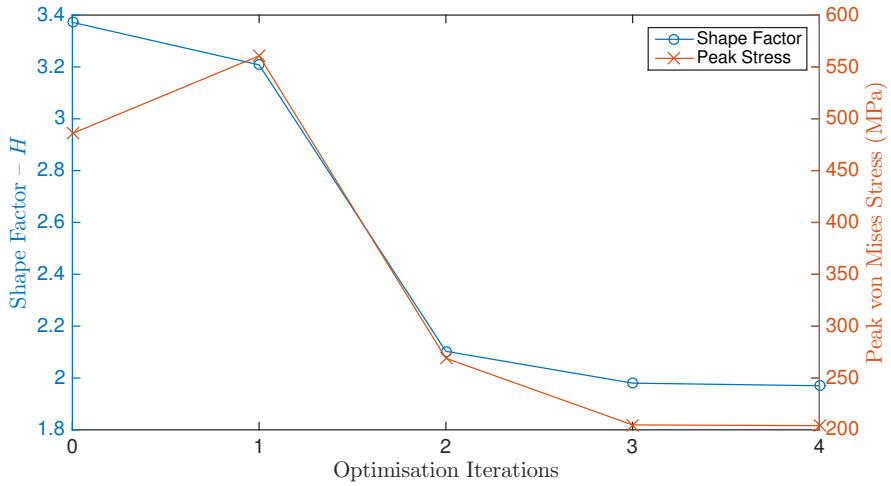
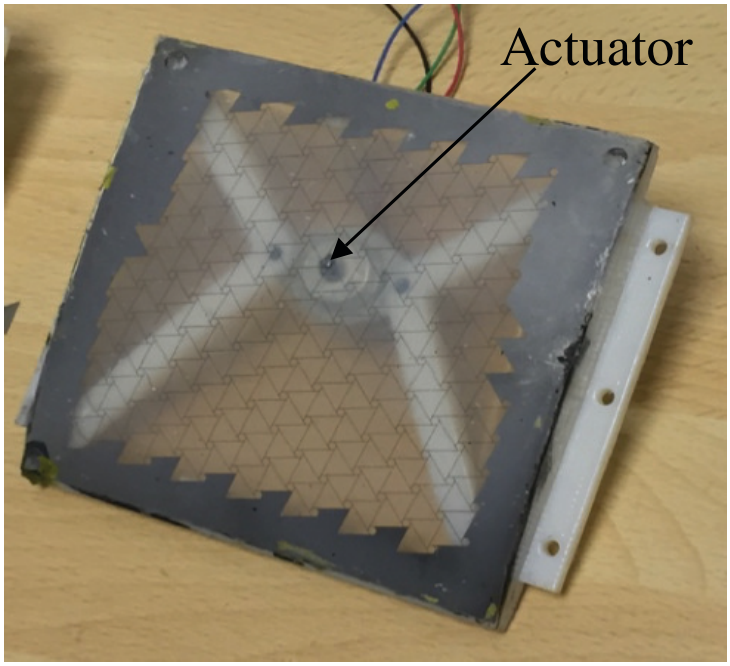
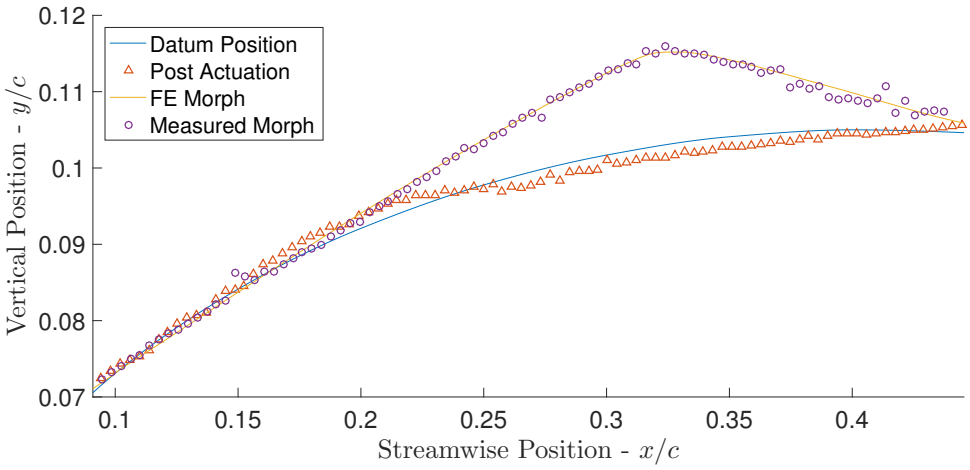


Figure 7.4: Convergence of the aerofoil boundary layer shape factor and peak stress with optimisation iterations



(a) Manufactured adaptive device based on a chiral lattice structure



(b) Measured deformed section

Figure 7.5: Wing section actuator

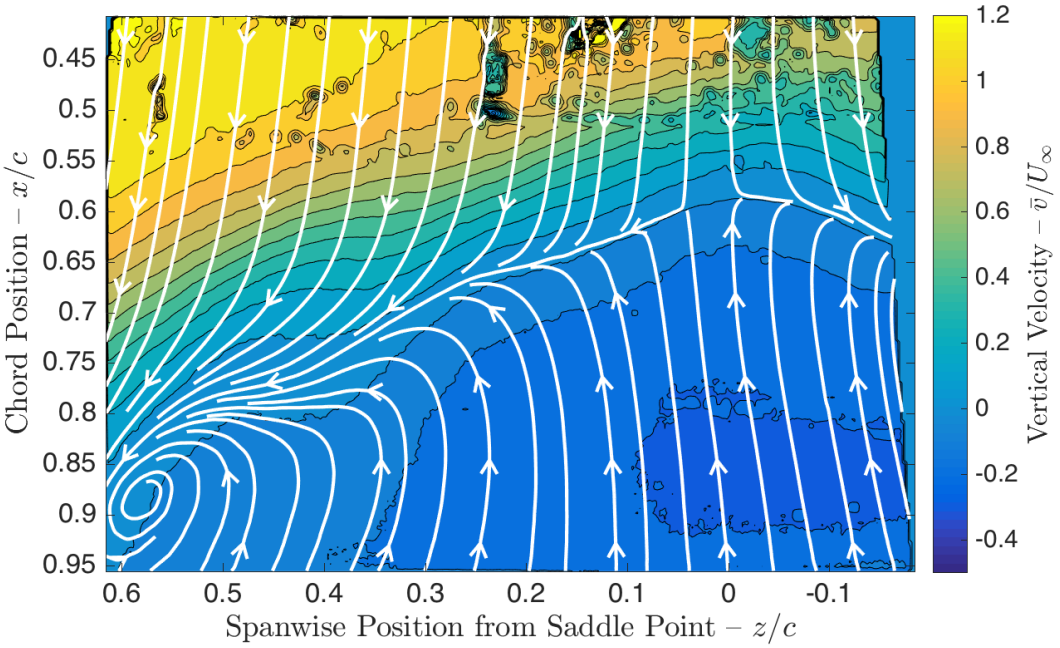
Fig. 7.5(b). The geometry can be seen to again compare well with the FE prediction in both the morphed and post-morph cases. As discussed in Sec. 5.4.4, the small pressure variation over the adaptive device has a minor effect on the final geometry due to the increased flexibility of the lattice surface. In the case of the flow over an aerofoil, there is an surface pressure variation due to the aerofoil geometry. To remove the influence of this offset on the final surface, a small hole is located on each spanwise side of the actuating section between the actuation cavity and the aerofoil surface. The pressure in the cavity under the lattice surface is therefore maintained at a similar pressure to that found on the un-actuated aerofoil. Only the small variation in pressure due to the actuated surface therefore acts to alter its geometry.

7.4 Actuation with an Adaptive Actuator

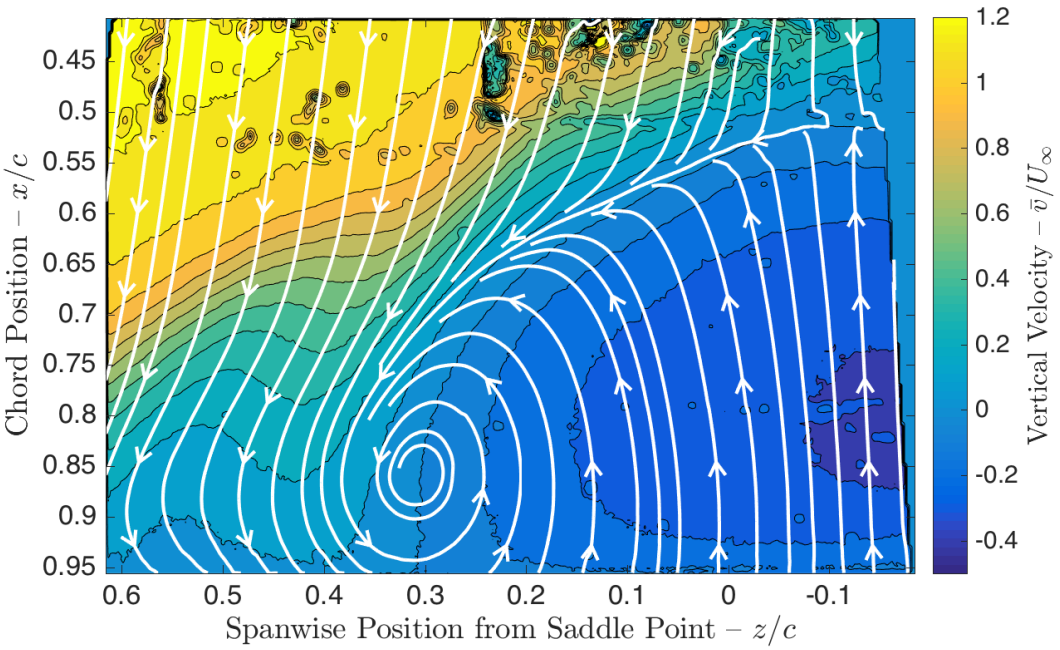
The discontinuous VG was removed and replaced with the adaptive device developed above and the experiment described in Sec. 7.2 was repeated. The flow over the actuator was recorded undeployed at $h = 0$ mm and deployed at the height determined through optimisation $h = 2.63$ mm. The flow fields for these results are shown in Fig. 7.6.

In the baseline case, the upstream extent, focus position and width of the stall cell compare well with previous measurements. When the device is actuated to the design height, as with the discontinuous VG, the focus of the stall cell can be seen to move towards the saddle point, decreasing the the size of the recirculating region. The effect is less pronounced than is seen using the fixed device. Unlike the previous case however, with the adaptive geometry deployed the saddle point is seen to move upstream. This behaviour is similar to that seen on the plate variant discussed previously and is attributed to the finite curvature constraint required by a morphing structure. In order to maintain an elastic deformation, the surface curvature must remain finite. Without the possibility of a sharp trailing edge, the vorticity generated is shed from the device periodically rather than continuously.

Interference can be seen in each vector field for values in the region $z < 0.25$ and $x < 0.52$. This is caused by incident reflections of the laser from the silicone towards the camera. These reflections cause the sensor to saturate in these regions and thus any reflections from seed particles in the flow are unrecoverable through background subtraction.



(a) Adaptive VG – 0 mm displacement



(b) Adaptive VG – 2.63 mm displacement

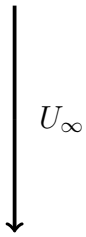


Figure 7.6: Flow field before and after actuation of the optimised Adaptive VG

Small oscillations were observed in the lattice surface during actuation. The oscillations were recorded by a series of photographs and, although it is not possible to obtain the displacement magnitude quantitatively, they did not appear large in comparison to the actuation.

7.5 Summary

The mean topology of the cellular separation pattern described in Chap. 6 is defined by a series of critical points. The layout of these points defines the distribution of surface streamlines on the model, and so the paths along which flow properties are convected.

At the saddle point, at the upstream extent of the cell, fluid from the upstream, attached flow, meets the recirculating fluid from the trailing edge. The streamline bifurcates to form the bounding streamline of the recirculating region.

A passive vortex generator is located upstream of the identified saddle point at $x/c = 0.3$ in order to increase the momentum along the bifurcating streamline. The resulting flow field shows a small increase in duration of attached flow immediately behind the saddle point. Additionally, a significant reduction in spanwise separation extent is observed, reducing the overall separated area.

This actuation is then replaced with an adaptive device generated using the aerodynamic optimisation process developed in Sec. 5.2. The integral CFD simulation within this method is updated to calculate the flow over the aerofoil profile used in Chap. 6 with $AR = 0.5$. The resulting parameters are used to manufacture an encapsulated lattice model as previously described. The actuated device surface compares well with that calculated in the FE simulation. The device returns to its original position once actuated demonstrating elastic deformation.

The final device is installed in a pocket within the experimental model and sealed in place with a wax sealant. A bleed hole equalised the cavity pressure with the surface pressure on the aerofoil surface. Baseline PIV data is taken before actuation to include any unintentional modification of the aerofoil surface by adding the adaptive structure (in the retracted position).

Following actuation the spanwise separation extent is seen to retract by $\approx 33\%$ or $z/c \approx 0.2$ as seen previously with the static VG. Contrary to the static case however, the upstream extent of the stall cell advances up the chord by $x/c \approx 0.05c$. The reduced efficacy is believed to be due to the reduced concentration of vortices from the adaptive actuation, with the continuous curvature constraint, than when compared to the static VG. However, it must be noted that, unlike the static VG, the adaptive device can be retracted when not required and so has no associated drag penalty.

Chapter 8

Conclusions

The overall aims of this research project are outlined in Sec. 2.3 and were two-fold:

- To develop a design methodology which will deliver an elastic, local, three-dimensional morphing geometry from an initially curved aerofoil to re-energise the fluid boundary-layer.
- To investigate the behaviour and topology of three-dimensional separation in order to identify characteristic traits to allow the detection and control of these features.

These two aims were examined in isolation in Chapters 5 and 6 and combined in Chapter 7. The principle conclusions of each strand are summarised below before suggestions are made on the continuation and evolution of this research.

8.1 The Design, Optimisation and Manufacture of an Adaptive Boundary-Layer Control Device

- The use of RMS positional error as an objective function for producing a morphing version of a geometry is only effective if the additional constraints of a morphing structure, notably for continuous shallow curvature, do not impinge on the efficacy of the structure. In work by previous authors this has been the case. In the example of a morphing VG however, the lack of high curvature at the trailing edge prevents the device from functioning efficiently.

- When a minimum radius of curvature is detrimental to the ideal geometry, using the final design metric allows the optimisation to achieve the best solution to the altered design space. In this case, the downstream shape factor H of the boundary layer describes the momentum distribution throughout the boundary layer and so can be used to judge the solution fitness.

- As discussed by previous authors, localised morphing structures are severely limited by the production of in-plane membrane strain for any deformation from a prismatic surface. This is due to the change of Gaussian curvature distribution in the surface which necessitates localised material elongation. As the yield strain of most traditional aerospace materials is $\approx 0.6\%$, this severely limits the total deformation possible.

- The use of a bending-dominated lattice structure in place of the adaptive surface allows a significant increase of in-plane surface yield strain and thus larger magnitude deflections. Due to the distributed nature of lattice structures, alterations to the constituent unit cell allows the alteration of structural properties by design.

- For out-of-plane local morphs, such as the ones discussed in this thesis, the use of a topology which exhibits bulk $\nu < 0$, termed Auxetic lattices, allows the production of doubly curved geometries with $\kappa > 0$ without the detrimental Poisson's effects associated with materials with $\nu > 0$. For this work, the Hex-Chiral lattice proposed by Prall and Lakes (1997) is used.

- These concepts have been combined into an aero-structural optimisation methodology for the reduction of a boundary-layer shape factor. The design variables contain all required parameters to produce and actuate a 2D lattice structure. In each step the initial lattice unit cell is reconstructed with the central node at the actuation location. The boundaries of the adaptive domain are determined from additional design variables and the lattice is then tessellated to cover the domain. The actuation determined by the optimisation algorithm is applied and the resulting deformed surface is calculated using a geometrically nonlinear finite element analysis.

- The deformed geometry is then embedded in a two stage RANS – LES simulation from which the time averaged boundary layer shape factor is determined. If the deformation is elastic, where $\sigma_{max} < \sigma_{yield}$, then the shape factor is returned as the objective value. If the yield criterion is breached, a dynamic penalty function

adds a weighted function to the shape factor to prevent unfeasible solutions being selected.

- The design parameters selected from a converged optimisation process have been used to manufacture the deformed geometry and this is tested in a sPIV-based wind tunnel experiment on a plate with zero pressure gradient. The geometry has been shown to be effective at transferring momentum towards the wall from the freestream flow. A separate model of the final lattice geometry is manufactured to high precision from Stainless Steel 1.4310. The structure is encapsulated in Silicone to provide an impermeable membrane and measured using a Faro laser scanner. The morphing geometry is found to both compare well with the FE predictions and return to its original position, demonstrating an elastic, repeatable morph.

8.2 Investigation of Cellular Separation from an Aerofoil

- The separation pattern above a NASA GA(W)-1 high lift aerofoil with $AR = 6$ at $Re = 3.5 \times 10^5$ and $\alpha = 15°$ has been investigated using surface oil flow visualisation, time-resolved stereo Particle Image Velocimetry sPIV, and surface pressure measurements.

- A spanwise periodic array of three-dimensional recirculating regions is observed on the surface of the model at a range of incidences. With increasing incidence, the size of these stall-cells increases and subsequently the number of cells decreases.

- Examination of the mean flow topology through multiple sPIV planes (Fig. 6.5) supports the flow-field model presented by Manolesos and Voutsinas (2015) in which the 2D separation line vortex and corresponding trailing edge vortex become unstable and form 3D variations in separation extent.

- Analysis of time-resolved surface pressure data taken from across the span of the stall cell identified two distinct frequencies of oscillation. The first is the anticipated von Kármán shedding typical of any separated wake and which occurs at non-dimensional frequency $St = f\ c\ \sin(\alpha)/U_\infty \approx 0.2$ and is detected towards the centre of the cell. The second oscillation, at $St \approx 0.02$, is detected near the recorded location of the focus.

- Proper Orthogonal Decomposition POD is conducted on the velocity fields from three of the sPIV planes recorded. The spatially coherent modes identified by the POD are split between: those containing small defined structures with vorticity of alternating sign and acting at the edge of the recirculating region; and those acting with constant sign over the entire cell.

- Analysis of the frequency content of the temporal variation in POD coefficients for these modes shows that the modes containing the smaller structures are found at $St \approx 0.2$ and thus correspond to the predicted von Kármán vortices.

- The larger, uniform variations, are instead seen to fluctuate with frequency $St \approx 0.02$. These variations represent the cell growing and contracting in spanwise length, altering the region of the model experiencing separated flow. These structures explain the low frequency component of fluctuating pressure visible towards the focus of the cell.

- These low-frequency oscillations in stall cell size are analogous to separation bubble pumping from sharp corners reported on a backward facing step by Berger et al. (1990) and Heenan and Morrison (1998), and an axi-symmetric body by Oxlade (2013) and Rigas et al. (2014).

- Previous authors Zaman et al. (1989) concerned with high lift configurations of aerofoils have reported low frequency oscillations in wing loading. This has however previously been associated with 2D 'flapping' of the separation region. For the first time, this has been associated experimentally with the spanwise pumping of the separated region.

8.3 Point Control of a Stall Cell

- The pattern of streamlines in three dimensional cellular separation in the mean flow field over a turbulent aerofoil contain a critical bifurcation point at their upstream extent. The streamline entering this bifurcation point splits and moves spanwise around the border of the cell. As streamlines describe the paths of convection of information through the flow field, any information imparted onto this streamline should be convected around the whole cell.

- Additional momentum was added to the near wall region along this streamline through the use of a forwards wedge static vortex generator with height approximately equal to the boundary layer thickness in Fig. 7.2. Through this point actuation, the spanwise extent of the separation region is shown to reduce by $z/c \approx 0.3$.
- An adaptive device is developed, from the initially-curved section found near the leading edge of the aerofoil profile, using the optimisation methodology described previously. The deformed geometry is shown in Fig. 7.5(b) and compares well with the FE predictions and remains elastic throughout.
- When this device is deployed in the wind tunnel, the spanwise extent of the separated region reduces by $\approx 33\%$ or $z/c \approx 0.2$. Unlike the static device however, the streamwise extent of the separation increases by $x/c \approx 0.05c$ under actuation. Despite this, a total reduction in recirculating area is observed in Fig. 7.6.
- Without the possibility of a sharp trailing edge, the vorticity generated is not shed cleanly from the adaptive device and so the resulting mixing is less focused and hence less efficient.
- However, as the device may be retracted when not required, this would have no impact on off-design performance.

8.4 Further Work

The field of adaptive structures is growing rapidly as the inclusion of aero-elastic effects within a design becomes more widespread. The development of a local 3D morph for boundary layer control has been central to this work. However, the limited surface area of the model which could be morphed required compromises in material thickness to be made for manufacturing purposes. In a larger scale model, the ratio between lattice spar width and material thickness could be significantly larger, allowing a greater range of bulk properties to be achieved. In addition, alternate materials may be used, in particular the methods of Virk et al. (2013) could be used to further increase the bulk yield strain.

In addition, while the device produced has been measured statically and tested experimentally, oscillations in the adaptive surface have been observed and commented on earlier in this work. Dynamic FE analysis and experimental measurements should be undertaken to establish the response of the system to unsteady perturbations.

More broadly, the use of a 2D Auxetic lattice surface in morphing applications allows a wide range of potential geometry alterations which have previously been unfeasible. In particular, transonic shock control bumps and local profile morphing for gust or roll control are theoretically possible.

Further understanding of the topology, and unsteadiness, of turbulent three-dimensional separation has been added to the literature, however significant questions still remain. In particular, the formation of a stable periodic pattern of cells is not fully understood. This was explained through downwash in the model of Weihs and Katz (1983), however in the model of Manolesos (2013), this downwash is secondary and thus unlikely to produce the required stability. Further investigation in the formation of the stable pattern through cyclic, phase locked, measurements of a plunging aerofoil, may provide further clarity.

In addition to the two periodic fluctuations identified and discussed above, Grandemange et al. (2013); Oxlade (2013); Rigas et al. (2014) identify an instability in the global wake position which switches or rotates between stable states with a much longer time period. This is similar to the switching between two arrangements of stall cells that occurs between stable conditions. In the second part of their work Grandemange et al. (2014) found that the addition of a central perturbation in the separating wake reduced the observed instability and so obtained a centred wake with improved performance. This is again analogous to the use of 'ZZ' tape by Manolesos (2013) as a central disturbance to fix the position of the stall cells in that work. The use of deployable perturbations, in conjunction with the self-stabilising behaviour of stall cells observed, may allow an arrangement of cells to be induced that is more beneficial to performance than the naturally occurring pattern.

The reduction of the separation of a single cell by actuation at a point upstream of the stall cell saddle point has been demonstrated using both a static VG and an adaptive device. The sensitivity of the position of this actuation has not, however, been explored and should be investigated in the future. Additionally, the effect of actuation of a cell on the wider pattern should be investigated. If the mechanism resulting in a stable stall cell pattern is indeed the induced downwash, then it follows that there will be an optimal level of actuation at which the maximum reduction in separation extent is achieved and yet the pattern remains stable.

References

Arrieta, A. F., Bilgen, O., Friswell, M. I. and Ermanni, P. (2013), 'Modelling and Configuration Control of Wing-Shaped Bi-Stable Piezoelectric Composites Under Aerodynamic Loads', *Aerospace Science and Technology* **29**(1), 453–461.

Barbarino, S., Bilgen, O., Ajaj, R. M., Friswell, M. I. and Inman, D. J. (2011), 'A Review of Morphing Aircraft', *Journal of Intelligent Material Systems and Structures* **22**(9), 823–877.

Berger, E., Scholz, D. and Schumm, M. (1990), 'Coherent Vortex Structures in the Wake of a Shere and a Circular Disk at Rest and under Forced Vibrations', *Journal of Fluids and Structures* **4**, 231–257.

Berkooz, G., Holmes, P. and Lumley, J. (1993), 'The Proper Orthogonal Decomposition in the Analysis of Turbulent Flows', *Annual Review of Fluid Mechanics* **25**(1971), 539–575.

Bernhammer, L. O., Teeuwen, S. P., Breuker, R. D., van der Veen, G. J. and Solingen, E. V. (2013), 'Gust Load Alleviation of an Unmanned Aerial Vehicle Wing Using Variable Camber', *Journal of Intelligent Material Systems and Structures* **25**(7), 795–805.

Blazek, J. (2005), Principles of Grid Generation, *in* 'Computational Fluid Dynamics: Principles and Applications', pp. 373–413.

Blondeau, J. and Pines, D. (2004), Pneumatic Morphing Aspect Ratio Wing, *in* 'Collection of Technical Papers - AIAA/ASME/ASCE/AHS/ASC Structures, Structural Dynamics and Materials Conference', Vol. 4, pp. 3218–3229.

Boiko, a. V., Dovgal, a. V., Zanin, B. Y. and Kozlov, V. V. (1996), 'Three-Dimensional Structure of Separated Flows on Wings (review)', *Thermophysics and Aeromechanics* **3**(1), 1–13.

Bowman, J., Sanders, B. and Cannon, B. (2007), Development of Next Generation Morphing Aircraft Structures, *in* '48th AIAA/ASME/ASCE/AHS/ASC Structures, Structural Dynamics, and Materials Conference'.

Broeren, A. and Bragg, M. (2001), 'Spanwise Variation in the Unsteady Stalling Flowfields of Two-Dimensional Airfoil Models', *AIAA Journal* **39**(9).

Bubert, E. A., Woods, B. K. S., Lee, K., Kothera, C. S. and Wereley, N. M. (2010), 'Design and Fabrication of a Passive 1D Morphing Aircraft Skin', *Journal of Intelligent Material Systems and Structures* **21**(17), 1699–1717.

Bye, D. R. and McClure, P. D. (2007), Design of a Morphing Vehicle, *in* '48th AIAA/ASME/ASCE/AHS/ASC Structures, Structural Dynamics, and Materials Conference', Vol. 44, pp. 1–16.

Cabitza, S. (2014), Active Control of the Wake from a Rectangular-Sectioned Body, PhD thesis, Imperial College.

Calladine, C. (1983), *Theory of Shell Structures*, Cambridge University Press.

Chen, J., Shen, X. and Li, J. (2015), 'Zero Poisson's Ratio Flexible Skin for Potential Two-Dimensional Wing Morphing', *Aerospace Science and Technology* **45**, 228–241.

Chen, P. C., Sarhaddi, D., Jha, R., Liu, D. D., Griffin, K. and Yurkovich, R. (2000), 'Variable Stiffness Spar Approach for Aircraft Maneuver Enhancement Using ASTROS', *Journal of Aircraft* **37**(5), 865–871.

Crow, S. C. (1970), 'Stability Theory for a Pair of Trailing Vortices', *AIAA Journal* **8**(12), 2172–2179.

Culick, F. and Jex, H. (1985), Aerodynamics, Stability and Control of the 1903 Wright Flyer, *in* 'Proceedings of the Symposium on the 80th Anniversary of the Wright Brothers First Flight', AIAA.

Dassault Systemes (2013), *Abaqus User Guide*, 6-13-2 edn, Dassault Systemes.

Dearing, S., Lambert, S. and Morrison, J. F. (2007), 'Flow Control with Active Dimples', *The Aeronautical Journal* **111**(1125), 705–714.

Délery, J. M. (2001), 'Robert Legendre and Henri Werlé: Toward the Elucidation of Three-Dimensional Separation', *Annual Review of Fluid Mechanics* **33**(1), 129–154.

Deshpande, V., Ashby, M. and Fleck, N. (2001), 'Foam Topology: Bending Versus Stretching Dominated Architectures', *Acta Materialia* **49**(6), 1035–1040.

Drela, M. (1989), XFOIL: An Analysis and Design System for Low Reynolds Number Airfoils, *in* T. J. Mueller, ed., 'Low Reynolds Number Aerodynamics: Proceedings of the Conference Notre Dame, Indiana, USA, 5–7 June 1989', Berlin, Heidelberg, pp. 1–12.

Duncan, G. T., Crawford, B., Tufts, M. W., Saric, W. S. and Reed, H. L. (2013), Effects of Step Excrescences on Swept-Wing Transition, *in* '31st AIAA Applied Aerodynamics Conference', American Institute of Aeronautics and Astronautics, Reston, Virginia.

Dussauge, J.-P., Dupont, P. and Debiève, J.-F. (2006), 'Unsteadiness in shock wave boundary layer interactions with separation', *Aerospace Science and Technology* **10**(2), 85–91.

Eaton, J. K. and Johnston, J. P. (1982), *Low Frequency Unsteadyness of a Reattaching Turbulent Shear Layer*, Springer Berlin Heidelberg, Berlin, Heidelberg, pp. 162–170.

Filippone, A. (2000), 'Data and performances of selected aircraft and rotorcraft', *Progress in Aerospace Sciences* **36**(8), 629–654.

Flynn, G. A., Morrison, J. F. and Mabey, D. G. (2001), 'Buffet Alleviation on Swept and Unswept Wings at High Incidence', *Journal of Aircraft* **38**(2), 368–378.

Garcia, H., Abdulrahim, M. and Lind, R. (2003), Roll Control for a Micro Air Vehicle Using Active Wing Morphing, *in* 'AIAA Guidance, Navigation, and Control Conference and Exhibit', pp. 1–12.

Gibson, L. J. and Ashby, M. F. (1999), *Cellular Solids: Structure and Properties*, 2 edn, Cambridge University Press.

Glezer, A. and Amitay, M. (2002), 'Synthetic Jets', *Annual Review of Fluid Mechanics* .

Gomez, J. C. and Garcia, E. (2011), 'Morphing Unmanned Aerial Vehicles', *Smart Materials and Structures* **20**(10), 103001.

Grandemange, M., Gohlke, M. and Cadot, O. (2013), 'Turbulent Wake Past a Three-Dimensional Blunt Body. Part 1. Global Modes and Bi-Stability', *Journal of Fluid Mechanics* **722**, 51–84.

Grandemange, M., Gohlke, M. and Cadot, O. (2014), 'Turbulent Wake Past a Three-Dimensional Blunt Body. Part 2. Experimental Sensitivity Analysis', *Journal of Fluid Mechanics* **752**, 439–461.

Gregory, N., Quincey, V., O'Reilly, C. L. and Hall, D. J. (1971), Progress Report on Observations of Three-Dimensional Flow Patterns Obtained During Stall Development on Aerofoils, and on the Problem of Measuring Two-Dimensional Charicteristics, report, Aeronautical Research Council.

Griffin, K. E. and Hopkins, M. a. (1997), 'Smart Stiffness for Improved Roll Control', *Journal of Aircraft* **34**(3), 445–447.

Gurka, R., Liberzon, A. and Hetsroni, G. (2006), 'POD of Vorticity Fields: A Method for Spatial Characterization of Coherent structures', *International Journal of Heat and Fluid Flow* **27**(3), 416–423.

Heenan, A. F. and Morrison, J. F. (1998), 'Passive Control of Pressure Fluctuations Generated by Separated Flow', *AIAA Journal* **36**(6).

Henry, J. J. (2005), Roll Control for UAVs by Use of a Variable-Span Morphing Wing, PhD thesis, University of Maryland.

Hollenstein, M. (2005), Mechanical Characterization of Soft Materials: Comparison Between Different Experiments on Synthetic Specimens, Report ETH/ZfM-2008/01, ETH Zurich.

Huang, R. F. and Lin, C. L. (1995), 'Vortex Shedding and Shear-Layer Instability of Wings at Low-Reynolds Numbers', *AIAA Journal* **33**, 1398–1403.

Jones, B. (1934), 'Stalling', *Journal of the Royal Aeronautical Society* **38**, 753–770.

Joo, J. J. (2006), Optimal Actuator Location Within a Morphing Wing Scissor Mechanism Configuration, *in* 'Proc. SPIE 6166, Smart Structures and Materials 2006: Modeling, Signal Processing, and Control'.

Joshi, S. P., Tidwell, Z., Crossley, W. A. and Ramakrishnan, S. (2004), Comparison of Morphing Wing Strategies Based Upon Aircraft Performance Impacts, *in* '45th AIAA/ASME/ASCE/AHS/ASC Structures Structural Dynamics Materials Conference', Vol. 2, pp. 1–7.

Kerker, R. (1973), 'Liftvanes'. US Patent 3,744,745.

Kolmogorov, A. (1941), 'The Local Structure of Turbulence in Incompressible Viscous Fluid for Very Large Reynolds Numbers', *Dokl. Akad. Nauk SSSR* **434**(1890), 9–13.

Kota, S., Hetrick, J. and Osborn, R. (2003), 'Design and Application of Compliant Mechanisms for Morphing Aircraft Structures', *Smart Structures and Materials 2003: Industrial and Commercial Applications of Smart Structures Technologies* **5054**(734), 24–33.

Kuethe, A. M. (1972), 'Effect of Streamwise Vortices on Wake Properties Associated with Sound Generation.', *Journal of Aircraft* **9**(10), 715–719.

LaVision GmbH (2015), *DaVis 8.3.0*.

Legendre, R. (1956), *Séparation de l'écoulement laminaire tridimensionnel*, Vol. 54.

Lighthill, M. J. (1963), Attachment and Separation in Three-Dimensional Flows, *in* L. Rosenhead, ed., 'Laminar Boundary Layers', Oxford University Press, pp. 72–82.

Ligrani, P. M., Harrison, J. L., Mahmmod, G. I. and Hill, M. L. (2001), 'Flow Structure Due to Dimple Depressions on a Channel Surface', *Physics of Fluids* **13**(11), 3442.

Lin, J. C. (2002), 'Review of Research on Low-Profile Vortex Generators to Control Boundary-Layer Separation', *Progress in Aerospace Sciences* **38**(4-5), 389–420.

Liu, T. and Woodiga, S. (2010), Experimental Examination of Skin Friction Topology in Separated Flows, *in* '48th AIAA Aerospace Sciences Meeting Including the New Horizons Forum and Aerospace Exposition', pp. 269–276.

Logdberg, O. (2006), Vortex Generators and Turbulent Boundary Layer Separation Control, PhD thesis, KTH Mechanics.

Love, A. E. H. (1888), 'The Small Free Vibrations and Deformation of a Thin Elastic Shell', *Philosophical Transactions of the Royal Society A: Mathematical, Physical and Engineering Sciences* **179**, 491–546.

Manolesos, M. (2013), Experimental and Computational Study of Three-Dimensional Separation and its Control Using Passive Vortex Generators, PhD thesis, National Technical University of Athens.

Manolesos, M. and Voutsinas, S. G. (2014), 'Study of a Stall Cell Using Stereo Particle Image Velocimetry', *Physics of Fluids* **26**(4), 045101.

Manolesos, M. and Voutsinas, S. G. (2015), 'Experimental Investigation of the Flow Past Passive Vortex Generators on an Airfoil Experiencing Three-Dimensional Separation', *Journal of Wind Engineering and Industrial Aerodynamics* **142**, 130–148.

Mathworks Inc. (2015), *MATLAB Version 8.6.0 (R2015b)*.

McCormick, B. W. (1995), *Aerodynamics, Aeronautics and Flight Mechanics (Vol 2)*, Wiley.

McCullough, G. B. and Gault, D. E. (1951), Examples of Three Representative Types of Airfoil-Section Stall at Low Speed, Report 2502, NACA.

McGhee, R. J. and Beaseley, W. D. (1973), Low-speed Aerodynamic Characteristics of a 17-percent-thick Medium Speed Airfoil Designed for General Aviation Applications, Report TN D-7428, NASA.

Miller, G. D. (1988), Active Flexible Wing (AFW) Technology, Report AFWAL-TR-87-3096, Flight Dynamics Laboratory.

Morton, B. R. (1984), 'The Generation and Decay of Vorticity', *Geophysical & Astrophysical Fluid Dynamics* **28**(3-4), 277–308.

Moss, G. and Murdin, P. (1971), Two-Dimensional Low-Speed Tunnel Tests on the NACA 0012 Section Including Measurements Made During Pitching Oscillations at the Stall, report, Aeronautical Research Council.

Mulleners, K., Hemireg, A. and Raffel, M. (2008), Investigations of Trailing Edge Stall on 2D Airfoils, *in* '14th Int. Symp. on Applic. of ...', pp. 7–10.

National Instruments (2013), *Labview Version 13.0.1*.

Nemec, M. and Zingg, D. (2002), 'Newton-Krylov Algorithm for Aerodynamic Design using the Navier-Stokes Equations', *AIAA Journal* **40**(6), 1146–1154.

North, P. (1976), 'The Suppression of Flow Separation by Sequential Wall Jets', *Journal of Fluids Engineering* **98**(3), 447–452.

Olympio, K. and Gandhi, F. (2007), Zero-ν Cellular Honeycomb Flexible Skins for One-Dimensional Wing Morphing, *in* '48th Structures, Structural Dynamics, and Materials Conference, AIAA/ASME/ASCE/AHS/ASC, Honolulu, Hi. April', number April, pp. 23–26.

OpenFOAM (2013), OpenCFD Ltd (ESI Group).

Oxlade, A. R. (2013), High-frequency Pulsed Jet Forcing of an Axisymmetric Bluff Body Wake, PhD thesis, Imperial College London.

Pope, S. (2009), *Turbulent Flows*, 6 edn, Cambridge University Press.

Poppleton, E. D. (1951), Boundary-layer Control for High Lift by Suction at the Leading-edge of a 40 deg Swept-back Wing, Report 2897, Aeronautics Research Council.

Prall, D. and Lakes, R. (1997), 'Properties of a Chiral Honeycomb with a Poisson's Ratio of -1', *International Journal of Mechanical Sciences* **39**(3), 305–314.

Prandtl, L. (1927), Motion of Fluids With Very Little Viscosity, Report 452, National Advisory Committee for Aeronautics.

Previtali, F., Arrieta, A. F. and Ermanni, P. (2015), 'Double-Walled Corrugated Structure for Bending-Stiff Anisotropic Morphing Skins', *Journal of Intelligent Material Systems and Structures* **26**(5), 599–613.

Rhodes, O. (2012), Optimal Design of Morphing Structures, PhD thesis, Imperial College London.

Rigas, G., Oxlade, A. R., Morgans, A. S. and Morrison, J. F. (2014), 'Low-Dimensional Dynamics of a Turbulent Axisymmetric Wake', *Journal of Fluid Mechanics* **755**.

Roshko, A. (1954), On the Drag and Shedding Frequency of Two-Dimensional Bluff Bodies, Report 3169, NACA.

Roupassov, D. V., Nikipelov, A. A., Nudnova, M. M. and Starikovskii, A. Y. (2009), 'Flow Separation Control by Plasma Actuator with Nanosecond Pulsed-Periodic Discharge', *AIAA Journal* **47**(1), 168–185.

Santer, M. and Pellegrino, S. (2009), 'Topological Optimization of Compliant Adaptive Wing Structure', *AIAA Journal* **47**(3), 523–534.

Schlichting, H. and Gersten, K. (2000), *Boundary Layer Theory*, 8th edn, Springer.

Seifert, A., Bachar, T. and Koss, D. (1993), 'Oscillatory Blowing: a Tool to Delay Boundary-Layer Separation', *AIAA Journal* **31**(11).

Sirovich, L. (1987), 'Turbulence and the Dynamics of Coherent Structures Part I: Coherent Structures', *Quarterly of Applied Mathematics* **45**(3), 561–571.

Smith, A. E., Coit, D. W. and Michalewicz, Z. (1997), Constraint-Handling Techniques - Penalty Functions, *in* T. Back, D. B. Fogel and Z. Michalewicz, eds, 'Handbook of Evolutionary Computation', IOP Publishing Ltd, chapter 5.2.

Spalart, P. and Allmaras, S. (1992), A One-Equation Turbulence Model for Aerodynamic Flows, *in* '30th Aerospace Sciences Meeting and Exhibit', American Institute of Aeronautics and Astronautics, Reston, Virigina.

Spalart, P. R. and Rumsey, C. L. (2007), 'Effective Inflow Conditions for Turbulence Models in Aerodynamic Calculations', *AIAA Journal* **45**(10), 2544–2553.

Taylor, H. D. and Hoadley, H. H. (1948), Design Criteria for and Applications of the Vortex Generator Mixing Principle, Report M-15038-1, United Aircraft Corp.

Thill, C., Etches, J. a., Bond, I. P., Potter, K. D. and Weaver, P. M. (2010), 'Composite Corrugated Structures for Morphing Wing Skin Applications', *Smart Materials and Structures* **19**(12).

Tobak, M. and Peake, D. (1982), 'Topology of Three-Dimensional Separated Flows', *Annual Review of Fluid Mechanics* **14**, 61–85.

Torenbeek, E. (1979), *Synthesis of subsonic airplane design*, Springer Netherlands, Dordrecht.

Tropea, C., Yarin, A. L. and Foss, J. F., eds (2007), *Handbook of Experimental Fluid Mechanics*, Springer.

Tucker, P. (2014), Unsteady Computational Fluid Dynamics in Aeronautics, *in* 'Fluid Mechanics and Its Applications', 1st edn, Vol. 104, Springer Netherlands, Dordrecht.

Udovidchik, N. and Morrison, J. F. (2006), Investigation of Active Dimple Actuators for Separation Control, *in* '3rd AIAA Flow Control Conference', pp. 1–9.

Uicker, J. J., Pennock, G. R. and Shigley, J. E. (2010), *Theory of Machines and Mechanisms*, Oxford University Press.

Vasiliev, V., Barynin, V. and Rasin, A. (2001), 'Anisogrid Lattice Structures Survey of Development and Application', *Composite Structures* **54**(2-3), 361–370.

Versmissen, J. (1974), Some Experiments on the Performance and the Drag Penalty of Various Distributed Roughness Bands used for Boundary Layer Transition Fixing, Report NLR TR 74009 U, National Aerospace Laboratory NLR.

Virk, K., Monti, A., Trehard, T., Marsh, M., Hazra, K., Boba, K., Remillat, C. D. L., Scarpa, F. and Farrow, I. R. (2013), 'SILICOMB PEEK Kirigami Cellular Structures: Mechanical Response and Energy Dissipation through Zero and Negative Stiffness', *Smart Materials and Structures* **22**(8), 084014.

Weihs, D. and Katz, J. (1983), 'Cellular Patterns in Poststall Flow Over Unswept Wings', *AIAA Journal* **21**(12), 1757–1759.

Weisbord, L. and Paros, J. M. (1965), 'How to Design Flexure Hinges', *Journal of Machine Design* **37**, 151–157.

Welch, P. D. (1967), The Use of Fast Fourier Transform for the Esitimation of Power Spectra: A Method Based on Time Averaging over Short, Modified Periodograms, *in* 'IEEE Trans. Audio and electroacoustic', Vol. 15, pp. 70–73.

Winkelmann, A. and Barlow, J. (1980), 'Flowfield Model for a Rectangular Planform Wing Beyond Stall', *AIAA Journal* **18**(8), 685–686.

Woods, B. K. S. and Friswell, M. I. (2012), Preliminary Investigation of a Fishbone Active Camber Concept, *in* 'Proceedings of the ASME 2012 Conference on Smart Materials, Adaptive Structures and Intelligent Systems', p. 555.

Yang, Z. and Hu, H. (2008), 'Laminar Flow Separation and Transition on a Low-Reynolds-Number Airfoil', *Journal of Aircraft* **45**(3), 1067–1070.

Yao, C., Lin, J. and Allan, B. (2002), Flow-field Measurement of Device-Induced Embedded Streamwise Vortex on a Flat Plate, *in* '1st Flow Control Conference', p. 16.

Yokozeki, T., Takeda, S. I., Ogasawara, T. and Ishikawa, T. (2006), 'Mechanical Properties of Corrugated Composites for Candidate Materials of Flexible Wing Structures', *Composites Part A: Applied Science and Manufacturing* **37**(10), 1578–1586.

Yon, S. and Katz, J. (1998), 'Study of the Unsteady Flow Features on a Stalled Wing', *AIAA Journal* **36**(3), 305–312.

Zaman, K. B. M. Q., McKinzie, D. J. and Rumsey, C. (1989), 'A Natural Low-Frequency Oscillation of the Flow over an Airfoil near Stalling Conditions', *Journal of Fluid Mechanics* **202**.